nature catalysis

Article

https://doi.org/10.1038/s41929-022-00865-5

Biomimetic active sites on monolayered metal–organic frameworks for artificial photosynthesis

In the format provided by the authors and unedited

Contents

Supplementary Methods

Synthesis of 4-(3-(3,5-bis(trifluoromethyl)phenyl)ureido)butanoic acid (Ur) The synthesis and characterization of Ur is shown in Supplementary Fig. 21. An aqueous solution of 4-amino butanoic acid (0.83 g, 8.0 mmol) was heated and 1-isocyanato-3,5-bis(trifluoromethyl)benzene (2.1 g, 8.2 mmol) was added in five portions to the gently refluxing solution. This reaction mixture was refluxed for 20 min, cooled to room temperature, and treated with an equimolar amount of concentrated HCl (12 M, 0.7 mL) to reach pH 1. This reaction mixture was then kept at room temperature for 7 h and the precipitated crystals filtered off. The solid was further purified by column chromatography on silica using a 10:1 $CHCl_3$:MeOH eluent to give Ur ligand as white crystals. Yield: 81% (2.32 g). ^{1}H NMR (500 MHz, DMSO-d_6) δ 9.22 (s, 1H), 8.08 (s, 2H), 7.54 (s, 1H), 6.56 (s, 1H), 3.12 (q, 2H), 2.24 (t, 2H), 1.67 (p, 2H). ^{13}C NMR (126 MHz, DMSO-d_6) δ 174.71, 155.3, 143.1, 131.01 (q, J = 32.76 Hz), 124.9, 122.7, 120.5, 39.1, 31.5, 25.5. HRMS: m/z calculated for $C_{13}H_{13}F_6N_2O_3$ $[M+H]^+$: 359.0910, found: 359.0838.

Synthesis of amide ligands Am-1 and Am-2 The synthesis and characterization of **Am-1** and **Am-2** is shown in Supplementary Fig. 23. 1 mmol 3,5-bis(trifluoromethyl)aniline (for **Am-1**) or N-methyl-3,5,bis(trifluoromethyl)-aniline (for **Am-2**), 148 uL monomethyl adipate (1 mmol), 211 mg 1-Ethyl-3-(3-dimethylaminopropyl)-carbodiimide hydrogenchloride (1.1 mmol), 122 mg DMAP (1 mmol) and 349 uL DIPEA (2 mmol) were added to 20 ml dry dichloromethane and stirred for 12 hours at room temperature. The solution was then washed three times with 1 M HCl and the solvent removed under reduced pressure. The resultant mixture was subjected to silica gel column and yielded the ester intermediate as a yellowish oil. 1 mL 0.5 M LiOH aqueous solution was added to 90 mg of this intermediate in 1 mL THF. After stirring for 2 hours, 1 mL 0.5 M HCl was added. The resultant mixture was extracted with ethyl acetate three times and the combined organic phase concentrated under vacuum to give the crude product. Recrystallization by adding diethyl ether into the ethyl acetate solution of the crude product gave the targeted product 6-((3,5-

bis(trifluoromethyl)phenyl)amino)-6-oxohexanoic acid (**Am-1**) as a white solid (140 mg, 39%) or 6-((3,5-bis(trifluoromethyl)phenyl)(methyl)amino)-6-oxohexanoic acid (**Am-2**) as a white solid (130 mg, 35%). **Am-1**: ^{1}H NMR (400 MHz, DMSO) δ 10.56 (s, 1H), 8.26 (s, 2H), 7.73 (s, 1H), 2.37 (t, *J* = 7.2 Hz, 2H), 2.24 (t, *J* = 7.1 Hz, 2H), 1.66 – 1.50 (m, 4H). ^{13}C NMR (101 MHz, DMSO) δ 174.80, 172.69, 141.53, 131.68, 131.20 (q, *J* = 33 Hz), 125.06, 122.35, 119.09, 36.61, 33.86, 24.75, 24.49. HRMS (ESI-TOF): calculated for $C_{14}H_{13}F_6NO_3$ $[M+H]^+$: 358.0878, found 358.0859. **Am-2**: ^{1}H NMR (400 MHz, $CDCl_3$) δ 7.84 (s, 1H), 7.68 (s, 2H), 3.34 (s, 3H), 2.46 – 2.18 (m, 4H), 1.73 – 1.61 (m, 4H). ^{13}C NMR (101 MHz, $CDCl_3$) δ 178.29, 172.26, 153.46, 145.43, 127.41, 124.07, 121.36, 37.59, 33.97, 33.44, 24.47, 24.14. HRMS (ESI-TOF): calculated for $C_{14}H_{13}F_6NO_3$ $[M+H]^+$: 372.1034, found 372.1091.

Synthesis of [Ir(Me-MBA)Cp*Cl]Cl (Me-MBA-Ir) $[IrCp^*Cl]_2Cl_2$ and methyl 2-(4'-methyl-[2,2'-bipyridin]-4-yl)acetate (Me-MBA) were synthesized as previously described.[60] $[IrCp^*Cl]_2Cl_2$ (796.7 mg, 1.0 mmol), Me-MBA (0.85 g, 2.0 mmol), methanol (25 mL), and chloroform (25 mL) were added to a 200 mL thick-walled sealed tube. The vessel was then degassed with N_2, sealed, and heated to 120 °C for 2 days while stirring. After cooling to ambient temperature, the solvent was removed under reduced pressure to afford pure Me-MBA-Ir as an orange solid (1.64 g, 2.0 mmol, 100%). ^{1}H NMR (500 MHz, DMSO-d_6) δ 8.92 (d, 1H), 8.81 (d, 1H), 8.71 (s, 1H), 8.60 (s, 1H), 7.79 (d, 1H), 7.70 (d, 1H), 4.10 (s, 2H), 3.71 (s, 3H), 2.63 (s, 3H), 1.66 (s, 15H).

Synthesis of [Ir(H-MBA)Cp*Cl]Cl (H-MBA-Ir) To Me-MBA-Ir (57 mg, 0.1 mmol, in 15 mL H_2O) was added concentrated HCl (5 mL) slowly. The solution was stirred at reflux for 24 h. The solvent was then removed under vacuum to yield the product [Ir(H-MBA)Cp*Cl]Cl (H-MBA = 2-(4'-methyl-[2,2'-bipyridin]-4-yl)acetic acid) as a yellow powder (50 mg , 90%). ^{1}H NMR (400 MHz, DMSO-d_6) δ 8.90 (d, 1H), 8.81 (d, 1H), 8.70 (s, 1H), 8.62 (s, 1H), 7.79 (d, 1H), 7.70 (d, 1H), 3.99 (s, 2H), 2.63 (s, 3H), 1.65 (s, 15H).

Synthesis of 6-oxo-6-(phenylamino) hexanoic acid derived Am-R ligands The synthesis and characterization of **Am-R** (R = OCH_3, CH_3, F, H, Cl, Br, or NO_2) ligands is shown in Supplementary Fig. 29. To monomethyl

adipate (0.163 mL, 1.10 mmol) was added thionyl chloride (0.99 mL, 1.23 mmol) and heated at 80 °C for 30 minutes, cooled to room temperature, dried under vacuum, and used without further purification. To a solution of different anilines (1 mmol), including *p*-anisidine for **Am-OCH$_3$**, *p*-toluidine for **Am-CH$_3$**, *p*-fluoroaniline for **Am-F**, aniline for **Am-H**, *p*-chloroaniline for **Am-Cl**, *p*-bromoaniline for **Am-Br**, *p*-nitroaniline for **Am-NO$_2$**, and triethylamine (0.209 mL, 1.5 mmol) in 5 mL of dry dichloromethane, was added dropwise the acid chloride (1.1 mmol) at 0 °C. The solution was allowed to warm to room temperature and stirred for 1 day. The solution was concentrated under vacuum and used without further purification. To a solution of this ester in 1 mL MeOH and 3 mL THF was added dropwise 2 mL of 1 M LiOH and stirred at room temperature, overnight. 5 mL water was added and THF and MeOH were removed under reduced pressure. The solution was then acidified with 1 M HCl until pH = 1, and extracted with 10 mL of ethyl acetate. The organic layer was then washed with 5 mL of 1 M HCl twice and 5 mL of brine, before being collected, dried over Na_2SO_4, and concentrated under reduced pressure to yield the desired **Am-R** products:

6-((4-methoxyphenyl)amino)-6-oxohexanoic acid (**Am-OCH$_3$**). White solid. Yield: 57% (0.143 g). ^{1}H NMR (400 MHz, DMSO) δ 9.72 (s, 1H), 7.48 (d, *J* = 8.9 Hz, 2H), 6.86 (d, *J* = 9.0 Hz, 2H), 3.71 (s, 3H), 2.25 (dt, *J* = 11.1, 6.8 Hz, 4H), 1.61 – 1.50 (m, 4H). ^{13}C NMR (101 MHz, DMSO) δ 174.86, 170.99, 155.48, 132.94, 121.06, 114.24, 55.61, 36.43, 33.89, 25.20, 24.62. HRMS (ESI-TOF): calculated for $C_{13}H_{18}NO_4$ $[M+H]^+$: 252.1236, found 252.1224.

6-oxo-6-(p-tolylamino)hexanoic acid (**Am-CH$_3$**). White solid. Yield: 53% (0.124 g). ^{1}H NMR (400 MHz, DMSO) δ 9.77 (s, 1H), 7.46 (d, *J* = 8.2 Hz, 2H), 7.08 (d, *J* = 8.1 Hz, 2H), 2.32 – 2.20 (m, 7H), 1.61 – 1.50 (m, 4H). ^{13}C NMR (101 MHz, DMSO) δ 174.92, 171.37, 137.17, 132.39, 129.50, 119.58, 36.50, 33.90, 25.15, 24.60, 20.87. HRMS (ESI-TOF): calculated for $C_{13}H_{18}NO_3$ $[M+H]^+$: 236.1287, found 236.1273.

6-((4-fluorophenyl)amino)-6-oxohexanoic acid (**Am-F**). White solid. Yield: 93% (0.222 g). ^{1}H NMR (400 MHz, DMSO) δ 12.02 (s, 1H), 9.93 (s, 1H), 7.65 – 7.55 (m, 2H), 7.18 – 7.07 (m, 2H), 2.27 (dt, *J* = 22.5, 7.3 Hz, 4H),

1.66 – 1.47 (m, 4H). ^{13}C NMR (101 MHz, DMSO) δ 174.82, 171.37, 159.46, 136.19, 121.23, 121.15, 115.77, 115.54, 36.48, 33.88, 25.10, 24.60. ^{19}F NMR (377 MHz, DMSO) δ -119.80. HRMS (ESI-TOF): calculated for $C_{12}H_{15}FNO_3$ $[M+H]^+$: 240.1036, found 240.1035.

6-oxo-6-(phenylamino)hexanoic acid (**Am-H**). White solid. Yield: 62% (0.138 g). ^{1}H NMR (400 MHz, DMSO) δ 9.87 (s, 1H), 7.61 – 7.54 (m, 2H), 7.33 – 7.24 (m, 2H), 7.07 – 6.98 (m, 1H), 2.35 – 2.20 (m, 4H), 1.66 – 1.47 (m, 4H). ^{13}C NMR (101 MHz, DMSO) δ 174.87, 171.54, 139.74, 129.13, 123.45, 119.51, 36.56, 33.89, 25.12, 24.60. HRMS (ESI-TOF): calculated for $C_{12}H_{16}NO_3$ $[M+H]^+$: 222.1130, found 222.1120.

6-((4-chlorophenyl)amino)-6-oxohexanoic acid (**Am-Cl**). White solid. Yield: 52% (0.133 g) ^{1}H NMR (400 MHz, DMSO) δ 10.02 (s, 1H), 7.61 (d, *J* = 8.7 Hz, 2H), 7.34 (d, *J* = 8.8 Hz, 2H), 2.27 (dt, *J* = 28.6, 6.9 Hz, 4H), 1.64 – 1.50 (m, 4H). ^{13}C NMR (101 MHz, DMSO) δ 174.84, 171.71, 138.69, 129.03, 121.03, 55.36, 36.54, 33.87, 25.03, 24.58. HRMS (ESI-TOF): calculated for $C_{12}H_{15}ClNO_3$ $[M+H]^+$: 256.0741, found 256.0719.

6-((4-bromophenyl)amino)-6-oxohexanoic acid (**Am-Br**). White solid. Yield: 47% (0.140 g) ^{1}H NMR (400 MHz, DMSO) δ 12.02 (s, 1H), 10.01 (s, 1H), 7.61 – 7.53 (m, 2H), 7.51 – 7.43 (m, 2H), 2.28 (dt, *J* = 29.1, 6.5 Hz, 4H), 1.66 – 1.47 (m, 4H). ^{13}C NMR (101 MHz, DMSO) δ 174.81, 171.69, 139.13, 131.94, 121.40, 114.92, 101.87, 36.58, 33.88, 25.02, 24.59. HRMS (ESI-TOF): calculated for $C_{12}H_{14}BrNNaO_3$ $[M+Na]^+$: 322.0055 and 324.0034, found 322.0068 and 324.0046.

6-((4-nitrophenyl)amino)-6-oxohexanoic acid (**Am-NO$_2$**). Light yellow solid. Yield: 77% (0.205 g). ^{1}H NMR (400 MHz, DMSO) δ 10.52 (s, 1H), 8.26 – 8.18 (m, 2H), 7.88 – 7.80 (m, 2H), 2.39 (t, *J* = 7.2 Hz, 2H), 2.25 (t, *J* = 7.2 Hz, 2H), 1.68 – 1.46 (m, 4H). ^{13}C NMR (101 MHz, DMSO) δ 174.83, 172.60, 145.89, 142.47, 125.46, 119.11, 36.70, 33.85, 24.82, 24.52, 24.48. HRMS (ESI-TOF): calculated for $C_{12}H_{15}N_2O_5$ $[M+H]^+$: 267.0981, found 267.0978.

Supplementary Notes

Supplementary Note 1. Hf-Ir MOF monolayer

Hf-Ir was synthesized through the following protocol: To a 4 mL glass vial was added 0.5 mL of a $HfCl_4$ solution [2.0 mg/mL in N,N-Dimethylformamide (DMF)], 0.5 mL of an Ir-PS solution (4.0 mg/mL in DMF), 2 μL of trifluoroacetic acid (TFA), and 5 μL of water. The reaction solution was kept in an 80 °C oven for 24 hours. The afforded yellow precipitate was collected by centrifugation and washed with DMF three times. Yield was 43% based on Hf as determined by ICP-MS.

As shown in Supplementary Fig. 1a, the Hf-Ir monolayer is proposed to be constructed from previously reported Hf_{12} clusters [61], which are vertically capped by TFA and laterally linked by Ir-PS to generate a 2D network with a **kgd** topology. This monolayer morphology of Hf-Ir was confirmed by TEM and AFM, revealing a diameter of ~150 nm (Supplementary Fig. 1b) and a thickness of ~1.7 nm, respectively, corresponding with the modeled structure of TFA capped Hf_{12} cluster (Supplementary Fig. 1d, e). The **kgd** topology was confirmed by both HRTEM (Supplementary Fig. 1c) and HAADF (Supplementary Fig. 1h-j) revealing a six-fold pattern and a Hf_{12}-Hf_{12} distance of ~2.8 nm, corresponding with the modeled structure of Hf-Ir. Additionally, Hf-Ir presented a similar PXRD pattern to that of its simulated structure (Supplementary Fig. 1f). The composition of Hf-Ir is thus proposed to be $Hf_{12}(\mu_3\text{-}O)_8(\mu_3\text{-}OH)_8(\mu_2\text{-}OH)_6(\text{Ir-PS})_6(\text{TFA})_6$. This composition is confirmed by ICP-MS, which revealed the expected Hf:Ir ratio of approximately 2:1, as well as by NMR of digested Hf-Ir where ^1H NMR confirmed the presence of Ir-PS (Supplementary Fig. 1k) and ^{19}F NMR revealed the expected 1:1 ratio of TFA to Ir-PS (Supplementary Fig. 1l). (*N.B.*, Ir-PS has two -CF_3 groups while each TFA only has one -CF_3 group so a 2:1 NMR signal ratio of Ir-PS to TFA in Supplementary Fig. 1l corresponds to a 1:1 molar ration of Ir-PS to TFA).

Supplementary Note 2. Active sites in MOZs

Each Hf_{12} cluster in the Hf-Ir monolayer is capped by six TFA molecules, with three on both the top and bottom faces. (Each face of Hf_{12} clusters is defined as potentially active site after hemin and AA loading). The strongly electron withdrawing -CF_3 groups in TFA results in weak coordination to the Hf_{12} clusters (through Hf-O bonds). This weak coordination is reflected in the strong acidity of TFA (pKa = 0.23) and enables facile carboxylate exchange reactions with more electron-rich carboxylate group. This property makes the Hf-Ir monolayer a versatile template for building catalytic sites.

To construct **MOZ-1**, the electron-rich carboxylate groups of hemin, with a pKa of 3.2-3.5[62], could efficiently replace the CF_3COO^- in Hf-Ir monolayer. 8.0% of TFA in Hf-Ir was replaced by hemin from a 0.10 molar equivalent hemin solution in DMF over a 3-h reaction, as determined by UV-vis analysis (Fig. 3e). We propose this 8.0% hemin-loading is distributed homogenously over Hf_{12} sites.

To construct more complex MOZs, AAs or Ur (3 equivalents to TFA) with relatively electron-rich carboxylate groups and pKa of ~2.0 successfully replaced the remaining TFA in **MOZ-1**, while not replacing hemin (*vide infra*). To note, Glu is likely binding through the carboxylate group in the side chain rather than the main chain; however, would result in the same observed effect.

The binding of catalysts (e.g., Hemin) and ligands (e.g., Ur) to the Hf SBUs through carboxylate groups is further supported by the FTIR results. The bounded TFA in Hf-Ir was removed through a modified procedure as previously reported[63] and the as-generated TFA-free Hf-Ir showed two new signals at 3677 cm^{-1} and 2744 cm^{-1} (Supplementary Fig. 3i). After removal of TFA groups, the Hf SBUs in TFA-free Hf-Ir are terminated by OH/H_2O pairs.[64] The signals at 3677 cm^{-1} and 2744 cm^{-1} are assigned the stretches of terminal Hf-OH and H-bonded Hf-H_2O, respectively. These assignments are consistent with previous results (3674 cm^{-1} for the terminal -OH and 2745-2747 cm^{-1} for the H-bonded terminal H_2O on Zr SBUs).[64] Upon treatment of TFA-free Hf-Ir with excess Hemin or Ur, these two signals disappeared in the resulting Hf-Ir-Hemin or Hf-Ir-Ur, demonstrating that

both Hemin (a representative catalyst) and Ur (a representative ligand) bind to Hf SBUs through the carboxylate groups.

Here we used the **MOZ-4** as an example to analyze the potential combinations of hemin and AAs/Ur in MOZs (Supplementary Fig. 6). There are three coordination sites on each side of Hf_{12} SBU and all these three sites are identical. The two-step modification process of **MOZ-4** by hemin and Ur can lead to four potential combinations of Hemin and Ur on each side of Hf_{12} SBU, including three hemin (combination A), two hemin and one Ur (combination B), one hemin and two Ur (combination C), and three Ur (combination D). Because of replacement of TFA by hemin in the first step occurs randomly, the probability of each combination is calculated as:

$$P_{Combination\ A} = C_3^3 \times 0.08 \times 0.08 \times 0.08 = 0.05\% \quad (1)$$

$$P_{Combination\ B} = C_3^2 \times 0.08 \times 0.08 \times 0.92 = 1.78\% \quad (2)$$

$$P_{Combination\ C} = C_3^1 \times 0.08 \times 0.08 \times 0.08 = 20.31\% \quad (3)$$

$$P_{Combination\ D} = C_3^0 \times 0.08 \times 0.08 \times 0.08 = 77.87\% \quad (4)$$

In all of three combinations (A, B, and C) with hemin, combination C (one hemin and two Ur) is dominant at 91.7% [20.31/(0.05+1.78+20.31) = 91.7%] and serves as the major active site in **MOZ-4**.

All other MOZs were prepared in the same process as **MOZ-4**. They have the same arrangement of the catalyst (hemin or MBA-Ir) and AAs (or Ur or Am-Cl) as **MOZ-4**. Therefore, the combination of one catalyst and two AAs (or artificial ligands) is also the dominant species in these MOZs. In these MOZs, the catalyst (hemin or MBA-Ir) and two AAs (Ur or Am-Cl) are several Ångstroms apart.

Supplementary Note 3. Composition analysis of CO_2-reduction MOZs

MOZ-1. The hemin to Ir-PS ratio in **MOZ-1** was determined to be 8.0% by UV-Vis analysis (Supplementary Fig. 3e), suggesting 8.0% of capped TFA is replaced by hemin through carboxylate exchange. The composition of **MOZ-1** is thus proposed to be $Hf_{12}(\mu_3\text{-}O)_8(\mu_3\text{-}OH)_8(\mu_2\text{-}OH)_6(\text{Ir-PS})_6(\text{Hemin})_{0.48}(\text{TFA})_{5.52}$.

MOZ-2, **MOZ-3**, and **MOZ-4**. **MOZ-2**, **MOZ-3**, and **MOZ-4** were synthesized from **MOZ-1**, with capping-TFA being fully replaced by Glu, Asn, and Ur, respectively. This replacement was confirmed by the NMR analysis of digested MOZs (Supplementary Fig. 5). The paramagnetic nature of hemin prevents direct NMR measurement so hemin-free **MOZ-2***, **MOZ-3***, and **MOZ-4*** were synthesized directly from Hf-Ir. All digested hemin-free MOZs showed Ir-PS signal in ^{1}H NMR, and **MOZ-2***, **MOZ-3***, and **MOZ-4*** each presented the expected signals of Glu, Asn, and Ur, respectively. The ratios of Ir-PS to Glu, Asn or Ur were close to 1:1, confirming complete replacement of TFA. The hemin to Ir-PS ratios for **MOZ-2**, **MOZ-3**, and **MOZ-4** were determined to be 7.8%, 8.0%, and 7.7%, respectively, by UV-vis analysis. Therefore, the compositions of **MOZ-2**, **MOZ-3**, and **MOZ-4** are proposed to be $Hf_{12}(\mu_3\text{-}O)_8(\mu_3\text{-}OH)_8(\mu_2\text{-}OH)_6(\text{Ir-PS})_6(\text{Hemin})_{0.47}(\text{Glu})_{5.53}$, $Hf_{12}(\mu_3\text{-}O)_8(\mu_3\text{-}OH)_8(\mu_2\text{-}OH)_6(\text{Ir-PS})_6(\text{Hemin})_{0.48}(\text{Asn})_{5.52}$, and $Hf_{12}(\mu_3\text{-}O)_8(\mu_3\text{-}OH)_8(\mu_2\text{-}OH)_6(\text{Ir-PS})_6(\text{Hemin})_{0.46}(\text{Ur})_{5.54}$, respectively.

Supplementary Note 4. Active-site density in MOZs

As shown in Supplementary Fig. 1a, MOZs are composed of repeating triangular units of Hf_{12} clusters. Considering the Hf_{12}-Hf_{12} distance of ~2.8 nm and Hf_{12} height of ~2.1 nm in MOZs, the volume of this unit, assumed to be a triangular prism, was estimated:

$$0.5 \times 2.8 \times 1.4\sqrt{3} \times 2.1 = 7.1\ \text{nm}^3 \quad (5)$$

Since each unit has three Hf_{12} clusters and each Hf_{12} cluster is shared by another adjacent 5 units, each Hf_{12} cluster has two Hf_{12} site, 20.3% of which are active (i.e., connect to hemin), allowing for the average volume for each active site to also be estimated:

$$\frac{7.1}{3 \div 6 \times 2 \times 20.3\%} = 35\ \mathrm{nm}^3 \tag{6}$$

For enzymes, the volume (V) for each active-site/enzyme can be estimated from its mass (M) through the empirical equation [65]:

$$V(nm^3) = 1.212 \times 10^{-3} \left(\frac{\mathrm{nm}^3}{\mathrm{Da}}\right) \times M(\mathrm{Da}) \tag{7}$$

Since the majority of enzyme protein molecules have a molecular weight within the range of 20-160,000 kDa (average of ~50 kDa), the average volume for each active site in enzymes is estimated to be:

$$1.212 \times 10^{-3} \left(\frac{\mathrm{nm}^3}{\mathrm{Da}}\right) \times 50{,}000(\mathrm{Da}) = 60\ \mathrm{nm}^3 \tag{8}$$

According to these estimation results, the MOZs (~35 nm^3 per active-site) in this work have a higher active-site density than most enzymes (~60 nm^3 per active-site).

Supplementary Note 5. CO_2RR product detection

The calibration curves of CO, CH_4, and H_2 were generated for GC qualification and quantification (Supplementary Fig. 9). For MOZ-catalyzed CO_2RR, the generated CH_4 and CO were detected by FID, while the generated H_2 was detected by TCD. The remaining CO_2 was detected by both FID and TCD. The retention times of CH_4, CO, and CO_2 were determined to be 1.96, 1.08, and 4.40 min, respectively, using pure gases as standards by FID detection (Supplementary Fig. 9a). The retention times of H_2 and CO_2 were determined to be 0.65 and 4.40 min, respectively, using pure gases as standards by TCD detection (Supplementary Fig. 9b). The calibration curves of CH_4 and CO by FID detection and H_2 by TCD detection were separately generated (Supplementary Fig. 9c-e). The full GC traces of MOZ-catalyzed CO_2RR (48-hour reaction, in triplicate for each

MOZ) were provided as an example (Supplementary Fig. 9a, b). Because the volume of generated CH_4, CO, or H_2 was <0.1% of that of remaining CO_2, the scale of signal intensities in each GC trace was adjusted to highlight CH_4, CO, and H_2. In addition, the generation of liquid products (e.g., methanol and HCOOH) was ruled out by GC-MS and HPLC, respectively.

The gas products of MOZ-catalyzed CO_2RR were confirmed by GC-MS (Supplementary Fig. 10). The full GC-MS traces of MOZ-catalyzed CO_2RR (represented by **MOZ-4** in triplicate, 48-hour reaction) are provided as an example (Supplementary Fig. 10a). The generated CH_4 and CO were detected at retention times of 3.64 and 6.71 min, respectively (Supplementary Fig. 10a). The calibration curves of CH_4 and CO were separately generated (Supplementary Fig. 10c, d). Because GC-MS has a lower CH_4 detection sensitivity than GC, the catalyst loading of **MOZ-4** was increased by 4 times to ensure accurate quantification of the generated CH_4 by GC-MS. After 48-hour reaction, the TONs of CH_4 and CO for **MOZ-4** catalyzed CO_2RR were determined to be 6233 ± 282 and 18366 ± 2026, respectively, by the GC-MS, which are close to those (7415 ± 737 for CH_4 and 19049 ± 1756 for CO) determined by GC. The slight difference between the TON numbers determined by GC-MS and GC may be caused by the increased **MOZ-4** loading and/or catalytic activity difference in different batches of **MOZ-4**.

Furthermore, MOZ-catalyzed CO_2RR was performed with $^{13}CO_2$ (as carbon source) and CF_3CD_2OD (as proton source). The corresponding isotope-labeled products were detected by GC-MS (Supplementary Fig. 11). Under normal $^{12}CO_2$ and CF_3CH_2OH, $^{12}CH_4$ (m/z of 16) and ^{12}CO (m/z of 28) were detected in **MOZ-4** catalyzed CO_2RR at retention times of 3.64 and 6.71 min, respectively (Supplementary Fig. 11a). Under $^{13}CO_2$ and CF_3CH_2OH, $^{13}CH_4$ (m/z of 17) and ^{13}CO (m/z of 29) were detected at the same retention times (Supplementary Fig. 11c). Under $^{12}CO_2$ and CF_3CD_2OD, $^{12}CD_4$ (m/z of 20) and ^{12}CO (m/z of 28) were detected at the same retention times (Supplementary Fig. 11e). These results show that CH_4 and CO in MOZ-catalyzed CO_2RR are generated from CO_2 as carbon source and CF_3CH_2OH as proton source.

Supplementary Note 6. Electron transfer in MOZ-catalyzed CO_2RR and WOR

The electron transfer processes between photo-excited Ir-PS and various functional components in MOZs were studied by luminescence quenching, time-resolved luminescence spectroscopy, and CV.

Luminescence quenching: Hemin was added incrementally to a 20 μM Ir-PS solution in DMF to afford hemin concentrations of 0, 3.3, 6.7, 10.0, 13.3, 16.7, and 20.0 μM. A luminescence spectrum was collected at each hemin concentration by a fluorimeter with an excitation wavelength of 350 nm (Supplementary Fig. 13a). The oxidative quenching of Ir-PS by hemin was supported by fitting the observed intensities at 545 nm (I) to the concentration of hemin (C_{Hemin}) using the Stern-Völmer equation:

$$\frac{I_0}{I} = 1 + K_{\mathrm{SV}} C_{\mathrm{Hemin}} \tag{9}$$

where K_{SV} is the Stern-Völmer constant and I_0/I is the ratio of luminescence intensity of Ir-PS at 545 nm in the absence and presence of hemin. I_0/I revealed a strong linear correlation to C_{Hemin} with $R^2 = 0.99$ and $K_{\mathrm{SV}} = 0.155$ μM^{-1}.

The luminescence quenching of Ir-PS by BIH was studied under a similar condition (Supplementary Fig. 13b) with $R^2 = 0.99$ and $K_{\mathrm{SV}} = 0.057$ μM^{-1}.

The luminescence quenching of Ir-PS by Me-MBA-Ir was studied under a similar condition (Supplementary Fig. 28a) with $R^2 = 0.99$ and $K_{\mathrm{SV}} = 0.048$ μM^{-1}.

The luminescence quenching of Ir-PS by $K_2S_2O_8$ was studied under a similar condition (Supplementary Fig. 28b) with $R^2 = 0.99$ and $K_{\mathrm{SV}} = 0.281$ μM^{-1}.

These Fluorescence quenching studies showed that the photo-excited Ir-PS can be effectively quenched by both Hemin and BIH in MOZ-catalyzed CO_2RR and by both MBA-Ir and $Na_2S_2O_8$ in MOZ-catalyzed WOR.

Time-resolved luminescence spectroscopy: The time-resolved luminescence spectra of **MOZ-1**, **MOZ-4**, **MOZ-5**, **MOZ-7** and corresponding homogeneous controls were measured to characterize the electron transfer form Ir-PS to catalyst (hemin or MBA-Ir) upon light irradiation (Supplementary Fig. 14). The electron transfer between the photo-excited Ir-PS and the catalyst (hemin or MBA-Ir) as the quencher led to a decrease

of lifetime of photo-excited Ir-PS, which was determined by the electron transfer rate between the photo-excited Ir-PS and the catalyst. The quenching of the photo-excited Ir-PS by the catalyst was fitted with the following equation:

$$\frac{1}{\tau} = \frac{1}{\tau_0} + k[Q] \quad (10)$$

where τ_0 and τ are lifetime of photo-excited Ir-PS in the absence and presence of a catalyst as quencher (hemin or MBA-Ir), respectively; [Q] is the concentration of the catalyst (hemin or MBA-Ir); k is the quenching constant, representing the electron transfer rate. While a drastic decrease in lifetime was observed in **MOZ-1** with increased loading of Hemin ($k = 5.71 \times 10^{10}$ $M^{-1} \cdot s^{-1}$), a slower decrease in lifetime was observed when Hemin was added to Ir-PS ($k = 2.06 \times 10^{10}$ $M^{-1} \cdot s^{-1}$, Supplementary Fig. 14a-c). Similarly, **MOZ-5** with increased loading of MBA-Ir showed a much more drastic decrease in lifetime ($k = 8.75 \times 10^{9}$ $M^{-1} \cdot s^{-1}$) than Ir-PS with added MBA-Ir (k approaches 0 with no quenching, Supplementary Fig. 14d-f). These results show that the assembly of Ir-PS and catalysts (hemin or MBA-Ir) on MOZs significantly increases the electron transfer rate between them.

After Ur modification, **MOZ-4** ($\tau = 4.70$ μs) showed almost no change in lifetime in comparison to **MOZ-1** ($\tau = 4.52$ μs), indicating that Ur ligand was not involved in the electron transfer (matching with the proposed mechanism and the CV result in Supplementary Fig. 15, see discussion below). By contrast, after Am-Cl modification, **MOZ-7** ($\tau = 5.82$ μs) showed an obvious decrease in lifetime in comparison to **MOZ-1** ($\tau = 6.31$ μs), indicating that Am-Cl could also be oxidized by the photo-excited Ir-PS in **MOZ-7**. This observation is consistent with the proposed mechanism that Am-Cl ligands serves as an electron mediator in WOR and agrees with the CV result (Supplementary Fig. 15, see discussion below).

CVs: The redox potentials of functional components in MOZ-catalyzed CO_2RR (Ir-PS, hemin, and Ur) and MOZ-catalyzed WOR (Ir-PS, MBA-Ir, and Am-Cl) were separately determined by CV (Supplementary Fig. 15). Because the incorporation of these components in MOZs (through coordination to Hf_{12} SBUs) does not influence the electronic structures of their redox centers (e.g., porphyrin-Fe in hemin), their redox potentials in

the MOZs should remain the same as the homogenous systems. For MOZ-catalyzed CO_2RR, the reduced Ir-PS ([Ir-PS]/[Ir-PS]$^-$, -1.56 V vs. SCE) can drive two-electron reduction of hemin (Fe^{III} to Fe^{I} in hemin, -0.19 V, -1.06 V, and -1.64 V vs. SCE for Fe^{III}/Fe^{II}, Fe^{II}/Fe^{I}, and Fe^{I}/Fe^{0} in hemin, respectively), matching well with the above EPR result showing the Fe^{I} signal (Supplementary Fig. 16, see discussion below). Moreover, the Ur ligands showed no reduction peak, agreeing with the above time-resolved fluorescence spectra (Ur in **MOZ-4** did not quench the photo-excited Ir-PS). For MOZ-catalyzed WOR, the oxidized Ir-PS ([Ir-PS]$^+$/[Ir-PS], 1.67 V vs. SCE) can drive the oxidation of both MBA-Ir ([MBA-Ir]$^+$/[MBA-Ir]), 1.55 V vs. SCE) and Am-Cl ([Am-Cl]$^+$/[Am-Cl], 1.59 V vs. SCE), which shows that Am-Cl ligand serves as an electron mediator. This interpretation is supported by the above time-resolved luminescence spectra (Am-Cl in **MOZ-7** quenched the photo-excited Ir-PS).

Supplementary Note 7. Proposed mechanism of photocatalytic CO_2-to-CH_4 Conversion

In MOZs, the reduction potentials of Ir-PS ([Ir-PS]*, [Ir-PS]$^-$, and [Ir-PS]$^+$ refer to the photo-excited Ir-PS, reduced Ir-PS, and oxidized Ir-PS, respectively) were measured to be -0.63 V and -1.56 V *vs*. SCE for [Ir-PS]$^+$/[Ir-PS]* and [Ir-PS]/[Ir-PS]$^-$, respectively (Supplementary Fig. 15)[66]. The reduction potentials of hemin [Hemin(Fe^{III}), Hemin(Fe^{II}), Hemin(Fe^{I}), and Hemin(Fe^{0}) in this section refer to the hemin with the Fe oxidation status of +3, +2, +1, and 0, respectively] are measured to be -0.19, -1.06, and -1.64 V *vs*. SCE for Hemin(Fe^{III})/Hemin(Fe^{II}), Hemin(Fe^{II})/Hemin(Fe^{I}), and Hemin(Fe^{I})/Hemin(Fe^{0}), respectively (Supplementary Fig. 15)[67].

Fluorescence quenching studies showed that the excited [Ir-PS]* can be effectively quenched by both Hemin(Fe^{III}) and BIH (Supplementary Fig. 13). Their quenching behaviors are both well fitted with the Stern-Volmer equation though quenching by Hemin(Fe^{III}) was stronger (K_{SV} = 0.155 μM^{-1}) than that by BIH (K_{SV} = 0.057 μM^{-1}). Hemin(Fe^{III}) is thus proposed to first be reduced by [Ir-PS]* to generate Hemin(Fe^{II}) and [Ir-PS]$^+$,

upon which $[Ir\text{-}PS]^+$ is reduced to [Ir-PS] by BIH (only hemin-involving processes are listed in the Supplementary Equations 11-16):

$$Hemin(Fe^{III}) + [Ir\text{-}PS]^* \rightarrow Hemin(Fe^{II}) + [Ir\text{-}PS]^+ \quad (11)$$

The electron transfer from [Ir-PS]* to Hemin(Fe^{III}) in **MOZ-1** was further demonstrated by the time-resolved luminescent spectra, in which the increased loading of Hemin(Fe^{III}) in **MOZ-1** led to a decrease of the lifetime of [Ir-PS]* (Supplementary Fig. 14b, c).

Since [Ir-PS]* (-0.63 V *vs.* SCE) is not powerful enough to reduce the Hemin(Fe^{II}) and generate Hemin(Fe^{I}) (-1.06 V *vs.* SCE), this reduction is proposed to be proceed via $[Ir\text{-}PS]^-$ (-1.56 V *vs.* SCE, generated from BIH reduction of [Ir-PS]*):

$$Hemin(Fe^{II}) + [Ir\text{-}PS]^- \rightarrow Hemin(Fe^{I}) + [Ir\text{-}PS] \quad (12)$$

The generation of Hemin(Fe^{I}) in MOZs was confirmed by the EPR experiment (Supplementary Fig. 16). Under dark condition, the EPR signals of Hemin(Fe^{III}) in **MOZ-1** ($g_\perp$ = 5.87 and $g_\parallel$ = 1.97) were detected under N_2 (MOZ-1_N_2_Dark) with BIH (sacrificial agent). After 20-min light irradiation, the EPR signals of Hemin(Fe^{III}) disappeared and the EPR signals of Hemin(Fe^{I}) ($g_\perp$ = 2.30 and $g_\parallel$ = 1.91) appeared for **MOZ-1** under N_2 (MOZ-1_N_2_Light). This result shows that $[Ir\text{-}PS]^-$ can reduce Hemin(Fe^{III}) to Hemin(Fe^{I}) in **MOZ-1**.

Since $[Ir\text{-}PS]^-$ (-1.56 V *vs.* SCE) is not powerful enough to reduce Hemin(Fe^{I}) and generate Hemin(Fe^{0}) (-1.60 V *vs.* SCE), which combines with CO_2 to generate the reactive intermediate Hemin(Fe^{II})CO_2^{2-}, this reduction and associated CO_2 binding is proposed to go through a synergistic pathway (The proposed PCET and H-bond stabilization pathways in this work may decrease the reduction potential needed for this synergistic process):

$$Hemin(Fe^{I}) + [Ir\text{-}PS]^- + CO_2 \rightarrow Hemin(Fe^{II})CO_2^{2-} + [Ir\text{-}PS] \quad (13)$$

This electron transfer from Hemin(Fe^{I}) to CO_2 was confirmed by the EPR experiment (Supplementary Fig. 16). Under dark condition, the EPR signals of Hemin(Fe^{III}) in **MOZ-1** were detected in CO_2 (MOZ-1_CO_2_Dark) atmosphere with BIH (sacrificial agent). After 20-min light irradiation, the EPR signals of Hemin(Fe^{III}) disappeared, but the EPR signals of Hemin(Fe^{I}) (observed in N_2 atmosphere) were not detected. This observation can be explained by the fact that the electron transfer from Hemin(Fe^{I}) to CO_2 to generate diamagnetic Hemin(Fe^{II}) in Hemin(Fe^{II})CO_2^{2-}. The generation of Hemin(Fe^{II})CO_2^{2-} as the reactive intermediate was studied by DFT calculation (Supplementary Fig. 19, Supplementary Note 10).

The generated reactive intermediate Hemin(Fe^{II})CO_2^{2-} is doubly protonated to generate Hemin(Fe^{II})CO (the CO in Hemin(Fe^{II})CO could release as an intermediate product) and H_2O:

$$\text{Hemin}(Fe^{II})CO_2^{2-} + 2H^+ \rightarrow \text{Hemin}(Fe^{II})CO + H_2O \quad (14)$$

The generated Hemin(Fe^{II})CO was detected by FTIR (Supplementary Fig. 17). To exclude the interference of light irradiation, we used sodium anthracenide as a chemical reductant to replace [Ir-PS]*. We first studied the homogeneous Hemin system. The signal of Hemin(Fe^{II})-bound CO (corresponding to the stretch of C≡O) was expected at ~1950 cm^{-1}, according to the reported analogous systems.[68] As a positive control, when saturated CO was added to the partially reduced Hemin (Hemin*, one equivalent of sodium anthracenide was added to partially reduce Fe^{III} to Fe^{II} in Hemin), a signal at 1956 cm^{-1} was observed and assigned to Hemin(Fe^{II})-bound CO (Hemin* + CO group). This signal was also observed in the fully reduced Hemin (Hemin_R, three equivalents of sodium anthracenide were added to fully reduce Fe^{III} to Fe^{0} in Hemin) with saturated CO_2 (Hemin_R + CO_2), indicating the reduction of CO_2 by the Hemin_R to generate Hemin(Fe^{II})-bound CO as the intermediate. In contrast, the signal at 1956 cm^{-1} was not observed in either Hemin with saturated CO_2 (Hemin + CO_2) or fully reduced Hemin only (Hemin_R). Furthermore, this signal shifted to 1910 cm^{-1} in fully reduced Hemin with $^{13}CO_2$ (Hemin_R + $^{13}CO_2$), corresponding to the Hemin(Fe^{II})-bound ^{13}CO. The signal shift between Hemin(Fe^{II})-bound CO (1956 cm^{-1}) and Hemin(Fe^{II})-bound ^{13}CO (1910 cm^{-1}) matched well with the previously

reported result (1951 cm^{-1} in Hemoglobin-bound CO to 1907 cm^{-1} in Hemoglobin-bound ^{13}CO).[69] Similar results were also observed in **MOZ-1**. The signals at 1956 cm^{-1} and 1910 cm^{-1} were observed in the fully reduced **MOZ-1** with saturated CO_2 (MOZ_1_R + CO_2) and $^{13}CO_2$ (MOZ_1_R + $^{13}CO_2$), respectively, confirming the Hemin(Fe^{II})-bound CO was an observable intermediate in MOZ-catalyzed CO_2RR.

Hemin(Fe^{II})CO undergoes a two-electron (from $[Ir\text{-}PS]^-$) and one-proton reduction to generate the active intermediate Hemin(Fe^{I})CHO: Generated Hemin(Fe^{I})CHO then undergoes a four-electron (from $[Ir\text{-}PS]^-$) and five-proton reduction to release CH_4 as the target product alongside H_2O while regenerating Hemin(Fe^{II}):

$$\text{Hemin}(Fe^{II})\text{CO} + 2[\text{Ir-PS}]^- + H^+ \rightarrow \text{Hemin}(Fe^{I})\text{CHO} + 2[\text{Ir-PS}] \quad (15)$$

$$\text{Hemin}(Fe^{I})\text{CHO} + 4[\text{Ir-PS}]^- + 5H^+ \rightarrow \text{Hemin}(Fe^{II}) + 4[\text{Ir-PS}] + CH_4 + H_2O \quad (16)$$

The MOZ-catalyzed CO to CH_4 conversion was demonstrated using CO as substrate. The protocol of photocatalytic CO reduction by MOZs was similar to that of CO_2RR by MOZ with a CO/N_2 mixture (1:9) as the substrate. As shown in Supplementary Fig. 22, MOZs mediated the photocatalytic CO to CH_4 conversion with a higher CH_4 production efficiency, further supporting CO was the intermediate in CO_2 to CH_4 conversion. Moreover, when $^{13}CO_2$ was used as the substrate, the sequential generation of ^{13}CO and $^{13}CH_4$ were confirmed by GC-MS; when CF_3CD_2OD was used as the proton source, the generation of CD_4 was confirmed by GC-MS (Supplementary Note 5). All of these results agree with the proposed six-electron and six-proton process of CO to CH_4 conversion. Lastly, the generation of Hemin(Fe^{I})CHO as the reactive intermediate was studied by DFT calculations (Supplementary Fig. 19, Supplementary Note 10).

Supplementary Note 8. Kinetic study of MOZ-catalyzed CO_2RR

We have provided kinetic data of **MOZ-4** catalyzed CO_2RR to support our proposed mechanism (Supplementary Fig. 12). The original reaction conditions were 0.1 μM hemin (corresponding to 12.5 μM Ir-PS photosensitizer in **MOZ-4**), 100 mM TFE as proton source, 50 mM BIH as sacrificial reductant, 1 bar of CO_2 at room temperature (~25 ℃, controlled by the fan) upon irradiation of 300 W Xe lamp with 300-nm cutoff (the

light intensity was measured to be 1.2 W/cm^2) for 6 hours. CO_2, TFE, and BIH were in large excess of hemin, and so their depletion during early-stage reaction is assumed to be negligible, as confirmed by the linear time-dependence of TON of CO over time. Therefore, we used the TON of CO in a 6-hour reaction to calculate the reaction rate in our kinetic study. **MOZ-4** catalyzed CO_2RR showed a first-order dependence on CO_2 pressure (Supplementary Fig. 12b), second-order dependence on TFE concentration (Supplementary Fig. 12c), and first-order dependence on light intensity (driving force to excited Ir-PS photosensitizers to provide electron to hemin, Supplementary Fig. 12d). Besides, the TON of CO showed a zeroth-order dependence on hemin concentration (Supplementary Fig. 12e), corresponding to a first-order dependence CO_2RR rate catalyzed by of **MOZ-4** on hemin concentration (the CO generation was divided by hemin concentration for TON calculation). These results correspond with our proposed mechanism as shown in Supplementary Fig. 12a. The first two electron reduction of hemin (displayed by Fe^{III}) to generate Fe^{I} is energy favorable and relatively fast. The rate-limiting step will likely be a PCET ($Fe^{I} + e^{-} + CO_2 + 2H^{+} \rightarrow Fe^{II}CO + H_2O$) where the CO_2-bound hemin ($Fe^{II}CO_2^{2-}$) is proposed to be the potential intermediate. This mechanism further explains why Glu in **MOZ-2** may serve as proton donor facilitate the CO_2 reduction while Asn and Ur in **MOZ-3** and **MOZ-4** may H-bond to stabilize intermediates to facilitate the CO_2 reduction. Finally, a normal kinetic isotopic effect (KIE) of 6.42 ± 0.16 was obtained with CF_3CH_2OH/CF_3CD_2OD as the proton source at a concentration of 1.25 mM, further suggesting that protonation is involved in the rate-limiting step.

Supplementary Note 9. Reactivity comparison between MOZ-1 and its homogeneous analogue

To further compare the reactivity between **MOZ-1** and its homogeneous analogue (hemin + Ir-PS) we performed additional CO_2RR with increased concentrations of photosensitizer and hemin (Supplementary Fig. 12f). Hemin concentrations of 0.1, 0.5, 2.5, and 5.0 μM and corresponding Ir-PS concentrations of 1.25, 6.25, 31.25, and 62.5 μM respectively, were chosen. Reactions were performed for 6 hours. In homogenous analogues, although TON of CO_2RR ($CO+CH_4$) increased from 81 at 0.1 μM hemin to 178 at 0.5 μM hemin, it decreased

to 152 at 2.5 μM hemin and 103 at 5.0 μM hemin. This is likely due to saturation of light absorption of photosensitizer at high concentration, a major limitation for other photocatalysis broadly. In contrast, **MOZ-1** showed a concentration *independent* TON at low concentration (0.1 to 2.5 μM hemin) because local concentration of photosensitizer and hemin (i.e., the distance between photosensitizer and hemin) in **MOZ-1** is constant. The TON of CO_2RR for **MOZ-1** also decreased at high concentration (5.0 μM) likely due to the light absorption saturation. Even at 0.5 μM hemin, however, **MOZ-1** showed a 4.9-fold increase in TON compared to that of homogenous analogue. We believe these experiments demonstrate another strength of MOZs as photocatalysts insofar as even at low concentration of photosensitizer and hemin **MOZ-1** harvests light more effectively by maintaining a high local concentration of photosensitizer and hemin.

Supplementary Note 10. DFT calculation of MOZ-catalyzed CO_2RR

DFT calculations utilized the density functional methods implemented in Gaussian 16 (revision C.01)[70]. We relied upon unrestricted B3LYP-D3 methods[71]. The 6-31G* basis set was used for light atoms (e.g. C, H, O, N, F)[72] while the LANL2DZ basis set was used for Fe with effective core potentials (ECPs) for preliminary screening of conformations and spin states[73,74]. The self-consistent field was set to quadratically converge with an extra step if the first order SCF would not converge (SCF=XQC). Geometries of all models were optimized in the gas phase on the basis of experimental X-ray structures. Gibbs free energy was calculated using zero-point energy and thermal corrections. All conformations were geometrically optimized to the energy minimum. Frequency calculations and natural charge calculation were performed on the optimized structures with the same basis set and level of theory.

To simplify calculations, a Zr_6 cluster capped by formate was used to model the active cites in **MOZ-3** and **MOZ-4**. This simplification had three justifications: (1) Each active site composes only one face of component Hf_{12} clusters in MOZs, and so Hf_{12} clusters could be simplified to Hf_6 clusters [$Hf_6(\mu_3\text{-}O)_4(\mu_3\text{-}OH)_4$], half of the Hf_{12} clusters; (2) Hf has very similar chemical properties and electronic structures to Zr, and so Hf_6 cluster could

be further simplified to the Zr_6 cluster [$Zr_6(\mu_3\text{-}O)_4(\mu_3\text{-}OH)_4$]; (3) The capping organic ligands on this Zr_6 cluster have minimal effect on the energy calculation as previously reported[75], and so the capping ligand of this Zr_6 cluster was simplified to formate with the formulation of $Zr_6(\mu_3\text{-}O)_4(\mu_3\text{-}OH)_4(HCOO)_{12}$[76].

The geometries of hemin, Asn, and Ur were first optimized in the gas phase on the basis of their experimental X-ray structures. The hemin-capped Zr_6 cluster was chosen as the model to represent the starting coordination environment of the Fe catalytic site. The geometry of the two crucial reactive intimidates during the CO_2-to-CH_4 conversion ($Fe^{II}CO_2^{2-}$ and $Fe^{I}CHO$, as shown in Fig. 4c and Supplementary Fig. 19f) for **MOZ-3** (denoted by Asn-$FeCO_2$ and Asn-FeCHO) and **MOZ-4** (denoted by Ur-$FeCO_2$ and Ur-FeCHO) were optimized as quintets as previously reported[71] and triplets, respectively, by the B3LYP under unrestricted open-shell calculation (Fig. 4c). An AA-free version of these reactive intimidates (denoted by NA-$FeCO_2$ and NA-FeCHO) were optimized as controls. The Cartesian coordinates of these optimized structures are listed in Supplementary Data 1. The stabilization enthalpy (ΔH_{stb}) by the H-bonds in **MOZ-3** or **MOZ-4** were thusly defined as the enthalpy difference between the reactive intermediates in **MOZ-3** (Asn-$FeCO_2$ and Asn-FeCHO) or **MOZ-4** (Ur-$FeCO_2$ and Ur-FeCHO) and their corresponding controls (NA-$FeCO_2$ and NA-FeCHO, respectively).

As shown in Supplementary Fig. 19, based on these optimized structures, the extent of interaction between Fe and bound CO_2 in $FeCO_2^{2-}$ reactive species can be ascertained by the length of Fe-C bond and the angle of ∠O-C-O. A shorter Fe-C bond length and a narrower ∠O-C-O angel indicated a stronger back bonding from Fe to bound CO_2, leading to a stronger interaction between Fe and bound CO_2, corresponding to a better activation of CO_2. In the case of NA-$FeCO_2$, the CO_2 binds to the Fe center in an η_2-mode, with the Fe-C bond length computed to be 2.19 Å and the ∠O-C-O angle computed to 150.0°. This angle is substantially lower than that in free CO_2 (180°), suggesting substantial pi-backbonding from Fe to CO_2 in NA-$FeCO_2$. Asn-$FeCO_2$ presented a slightly stronger pi-backbonding from Fe to CO_2 with Fe-C bond length decreased to 2.10 Å and the ∠O-C-O angle decreases to 145.9°. This slightly stronger interaction between Fe and bound CO_2 in Asn-$FeCO_2$

was attributed to the moderate H-bond (1.96 Å) between the -NH fragment of Asn and oxygen atom of bound CO_2, leading to a ΔH_{stb} of -14.1 kcal·mol^{-1}. In the case of Ur-FeCO_2, due to two strong H-bonds between the -NH fragments of Ur and each oxygen atom of bound CO_2 (1.85 Å and 1.91 Å, ΔH_{stb} of -23.5 kcal·mol^{-1}), even stronger pi-backbonding from Fe to bound CO_2 was observed with the Fe-C bond length further decreased to 2.04 Å while the ∠O–C–O angle narrowed to 136.2°. Indeed, the natural population analysis (NPA) charge on bound CO_2 is -0.29, -0.38, and -0.56 in NA-FeCO_2, Asn-Fe$^{II}CO_2$, and Ur-FeCO_2, respectively. The more negative NPA charge on bound CO_2 in Asn-FeCO_2 and Ur-FeCO_2^- was because that H-bonding from the Asn and Ur to the bound CO_2 promoted the electron density transfer from Fe to bound CO_2.

A similar trend of the interaction between Fe and bound CHO was also observed in the optimized structures of FeCHO, as mainly reflected by the Fe-C bond length. NA-FeCHO, Asn-FeCHO, and Ur-FeCHO presented a Fe-C length of 2.02 Å, 1.88 Å, and 1.86 Å, the NPA charge of the bound CHO is -0.31, -0.36 and -0.43 respectively. This decreasing Fe-C length was attributed to the H-bond stabilization between the oxygen in CHO and the -NH fragments in Asn (2.02 Å, ΔH_{stb} of -9.1 kcal·mol^{-1}) or in Ur (1.88 Å, 2.23 Å, ΔH_{stb} of-17.2 kcal·mol^{-1}).

Supplementary Note 11. Amide ligands for CO_2RR

To further confirm H-bonding improves CO_2RR reactivity in **MOZ-3** and **MOZ-4,** from Asn and Ur, respectively, we synthesized two additional amide ligands with a single −NH fragment (Am-1) or no −NH fragment (Am-2, Supplementary Fig. 23a, Supplementary Method, Supplementary NMR spectra). We modified these ligands onto the **MOZ-1** to obtain two additional MOZ variants: **MOZ-1**-Am-1 and **MOZ-1**-Am-2. DFT calculation indicated that Asn in **MOZ-3** and Ur ligand in **MOZ-4** could provide one and two H-bonds, respectively, to stabilize CO_2 and CO intermediates and enhance reactivity compared to **MOZ-1**. Under similar 6-hour reaction condition, as expected, the TON of CO of **MOZ-1**-Am-1 decreased from 2704 ± 137 (**MOZ-4**) to 1262 ± 270, which is similar to that of **MOZ-3** (1545 ± 66). Moreover, the TON of CO of **MOZ-1**-Am-2

further decreased to 457 ± 98, similar to that of **MOZ-1**(435 ± 31, Supplementary Fig. 23b). A similar reactivity pattern of **MOZ-1**-Am-1 and **MOZ-1**-Am-2 was also found in CH_4 production (Supplementary Fig. 23c). These results demonstrate that −NH fragments in these urea and amide ligands improve reactivity of CO_2RR in MOZs. Since the pKa values of these −NH fragments are very high (~13.9) these fragments are unlikely to function as proton donors, and so we propose these Ur and amide ligands operate through a H-bonding mechanism.

Supplementary Note 12. WOR product detection

For MOZ-catalyzed WOR, the generated O_2 was detected by FID. The full GC traces of MOZ-catalyzed WOR (6-hour reaction, three replicates for each MOZ) are provided as an example (Supplementary Fig. 27a). O_2 was detected at a retention time of 0.90 min by FID (Supplementary Fig. 27a). The calibration curve of O_2 by FID was generated (Supplementary Fig. 27b).

The gas products of MOZ-catalyzed WOR were confirmed by GC-MS (Supplementary Fig. 10). The full GC-MS traces of MOZ-catalyzed WOR (represented by **MOZ-7** in triplicate, 6-hour reaction) are provided as an example (Supplementary Fig. 10b). O_2 was detected at a retention time of 1.58 min (Supplementary Fig. 10b). The calibration curve was generated for O_2 (Supplementary Fig. 10e). After 6-hour reaction, the TON of O_2 for **MOZ-7** catalyzed WOR was determined to be 1290 ± 169 by GC-MS, which is close to that (1443 ± 67 for O_2) determined by GC. The slight difference between the TON numbers determined by GC-MS and GC may be caused by the catalytic activity difference in different batches of **MOZ-4**.

Furthermore, MOZ-catalyzed WOR was caried out with $H_2{}^{18}O$ (oxygen source) and the corresponding isotope-labeled products were detected by GC-MS (Supplementary Fig. 11). Under normal $H_2{}^{16}O$, $^{16}O_2$ (m/z of 32) was detected in **MOZ-7** catalyzed WOR at a retention time of 1.58 min (Supplementary Fig. 11b). Under $H_2{}^{18}O$, $^{18}O_2$ (m/z of 36) was detected at the same retention time (Supplementary Fig. 11d). These results demonstrate H_2O as the source of O_2 generated in MOZ-catalyzed WOR.

Supplementary Note 13. Proposed mechanism of MOZ-catalyzed WOR

As reported, the $[Ir(bpy)(Cp^*)Cl]^+$ derived catalyst in MOFs was first oxidized to be $[Ir(bpy)(H_2O)_2(X)Cl]$ (X = $HCOO^-$ or CH_3COO^-) before it could catalyze water oxidation[77]. In this process, the Cp* group was oxidized to either formate or acetate group to form the active catalyst for water oxidation reaction. The generated $[Ir(bpy)(H_2O)_2(X)Cl]^+$ in MOFs cannot be further oxidized to IrO_2 nanoparticle as they are isolated in the MOFs. In MOZ-catalyzed water oxidation reaction, the active catalyst was determined to be $[Ir(MBA)(H_2O)_2(CH_3COO)Cl]^+$ (MBA-Ir*), as revealed by the HR-MS (Supplementary Fig. 28c). The **MOZ-5** was recovered by centrifugation after the 6-hour photocatalytic water oxidation reaction and digested by concentrated HCl. The peak corresponding to Ir-PS ($[M]^+$ = 1105.144), unreacted H-MBA-Ir with a formula of $[Ir(MBA)(Cp^*)Cl]^+$ ($[M]^+$ = 575.125), and reactive catalyst H-MBA-Ir* with a formula of $[Ir(MBA)(H_2O)_2(CH_3COO)Cl]^+$ ($[M]^+$ = 565.0728) were clearly observed. The mechanism of MOZ-catalyzed WOR was thusly proposed based on MBA-Ir* catalyst as shown in the Supplementary Fig. 28f.

Luminescence quenching studies showed that the excited Ir-PS* was effectively quenched by both MBA-Ir and $K_2S_2O_8$ (Supplementary Fig. 28a, b) and their quenching behaviors were both well fitted with Stern-Volmer equation. The quenching of Ir-PS* by $K_2S_2O_8$ had a larger Stern-Volmer slope (K_{SV} = 0.281 μM^{-1}) than that by MBA-Ir (K_{SV} = 0.048 μM^{-1}), indicating the Ir-PS* was first oxidized by $K_2S_2O_8$ to generate Ir-PS^+ before it could oxidize MBA-Ir to drive the WOR. Therefore, the redox pair Ir-PS^+/Ir-PS (E = 2.00 V vs SHE) was used to calculate the energy diagram of MOZ-catalyzed photocatalytic WOR in DFT calculation.

The mechanism of MBA-Ir* catalyzed WOR in **MOZ-5** was proposed as shown in Supplementary Fig. 28f and its energy diagram was optimized by DFT calculation (Fig. 5d). Initially, a water molecule is weakly adsorbed on Ir^{III} (the MBA-Ir* was simplified as Ir in the following discussion) to form the Ir^{III}-H_2O as initial state (IS, ΔG of IS was normalized to 0 kcal/mol). Subsequently, the $[Ir^{III}\text{-}H_2O]^{+1}$ underwent a PCET step to form $[Ir^{IV}\text{-}OH]^{+1}$ as the first intermediate (IM_1, −21.6 kcal/mol). This step involved the first transition state (TS_1)

where the oxygen atom of a water molecule attacked the hydrogen atom of the Ir^{IV}-bound water ($[Ir^{IV}\text{-}OH_2]^{+2}$, −20.7 kcal/mol) to release a proton in the form of H_3O^+. Then, the $[Ir^{IV}\text{-}OH]^{+1}$ underwent a second PCET step to from the Ir-oxo complex $[Ir^{V}{=}O]^{+1}$ as the second intermediate (IM_2, −38.2 kcal/mol). This step involved the second transition state (TS_2) where the oxygen atom of a water molecule attacked the hydrogen atom of the $[Ir^{V}\text{-}OH]^{+2}$ (−11.2 kcal/mol) to release another proton in the form of H_3O^+, corresponding to a Gibbs free energy of 10.4 kcal/mol. As reported, thusly formed $[Ir^{V}{=}O]^{+1}$ was the active catalytic specie for the oxygen-oxygen bond formation[77,78]. This rather complex step of oxygen-oxygen bond formation involved the third transition state (TS_3) where the oxygen atom of a water molecule attacked the oxo moiety in IM_2 to give peroxo complex $[Ir^{III}\text{-}OOH_2]^{+1}$ (−32.5 kcal/mol), followed by the release of a proton via the $H^+(H_2O)_3$ cluster to generate $[Ir^{III}\text{-}OOH]^0$ as the third intermediate (IM_3, −63.0 kcal/mol). The $[Ir^{III}\text{-}OOH]^0$ underwent a third PCET step to form $[Ir^{IV}\text{-}OO]^0$ as the fourth intermediate (IM_4, −92.2 kcal/mol). This step involved the fourth transition state (TS_4) where the oxygen atom of a water molecule attacked the hydrogen atom of the $[Ir^{IV}\text{-}OOH]^0$ (-14.3 kcal/mol) to release a proton in the form of H_3O^+, corresponding to an activation energy of 48.7 kcal/mol. Finally, the $[Ir^{IV}\text{-}OO]^0$ was oxidized to $[Ir^{V}\text{-}OO]^0$ as the fifth intermediate (IM_5, −102.0 kcal/mol), followed by the release of a O_2 molecule to close the catalytic cycle.

The **MOZ-6** catalyzed WOR was proposed to undergo a similar process as above, while the Gln functioned as electron mediator to make this catalytic cycle energetically favorable. During the **MOZ-6** catalyzed the WOR, the Gln ($R = -CH_2CH_2CONH_2$) was first photo-oxidized to form $Gln^{\bullet+}$ ($R = -CH_2CH_2CONH^{\bullet+}$) through a PCET and thusly generated $Gln^{\bullet+}$ could oxidize H_2O-bound MBA-Ir* through hydrogen atom transfer (HAT) to drive WOR. In this case, the Gibbs free energy corresponding to the TS_2 decreased to −0.4 kcal/mol in **MOZ-6** from 10.4 kcal/mol in **MOZ-5**, respectively. Notably, the activation energy corresponding the oxygen-oxygen formation (the rate-determining step) dropped from 48.7 kcal/mol in **MOZ-5** to 8.4 kcal/mol in **MOZ-6**.

Supplementary Note 14. DFT calculation of MOZ-catalyzed WOR

All reaction intermediates and transition states were optimized using the B3LYP methods[79-81], as implemented in the Gaussian 16 program package[82]. The Grimme's D3 method was used to account for dispersion correction[83]. We used the SDD basis set for the Ir and Zr atoms and the 6-31+G(d) basis set for the H, C, N, O and Cl atoms. Solvent effects, including contributions of non-electrostatic terms, were accounted for by the SMD methods[84], using water as solvent. The corresponding gas energy E_{gas} calculation was based on the def2TZVP basis set to ensure accuracy. Analytic frequency calculations were performed on all optimized structures at the same level of theory, to identify all of the stationary points as minima (zero imaginary frequency $\varepsilon_{ZPE,gas}$) or transition states (one imaginary frequency) and to obtain Gibbs free energy corrections at 298.15 K, $G^{o}_{298\,K,gas}$. The solvation energies ΔG^{*}_{solv} were calculated as single point corrections on the optimized structures using the SMD[84] continuum solvation model employing def2-TZVP basis set at the M06-2X level. The experimental solvation free energy (-6.3 kcal/mol) and concentration correction at 298.15 K (4.3 kcal/mol was used as the standard state 55.6 M of the water solvent) of water were used, 1.89 kcal/mol concentration correction at 298.15 K was added for the other species. The standard Gibbs free energy in aqueous solution was concluded as Supplementary Equation 17:

$$G^{o}_{aq} = E_{gas} + \Delta G^{*}_{solv} + \varepsilon_{ZPE,gas} + G^{o}_{298\,K,gas} + Concentration\ correction \quad (17)$$

The calculation of reference energy of PCET in this work was according to the standard protocol and described as follows. For the calculation of one electron redox potential, the experimental absolute redox potential of standard hydrogen electrode (SHE) is used (4.281 V, 98.7 kcal/mol). As a result, the electron affinity of Ir-PS^{+}/Ir-PS (2.00 V vs SHE) was calculated to be 144.8 kcal/mol [(4.281 + 2.0) × 23.0605]. The standard free energy of proton in aqueous solution (in the form of H_3O^{+}) $G^{o}(H^{+}, aq)$ was estimated to be -270.3 kcal/mol[85] (the experimental $\Delta G^{o}_{gas}(H^{+})$ is -6.28 kcal/mol, the solvation free energy estimated -265.9 kcal/mol [86]). Therefore, the reference energy of PCET oxidation by Ir-PS^{+}/Ir-PS at pH=7 was calculated to be 424.6 kcal/mol (144.8+270.3+7×1.364).

Supplementary Note 15. Am-R ligands synthesis for MOZ-catalyzed WOR

To further confirm the mechanism of MOZ-catalyzed WOR and enhance the activity of MOZs for water oxidation reaction, we designed a series of amide-containing artificial ligands (Am-R) derived from 6-oxo-6-(phenylamino) hexanoic acid (Supplementary Fig. 29a). The synthetic route towards these ligands can be found in the Supplementary Method and the NMR spectra of these ligands in the Supplementary NMR Spectra. Through tuning the functional groups attached to the phenyl ring in these ligands (R = OCH_3, CH_3, H, F, Cl, Br, or NO_2) the oxidation potentials of the conserved amide group could be precisely adjusted from 2.00 to 1.56 V as determined by the CV, and 1.92 to 1.56 V based on our DFT calculation (Supplementary Fig. 29b). By modifying these artificial ligands onto **MOZ-5**, the generated MOZ library presented a volcano plot for WOR reactivity compared to oxidation potential of the amide in these ligands (Supplementary Fig. 29c). Since all Am-R ligands share the same amide groups, it is likely that WOR reactivity is modulated by oxidation potential, which further confirms their role as electron mediators. The highest WOR reactivity was achieved in **MOZ-7** (R = Cl, Am-Cl) with the 6-h turnover number (TON) of 1443 ± 67, representing a 15% enhancement over that of **MOZ-6** (TON of 1250 ± 264). The **MOZ-7** catalyzed WOR was proposed to undergo a similar process to that of **MOZ-6** as described in Supplementary Note 13, while the Am-Cl functioned as electron mediator to make this catalytic cycle energetically favorable. During **MOZ-7** catalyzed WOR, Am-Cl was first photo-oxidized to form Am-$Cl^{\bullet+}$ (the -NH fragment in Am-Cl was photo-oxidized to -$N^{\bullet+}$) through a PCET and thusly generated Am-$Cl^{\bullet+}$ could oxidize H_2O-bound MBA-Ir* through HAT to drive WOR (Supplementary Fig. 29d-e). In this case, the Gibbs free energies corresponding to the TS_2 decreased to −18.6 kcal/mol in **MOZ-7** from −0.4 kcal/mol in **MOZ-6** and 10.3 kcal/mol in **MOZ-5**, respectively. Notably, the activation energy corresponding to the oxygen-oxygen formation (the rate-determining step) dropped from 48.7 kcal/mol in **MOZ-5** and 8.4 kcal/mol in **MOZ-6** to 1.5 kcal/mol in **MOZ-7**.

Supplementary Note 16. Calculation of PCET reduction potentials for Am-R ligands

Standard redox potentials are related to the free energy of the transformation:

$$E^{o}_{red(aq)} = \frac{-\Delta G^{*}_{red(aq)}}{nF} \tag{18}$$

Where F is Faraday's constant, $\Delta G^{*}_{red(aq)}$ is the solution phase standard state free energy change, and *n* is the number of electrons in the redox process.

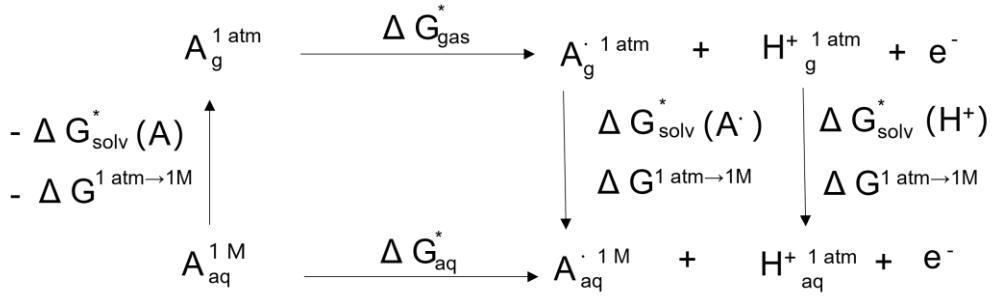

According to the thermodynamic cycle outlined above, $\Delta G^{*}_{red(aq)}$ is defined in the Supplementary Equation 19 for a PCET reduction process:

$$\Delta G^{*}_{red(aq)} = G^{*}_{(aq)}(A^{\bullet}) + G^{*}_{(aq)}(H^{+}) + G^{o}_{(g)}(e^{-}) - G^{*}_{(aq)}(A) \tag{19}$$

The standard state free energy is shown in the Supplementary Equation 20:

$$G^{*}_{(aq)} = \left(G^{o}_{(g)} + \Delta G^{1\,atm\rightarrow 1M}\right) + \Delta G^{*}_{solv} \tag{20}$$

The $\Delta G^{o}_{(g)}$ is the standard state free energy in the gas phase and ΔG^{*}_{solv} is the standard state free energy of solvation. $\Delta G^{1\,atm\rightarrow 1M}$ = 1.89 kcal/mol is the free energy difference for converting from the standard state concentration of 1 atm to the standard state concentration of 1 mol/L. The experimental Gibbs free energy (6.28 kcal/mol) and solvation free energy of a proton (−264.0 kcal/mol) were used. [87]

The gas phase free energies were calculated by CBS-QB3 compound model chemistry[88]. The solvation free energy was computed using the SMD implicit solvation free model[84] at the M05-2X/6-31G* level of theory. All calculations were carried out in Gaussian 16 with a solution phase of water.

Supplementary Figures

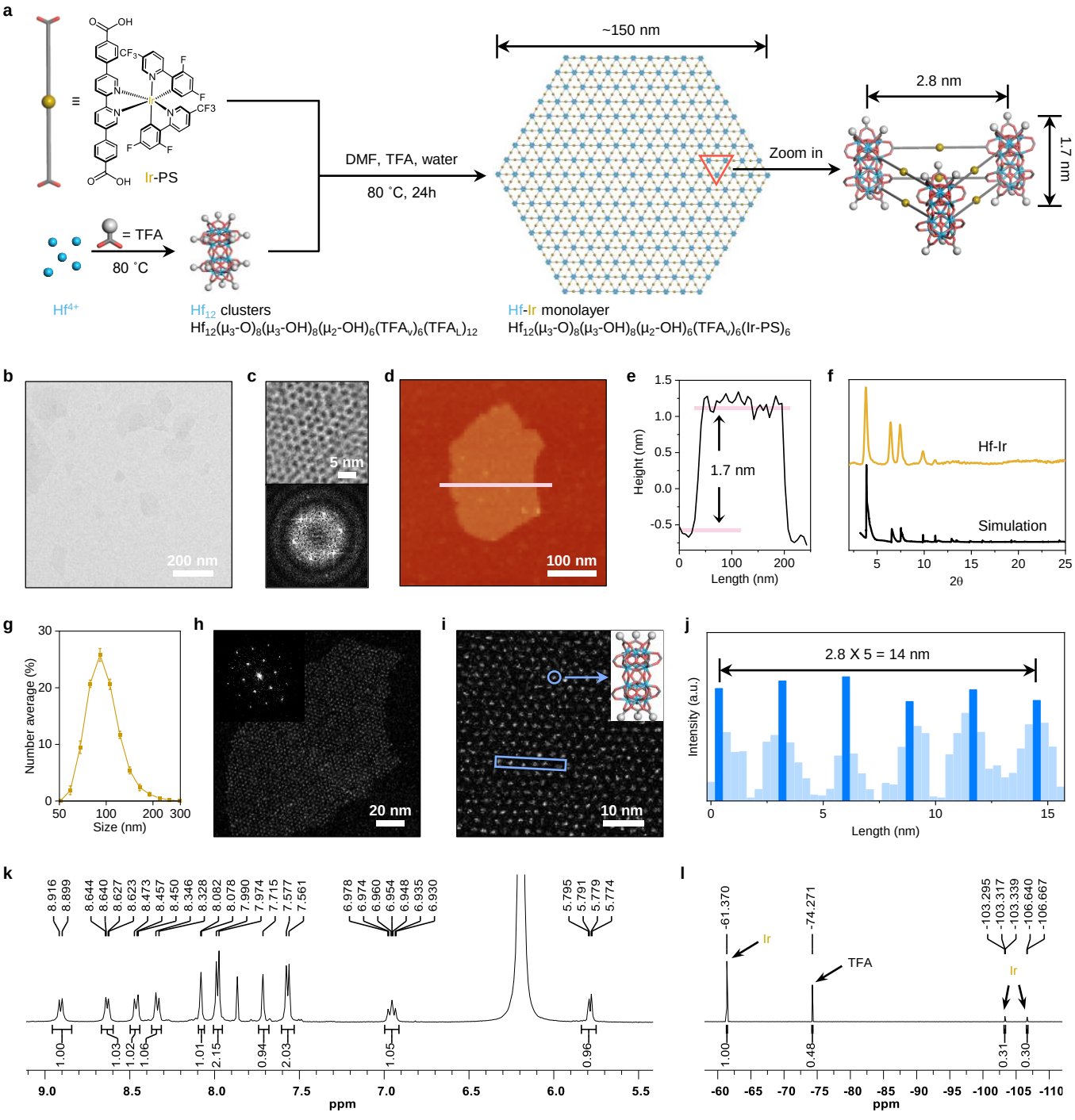

Supplementary Fig. 1. Hf-Ir monolayer. a, Schematic showing solvothermal synthesis and proposed structure and composition of Hf-Ir monolayer. A Hf_{12} cluster was first formed with TFA capping both vertically (TFA_v) and laterally (TFA_L). The TFA_L was further replaced by Ir-PS and the Hf_{12} cluster was thus regularly connected

to a 2D network. **b-j,** (**b**) TEM imaging, (**c**) HRTEM imaging (top) and fast Fourier transform (FFT) pattern (bottom), (**d**) AFM topography and (**e**) height profile, (**f**) PXRD pattern compared to that of simulated structure, (**g**) number-averaged diameters (99.1 ± 3.4 nm), (**h**) large-area HAADF imaging and FFT pattern (insert), and (**i**) small-area HAADF imaging and (**j**) intensity analysis of Hf-Ir monolayer. **k,** ^{1}H NMR spectrum of digested Hf-Ir monolayer. **l,** ^{19}F NMR spectrum of digested Hf-Ir monolayer, in which signals from left to right correspond to $-CF_3$ in Ir-PS, $-CF_3$ in TFA, −F in Ir-PS, and −F in Ir-PS. In **g**, data are presented as mean ± s.d. (n= 3) with the error bars representing the s.d.

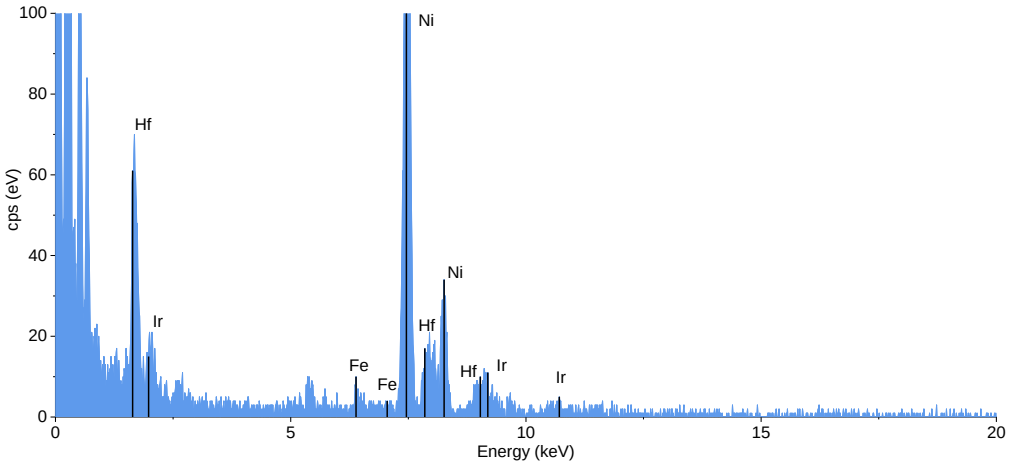

Supplementary Fig. 2. EDS spectrum of MOZ-1. Signals of Hf, Ir, Fe are clearly observed. Fe displays a relatively lower signal intensity due to both lower loading (Fe/Ir = 8% and Fe/Hf = 4%) and relatively lower sensitivity factor (counts) in the EDS mode. Ni was observed as sample was drop-casted onto carbon coated nickel grids.

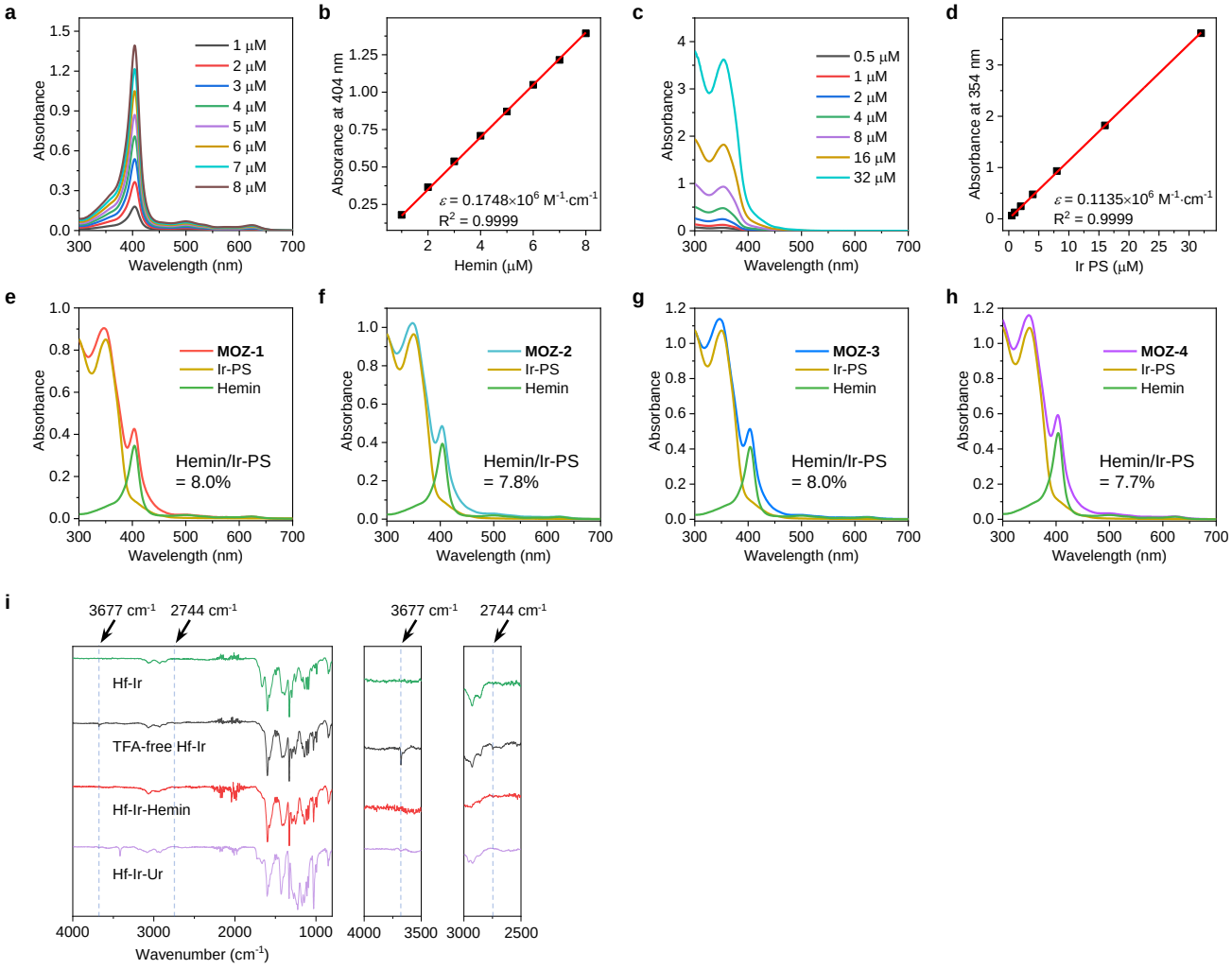

Supplementary Fig. 3. UV-Vis and IR analysis of MOZs. a, b, (**a**) Standard absorption curves of hemin in DMF and (**b**) linear fit of absorptions at 404 nm vs. concentrations (ε = 0.1748 × 10^6 M^{-1}·cm^{-1}, R^2 = 0.9999). **c, d,** (**c**) Standard absorption curves of Ir-PS in DMF and (**d**) linear fit of absorptions at 354 nm vs. concentrations (ε = 0.1135 × 10^6 M^{-1}·cm^{-1}, R^2 = 0.9999). **e-h,** Absorption curves of (**e**) **MOZ-1**, (**f**) **MOZ-2**, (**g) MOZ-3**, and (**h**) **MOZ-4**. Each of these absorption spectra was quantitively deconvoluted into the separate absorption of hemin and Ir-PS. The concentration of hemin and Ir-PS in each MOZ was determined by their standard curves and the ratio of hemin to Ir-PS was thus calculated to be 8.0%, 7.8%, 8.0%, and 7.7% for **MOZ-1**, **MOZ-2**, **MOZ-3**, and **MOZ-4**, respectively. This is consistent with a hemin to Ir-PS ratio of ~8.0%, verifying that hemin is not replaced by Glu, Asn, or Ur in **MOZ-2**, **MOZ-3**, or **MOZ-4**, respectively. **i,** FTIR spectra of Hf-Ir, TFA-

free Hf-Ir, Hf-Ir-Hemin, and Hf-Ir-Ur. Two dashed lines refer to the signals of the terminal Hf-OH at 3677 cm^{-1} and the H-bonded Hf-H_2O at 2744 cm^{-1} on Hf SBUs, respectively.

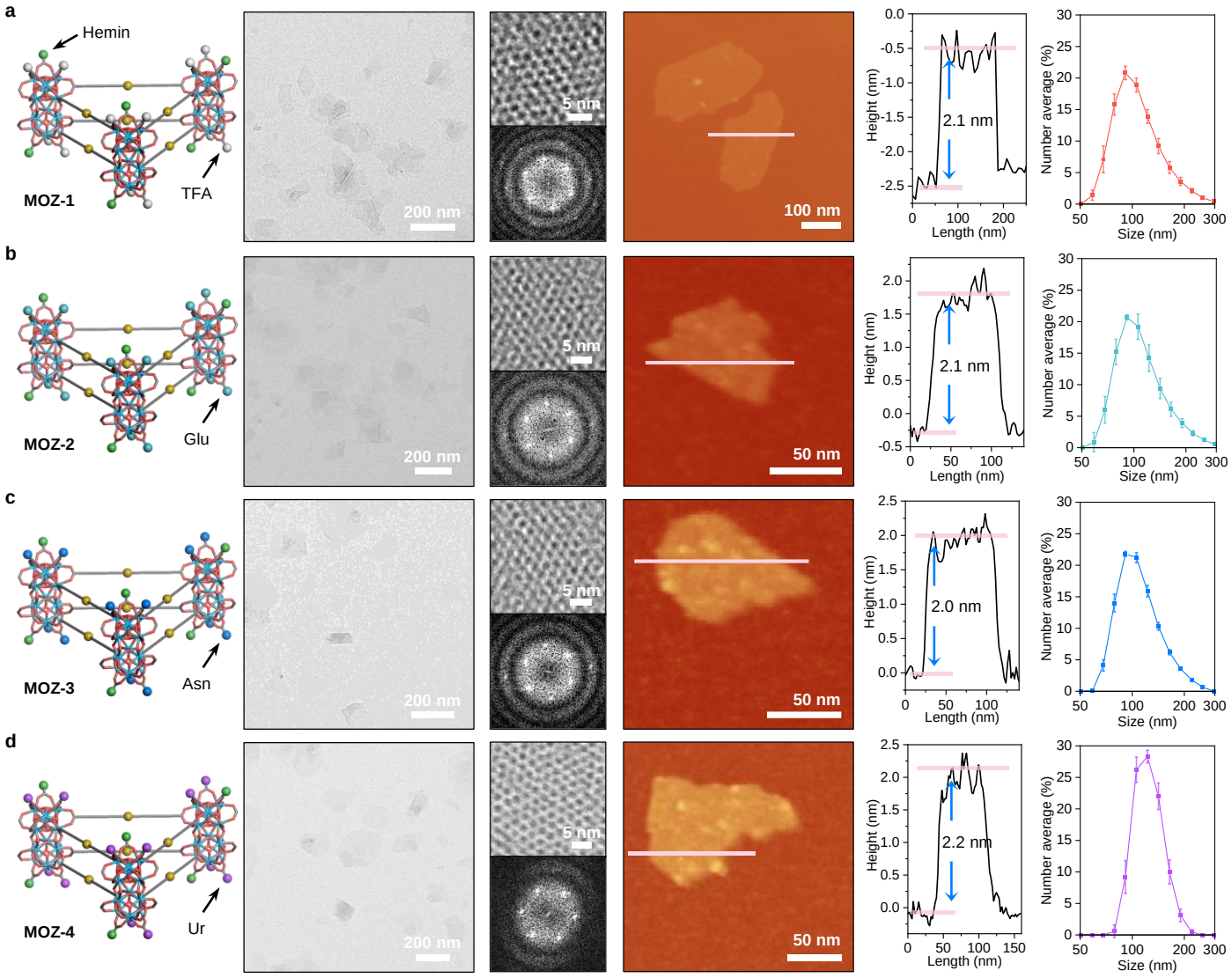

Supplementary Fig. 4. Morphological characterization of MOZs. a-d, Morphological characterization of (**a**) **MOZ-1**, (**b**) **MOZ-2**, (**c**) **MOZ-3**, and (**d**) **MOZ-4**. For each, from left to right: modeled structure, TEM imaging, HRTEM imaging (top) and its FFT pattern (bottom), AFM topography, height profile, and number-averaged diameter as measured by DLS. Number-averaged diameters were measured to be 112.5 ± 9.5 nm, 114.9 ± 5.7 nm, 113.9 ± 5.6 nm, and 125.5 ± 3.6 nm for **MOZ-1**, **MOZ-2**, **MOZ-3**, and **MOZ-4**, respectively. DLS data are presented as mean ± s.d. (n= 3) with the error bars representing the s.d.

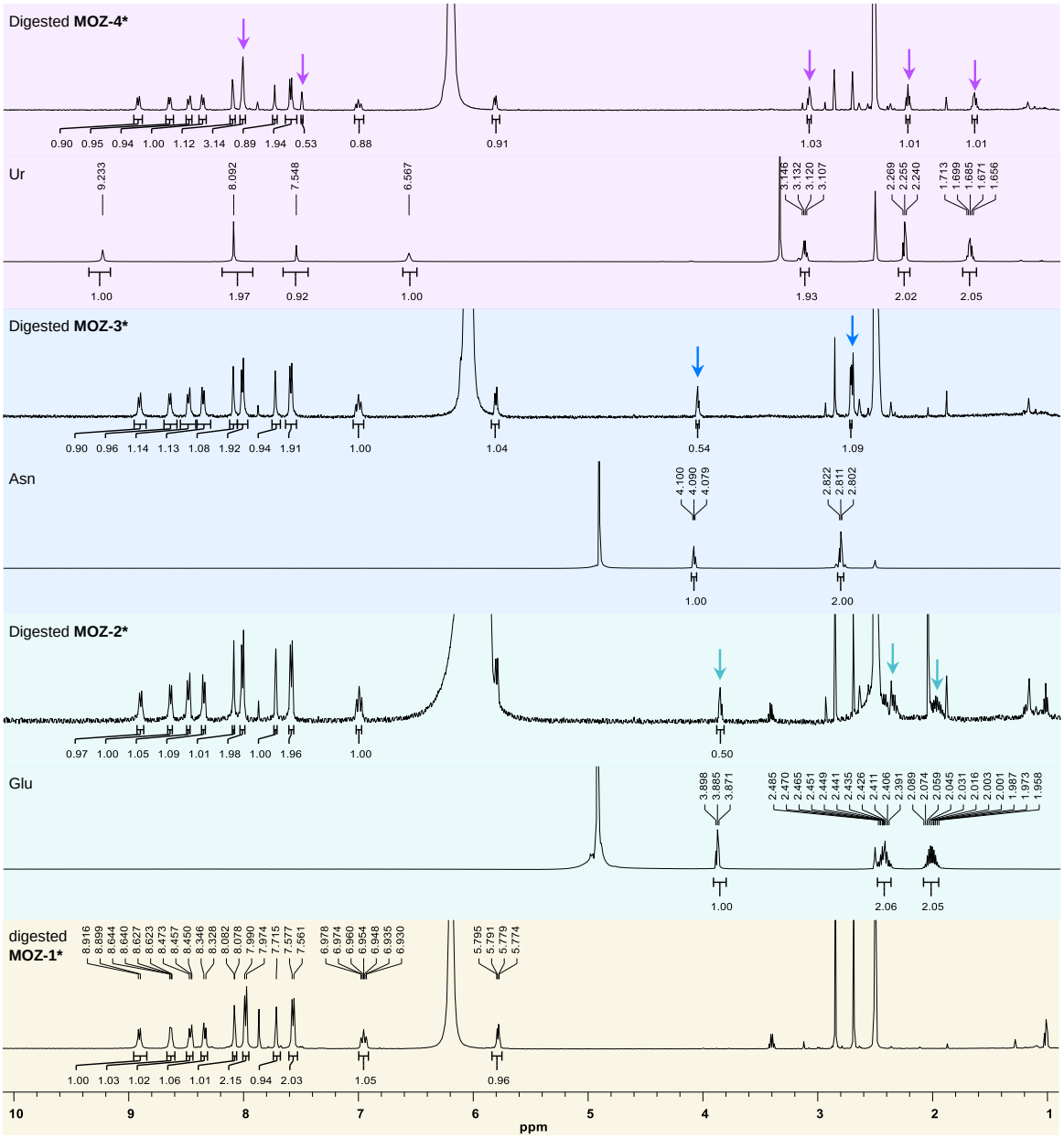

Supplementary Fig. 5. NMR analysis of MOZs. From bottom to top: ^{1}H NMR spectra of digested **MOZ-1***, Glu, digested **MOZ-2***, Asn, digested **MOZ-3***, Ur, and digested **MOZ-4***. MOZ* refers to a hemin-free analogue of an MOZ, designed to prevent the paramagnetic hemin from obscuring the NMR spectra. Ir-PS signals were found in all the MOZs*, while Glu, Asn, and Ur signals were only observed in **MOZ-2***, **MOZ-3***, and **MOZ-4***, respectively. NMR signals of Ur ligand corresponding to amine protons (9.233 and 6.567 ppm) were not observed in the digested **MOZ-4*** due to a strong acidic digestion condition. A 1:2 NMR signal

ratio of Ir-PS to Glu, Asn, or Ur was observed in **MOZ-2***, **MOZ-3***, and **MOZ-4***, respectively, corresponding to a 1:1 molar ratio of Glu, Asn, or Ur to Ir-PS. These results demonstrate that Glu, Asn, and Ur can fully replace the capped TFA during the synthesis of **MOZ-2**, **MOZ-3**, and **MOZ-4**.

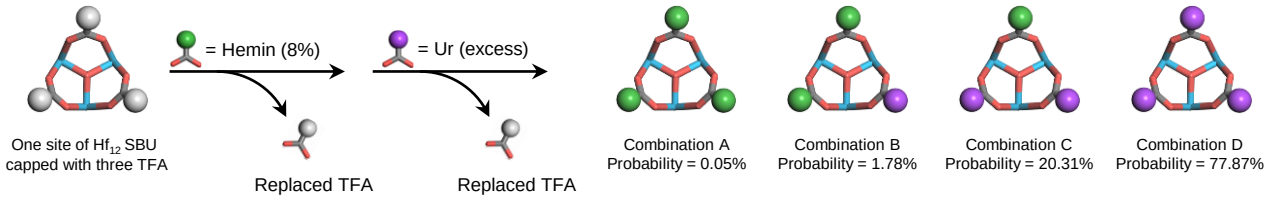

Supplementary Fig. 6. Active sites in MOZs. Schematic showing the post-modification process for **MOZ-4** and the potential combinations of Hemin and Ur on the Hf_{12} SBU and their corresponding probability.

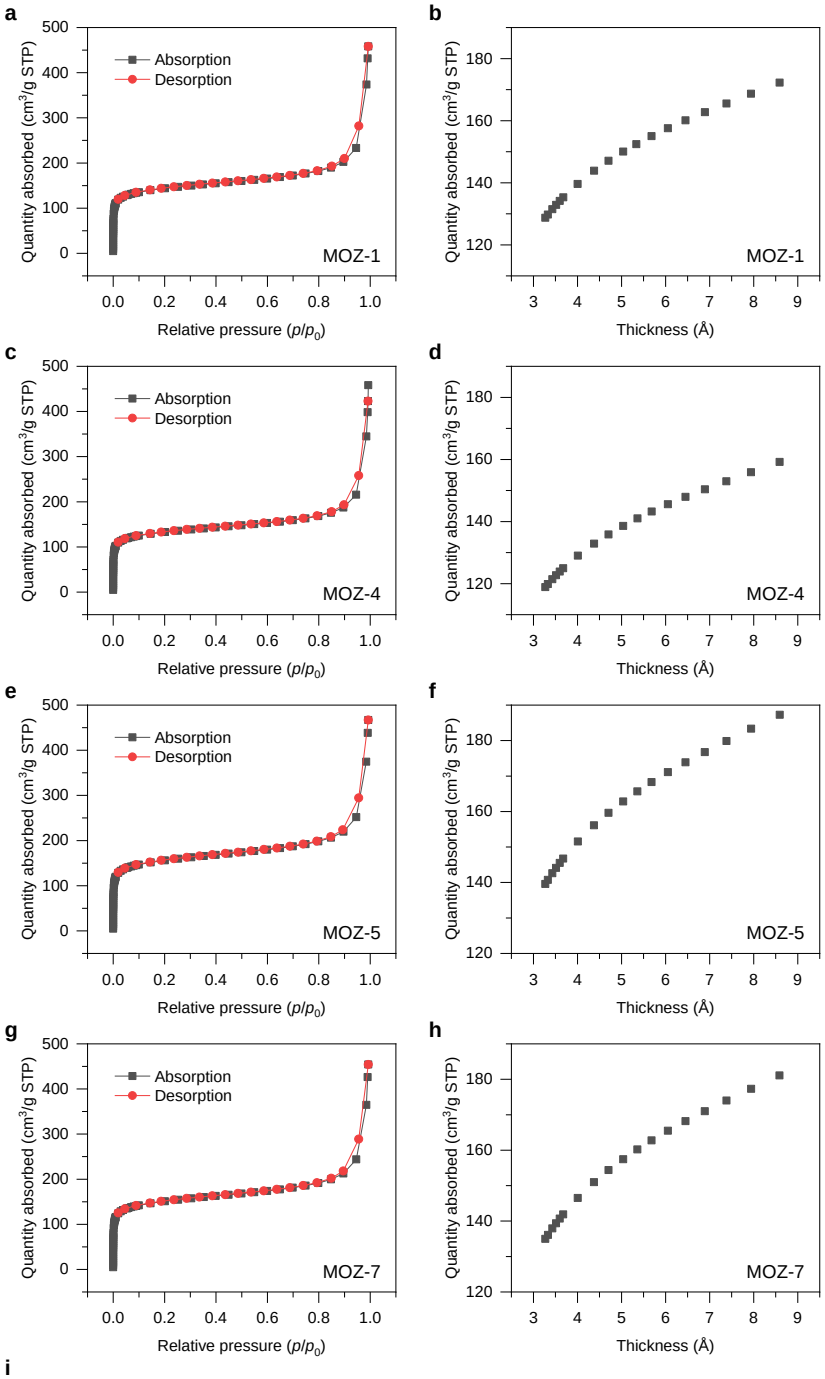

i

Parameters	MOZ-1	MOZ-4	MOZ-5	MOZ-7
Micropore volume (cm^3/g)	0.141	0.130	0.153	0.148
Micropore area (m^3/g)	329.8	304.3	356.74	344.7
External surface area (m^3/g)	185.7	171.8	202.8	196.2
Thickness range (Å)	3.5 to 5.0	3.5 to 5.0	3.5 to 5.0	3.5 to 5.0

Supplementary Fig. 7. N_2 sorption isotherms and t-plots. a-i, N_2 sorption isotherms and t-plot of (**a, b**) **MOZ-1**, (**c, d**) **MOZ-4**, (**e, f**) **MOZ-5**, and (**g, h**) **MOZ-7**, and (**i**) their result summary.

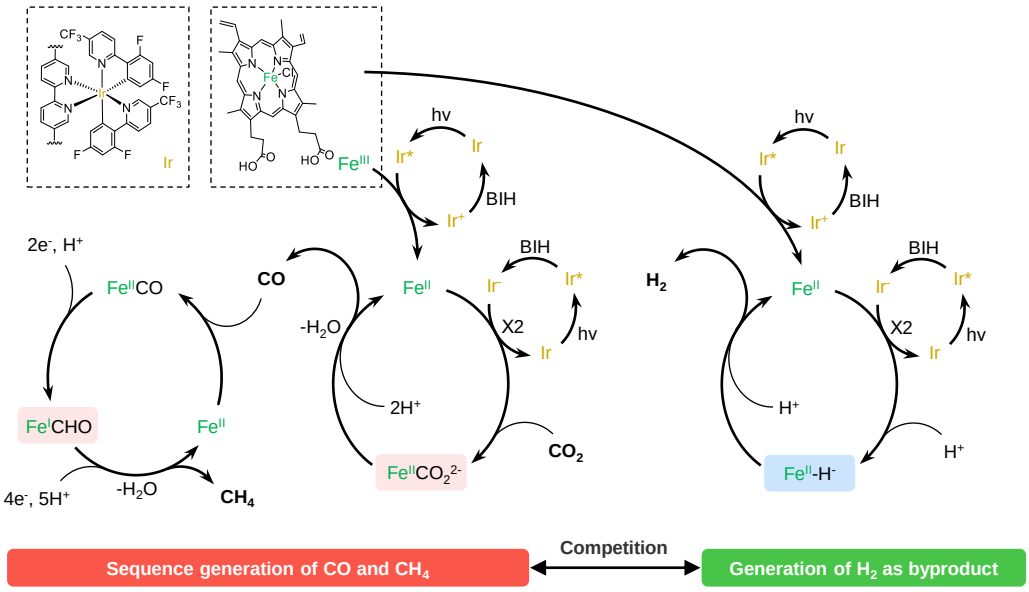

Supplementary Fig. 8. Proposed mechanism for MOZ-catalyzed CO_2RR. The proposed complete mechanism for photocatalytic CO_2-to-CH_4 conversation, with H_2 generation as the competing byproduct.

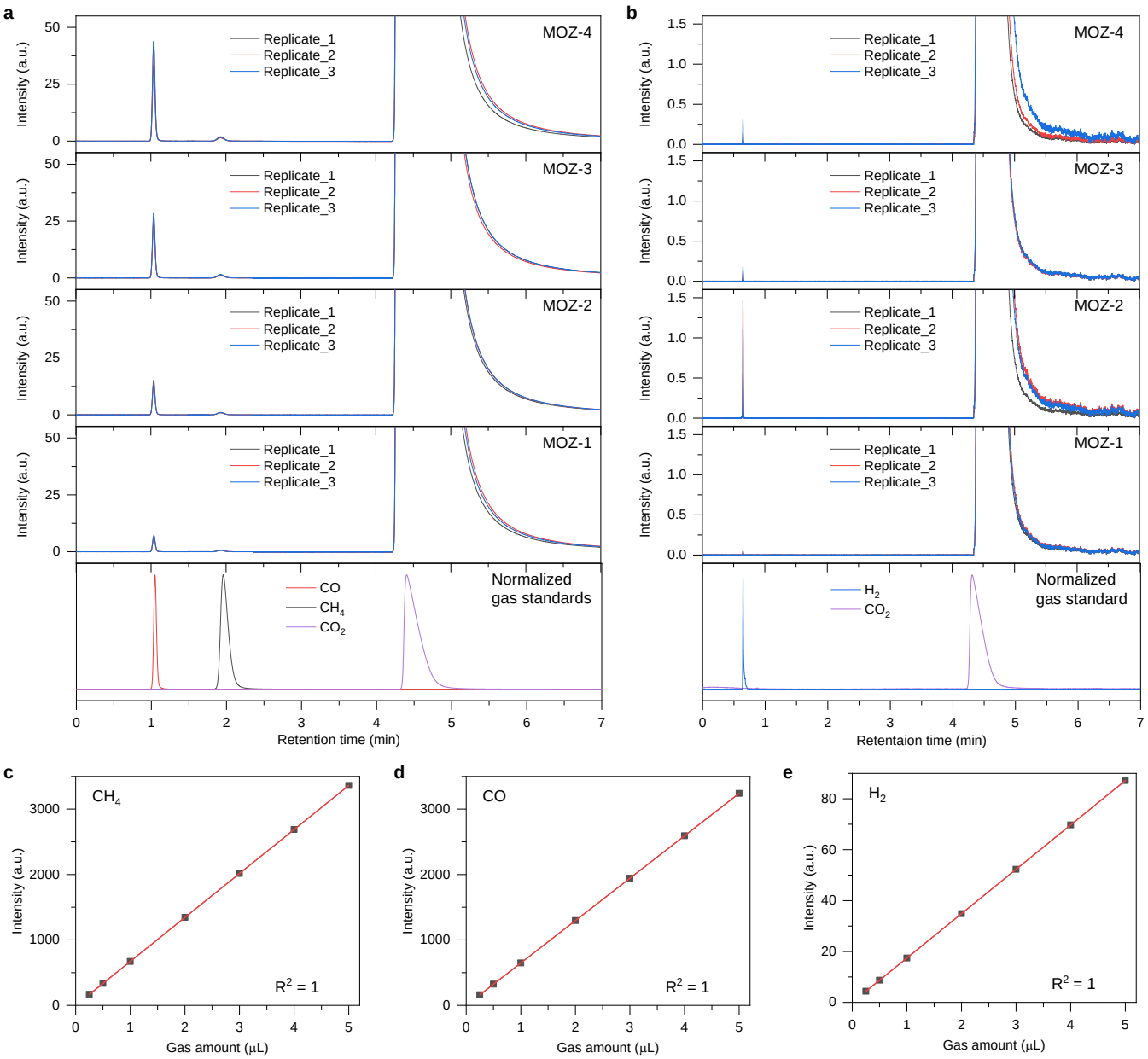

Supplementary Fig. 9. GC traces of MOZ-catalyzed CO_2RR. a-b, GC traces of MOZ-catalyzed CO_2RR in comparison to CH_4, CO, H_2, and CO_2 standards detected by (**a**) FID and (**b**) TCD. The scale of signal intensities in GC traces was adjusted to highlight the signals of CH_4, CO, and H_2. **c-e,** The calibration curves of (**c**) CH_4, (**d**) CO, and (**e**) H_2.

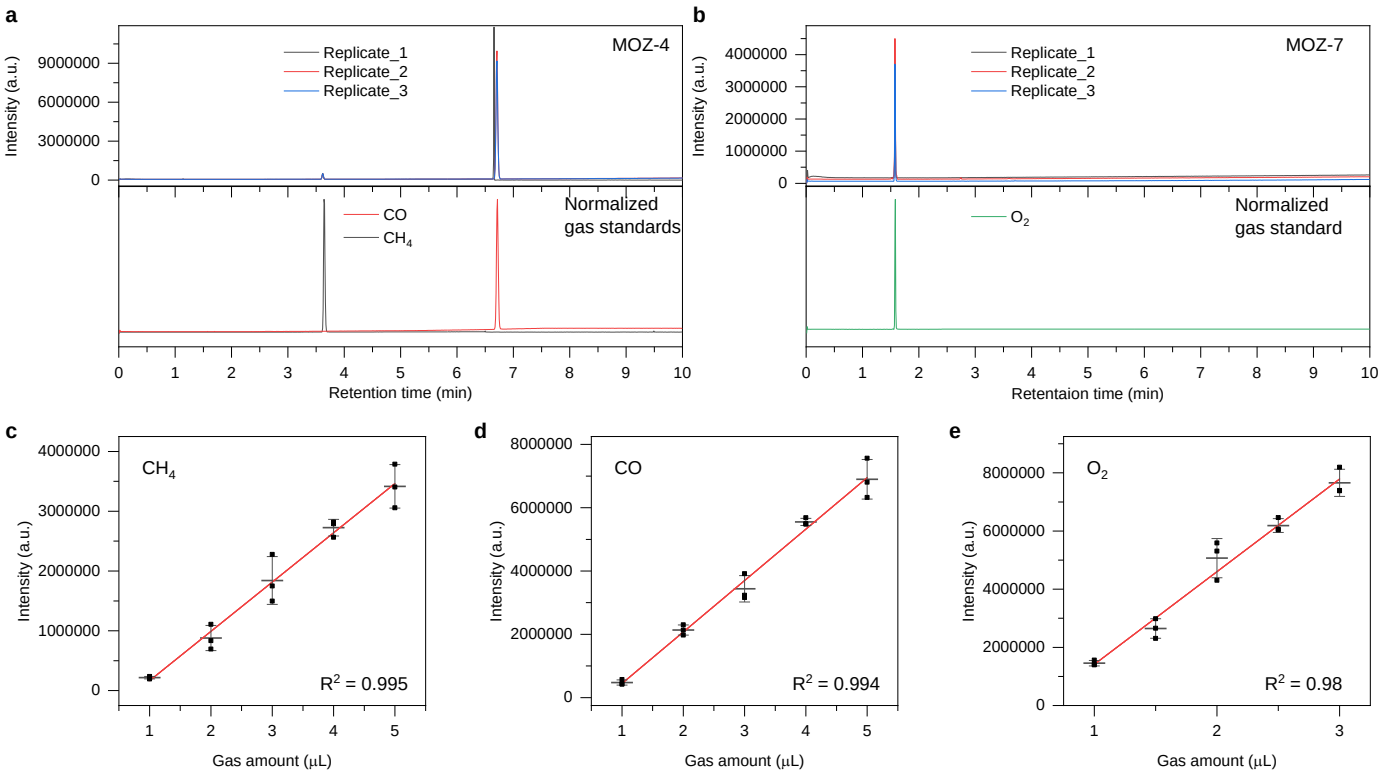

Supplementary Fig. 10. GC-MS traces. a, GC-MS traces of **MOZ-4** catalyzed CO_2RR in comparison to CH_4 and CO standards. **b,** GC-MS traces of **MOZ-7** catalyzed WOR in comparison to O_2 standard. **c-e,** The calibration curves of (**c**) CH_4, (**d**) CO, and (**e**) H_2 detected by GC-MS. In **c-e**, data are presented as mean ± s.d. (n= 3) with the central lines and error bars representing the mean and s.d., respectively; individual data points are shown as black dots.

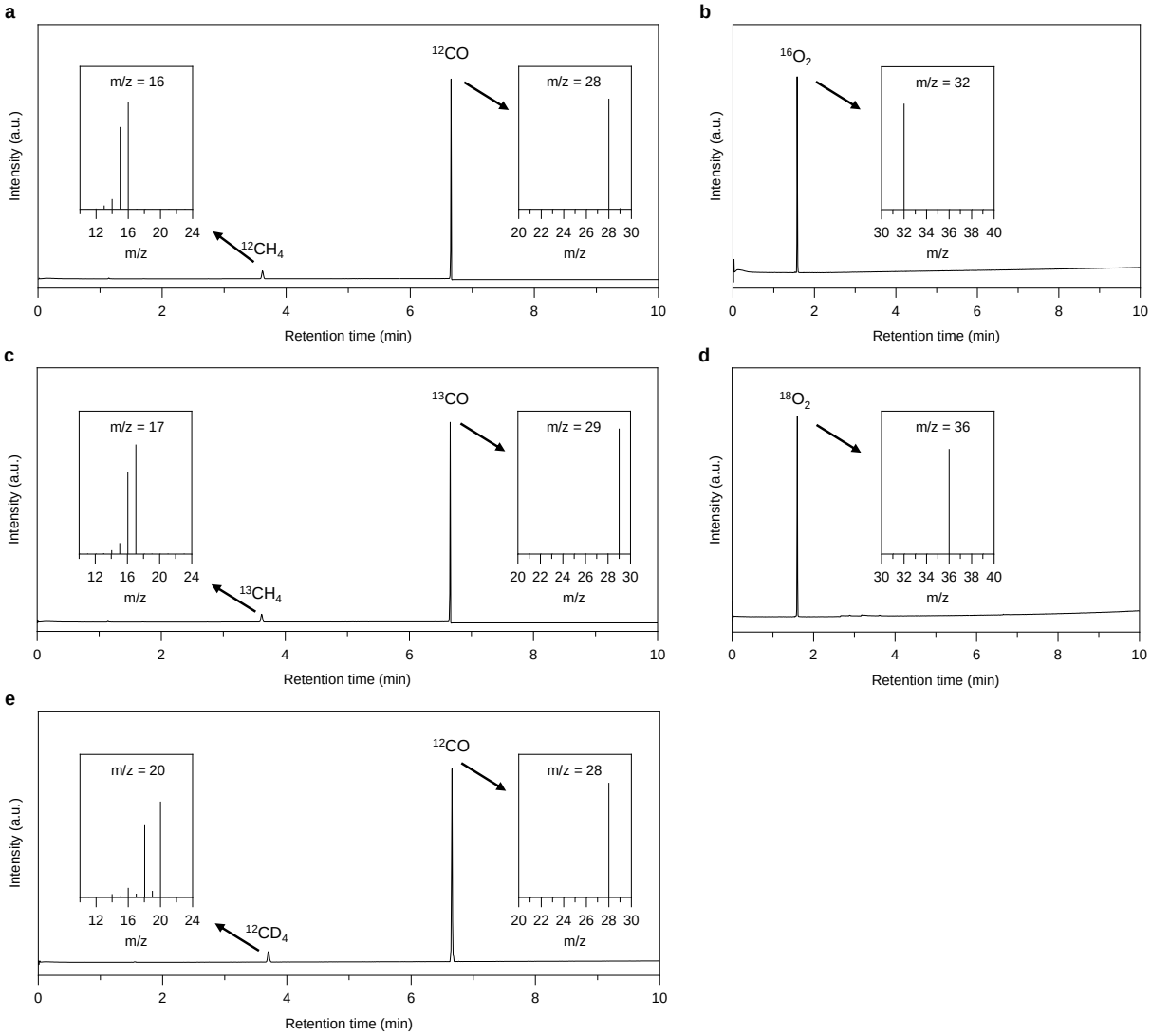

Supplementary Fig. 11. Isotope labeling. a-e, GC-MS traces and MS spectra (insert) of (**a**) **MOZ-4** catalyzed CO_2RR from normal $^{12}CO_2$ and CF_3CH_2OH, (**b**) **MOZ-7** catalyzed WOR from normal $H_2{}^{16}O$, (**c**) **MOZ-4** catalyzed CO_2RR from $^{13}CO_2$ and CF_3CH_2OH, (**d**) **MOZ-7** catalyzed WOR from normal $H_2{}^{18}O$, and (**e**) **MOZ-4** catalyzed CO_2RR from CO_2 and CF_3CD_2OD.

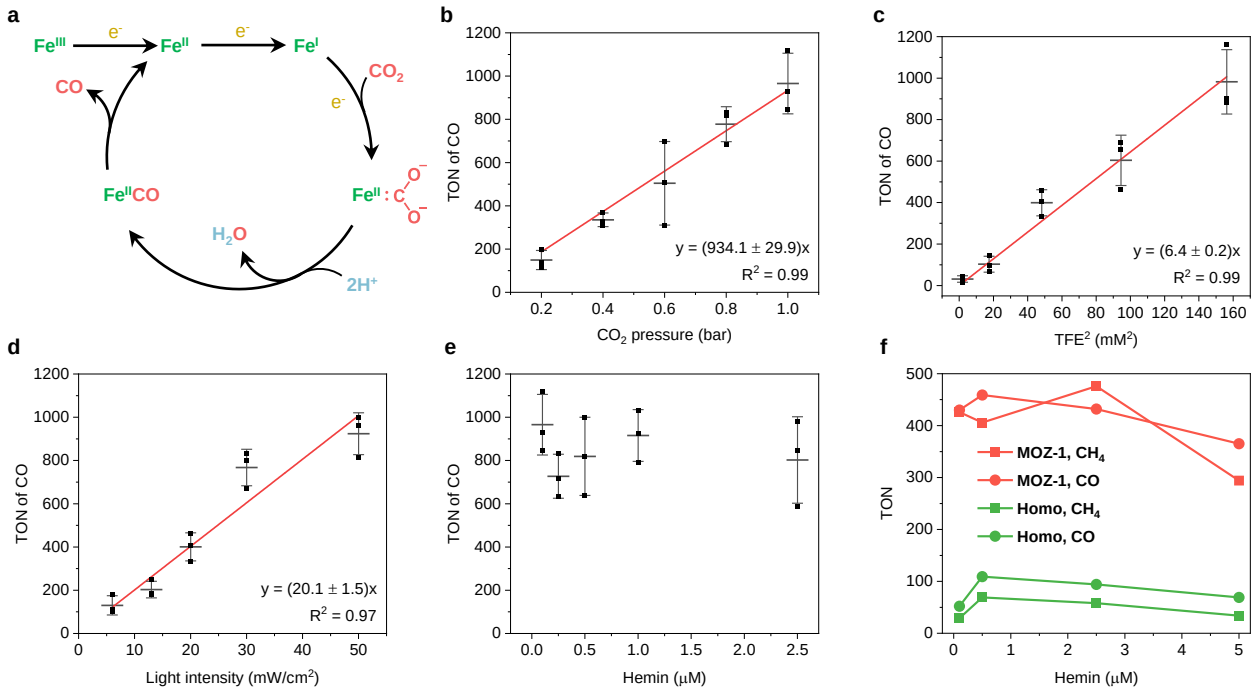

Supplementary Fig. 12. Kinetic Study of MOZ-catalyzed CO_2RR and homogeneous control reactions. a, Proposed mechanism of CO_2RR to CO by MOZs. Fe refers to the hemin catalyst, and the e^- is provided by photoexcited Ir-PS. **b-e,** Plots of the TON of CO for **MOZ-4** catalyzed CO_2RR versus (**b**) the pressure of CO_2, (**c**) the square of concentration of TFE, (**d**) the light intensity, and (**e**) the concentration of hemin. (**f**) Comparison between **MOZ-1** and its homologous analogue. Hemin concentrations of 0.1, 0.5, 2.5, and 5.0 μM corresponded to Ir-PS concentrations of 1.25, 6.25, 31.25, and 62.5 μM, respectively. Photocatalytic CO_2RR reactions were performed for 6 hours. In **b-e**, data are presented as mean ± s.d. (n= 3) with the central lines and error bars representing the mean and s.d., respectively; individual data points are shown as black dots.

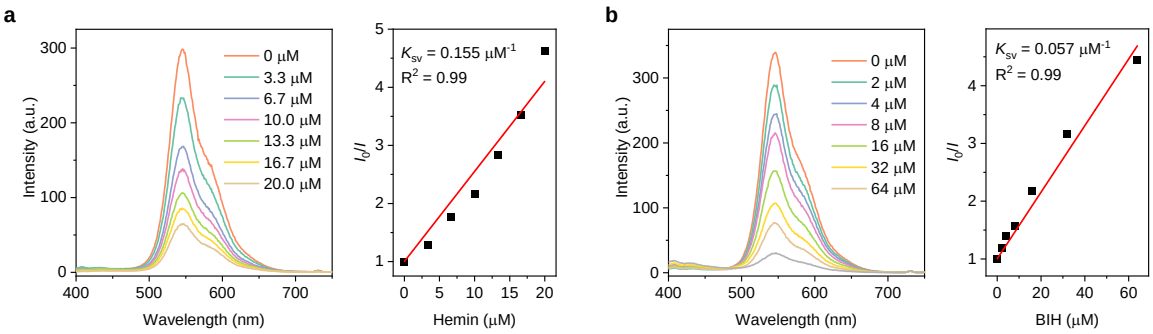

Supplementary Fig. 13. Luminescence quenching of Ir-PS by Hemin and BIH. a, Luminescence spectra upon excitation at 350 nm of 20 μM Ir-PS in DMF with varying concentrations of hemin (left) and their Stern-Volmer fitting (right, R^2 = 0.99 and K_{SV} = 0.155 μM^{-1}). **b,** Luminescence spectra upon excitation at 350 nm of 20 μM Ir-PS in DMF with varying concentrations of BIH (left) and their Stern-Volmer fitting (right, R^2 = 0.99 and K_{SV} = 0.057 μM^{-1}).

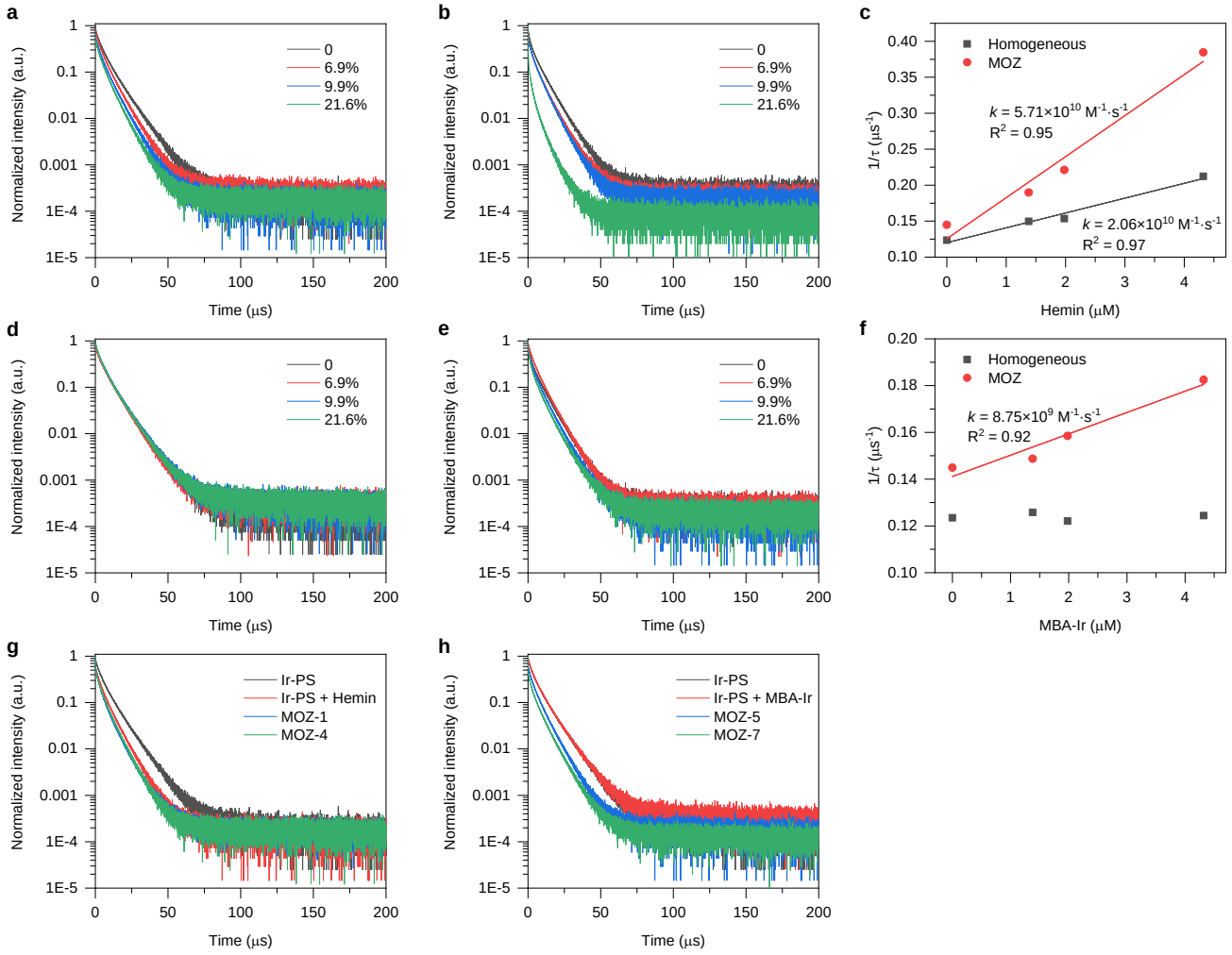

Supplementary Fig. 14. Time-resolved luminescence spectra. a-b, Normalized luminescence decay traces of (**a**) Ir-PS with different ratios of added Hemin and (**b**) **MOZ-1** with different Hemin loadings. **c,** Plots of $1/\tau$ as a function of the concentration of Hemin. **d-e,** Normalized luminescence decay traces of (**d**) Ir-PS with different ratios of added MBA-Ir and (**e**) **MOZ-5** with different MBA-Ir loadings. **f,** Plots of $1/\tau$ as a function of the concentration of MBA-Ir. The concentration of Ir-PS was 20 μM and the ratio/loading of Hemin/MBA-Ir to Ir-PS of 6.9%, 9.9%, and 21.6% corresponded to the Hemin/MBA-Ir concentration of 1.38 μM, 1.98 μM, and 4.32 μM, respectively. **g,** Normalized luminescence decay traces of Ir-PS (τ = 8.10 μs), Ir-PS with Hemin (τ = 6.51 μs), **MOZ-1** (τ = 4.52 μs), and **MOZ-4** (τ = 4.70 μs). **h,** Normalized luminescence decay traces of Ir-PS (τ = 8.10 μs), Ir-PS with MBA-Ir (τ = 8.19 μs), **MOZ-5** (τ = 6.31 μs), and **MOZ-4** (τ = 5.82 μs).

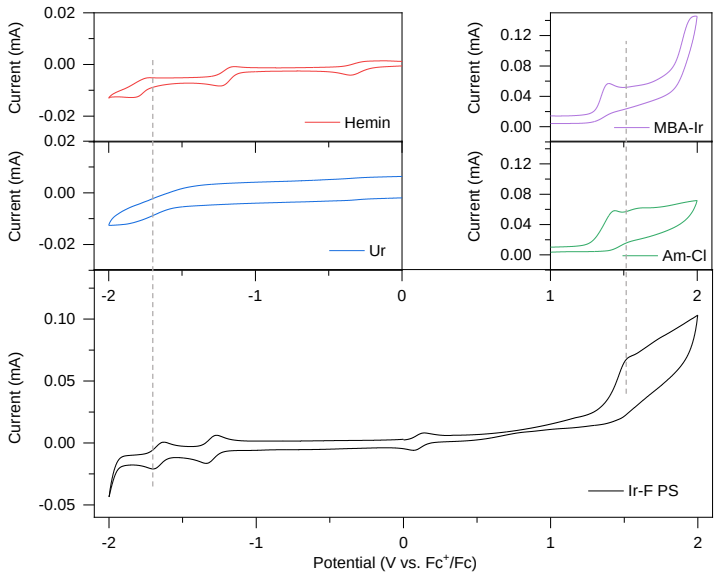

Supplementary Fig. 15. CV results. CVs of Ir-PS in comparison to Hemin, Ur, MBA-Ir, and Am-Cl. Fc^{+}/Fc couple was added as internal calibration standard. The reduction potentials of Ir-PS ([Ir-PS]/[Ir-PS]$^{-}$) were measured to be -1.70 V vs. Fc^{+}/Fc (-1.56 V vs. SCE) and -1.34 V vs. Fc^{+}/Fc (-1.18 V vs. SCE). Two reduction potentials of Ir-PS were observed because of two different ligands coordinated to the Ir in Ir-PS. The reduction potentials of Hemin were measured to be -0.35 V vs. Fc^{+}/Fc (Fe^{III}/Fe^{II}, -0.19 V vs. SCE), -1.22 V vs. Fc^{+}/Fc (Fe^{II}/Fe^{I}, -1.06 V vs. SCE), and -1.80 V vs. Fc^{+}/Fc (Fe^{I}/Fe^{0}, -1.64 V vs. SCE), respectively. The oxidation potentials of Ir-PS, Am-Cl, and MBA-Ir were measured to be 1.51 V vs. Fc^{+}/Fc ($[Ir\text{-}PS]^{+}/[Ir\text{-}PS]$), 1.67 V vs. SCE), 1.43 V vs. Fc^{+}/Fc ($[Am\text{-}Cl]^{+}/[Am\text{-}Cl]$, 1.59 V vs. SCE), and 1.39 V vs. Fc^{+}/Fc ($[MBA\text{-}Ir]^{+}/[MBA\text{-}Ir]$), 1.55 V vs. SCE), respectively.

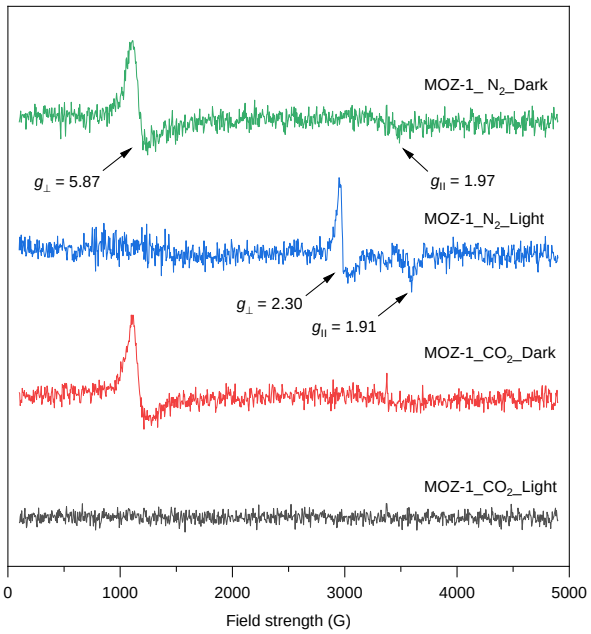

Supplementary Fig. 16. EPR spectra. **MOZ-1** with high Hemin loading (Ir-PS of 10 mM and Hemin of 3 mM, 30% Hemin loading) was dispersed in 2 mL of DMA with 22.4 mg BIH (sacrificial reductant). The mixture was divided into four groups in equal volume followed by purging with N_2 without light irradiation (**MOZ-1**_N_2_Dark), purging with N_2 and illuminating by Xe lamp for 20 mins (**MOZ-1**_N_2_Light), purging with CO_2 (**MOZ-1**_CO_2_Dark) or purging with CO_2 and illuminating by Xe lamp for 20 mins (**MOZ-1**_CO_2_Light). EPR signals with $g_\perp$ of 5.87 and $g_\parallel$ of 1.97 correspond to Hemin(Fe^{III}),[89] while EPR signals with $g_\perp$ of 2.30 and $g_\parallel$ of 1.91 correspond to Hemin(Fe^{I}).[90,91]

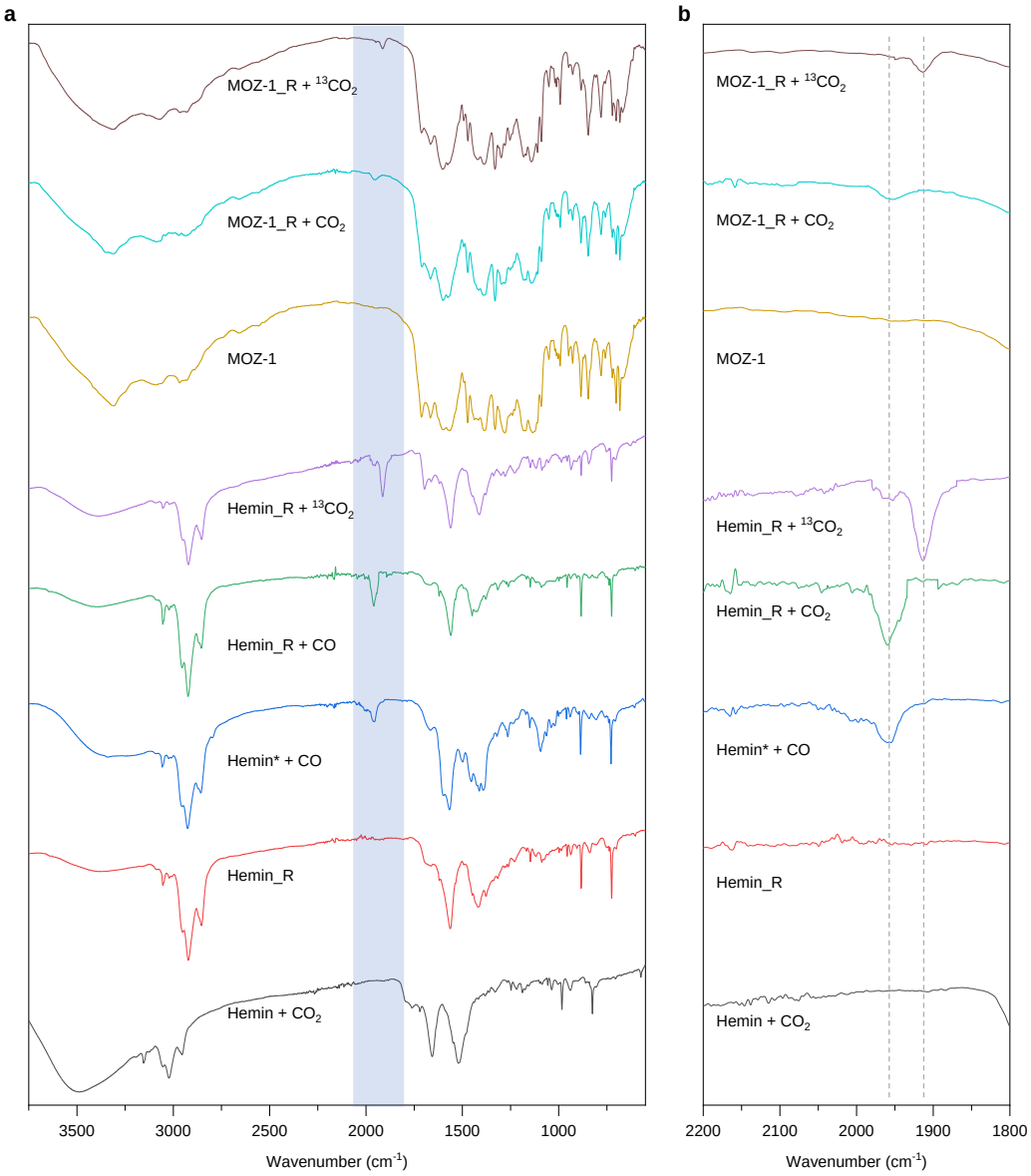

Supplementary Fig. 17. FTIR spectra to probe the intermediate of MOZ-catalyzed CO_2RR. a-b, FTIR spectra of reduced hemin and **MOZ-1** reacting with CO_2 (or $^{13}CO_2$) and their corresponding controls in the ranges of (**a**) 3750-550 cm^{-1} and (**b**) 2200-1800 cm^{-1}. The hemin loading in the **MOZ-1** for FTIR was increased to 100% (1:1 ratio of Hemin to Ir-PS). Two dashed lines in Supplementary Fig. 17b refer to the absorption of Hemin(Fe^{II})-bound ^{12}CO at 1956 cm^{-1} and Hemin(Fe^{II})-bound ^{13}CO at 1910 cm^{-1}, respectively.

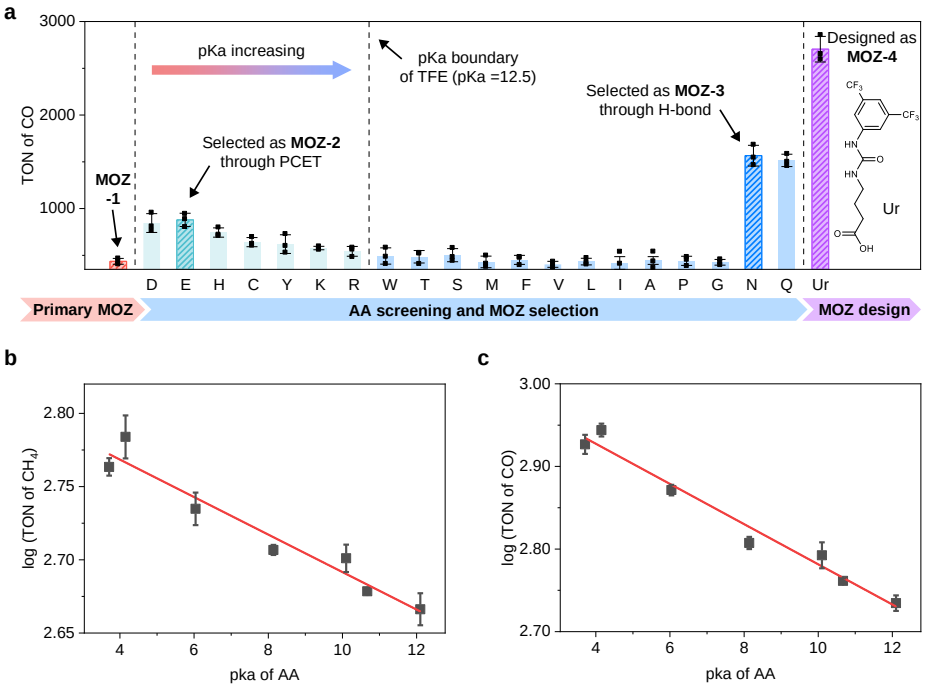

Supplementary Fig. 18. AA screening for CO_2RR. a, Turnover numbers (TON) of CO for **MOZ-1**, AA modified MOZ-1, and Ur modified **MOZ-1**. Glu and Asn modified **MOZ-1** were selected (**MOZ-2** and **MOZ-3**, respectively,) due to their enhanced activity. Ur modified **MOZ-1** was denoted **MOZ-4**. Data are presented as mean ± s.d. (n= 3) with the error bars representing the s.d.; individual data points are shown as black dots. **b-c,** (**b**) log(TON of CH_4) and (**c**) log(TON of CO) both showed negative correlation with pKa values of modified AA with Pearson correlation coefficients of -0.97 and -0.99, respectively. In **b-c**, data are presented as mean ± s.d. (n= 3) with the error bars representing the s.d.

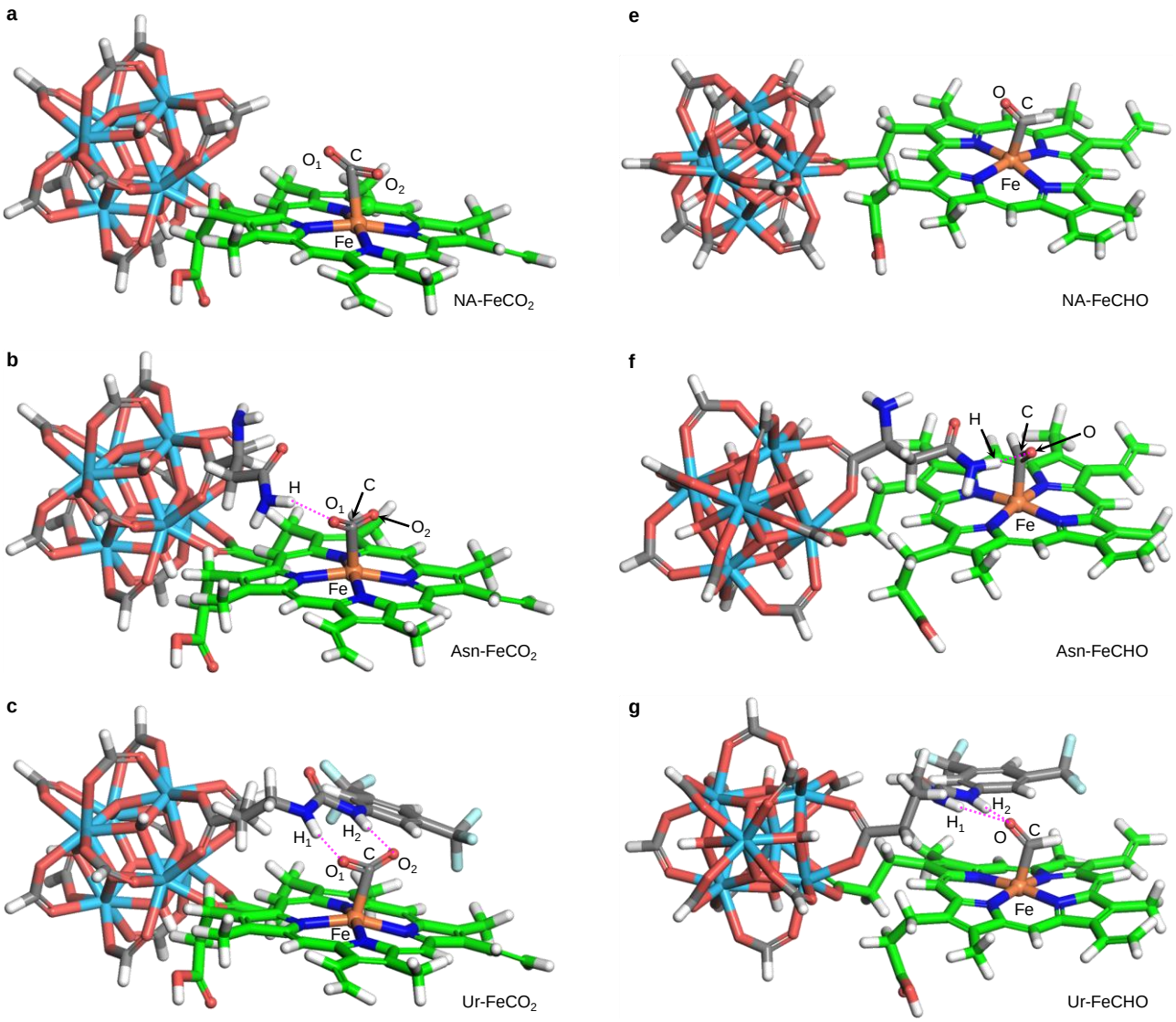

d

Parameters	NA-$FeCO_2$	Asn-$FeCO_2$	Ur-$FeCO_2$
d_{Fe-C} (Å)	2.19	2.10	2.04
d_{C-O} (Å)	1.21 ($C-O_1$) 1.23 ($C-O_2$)	1.22 ($C-O_1$) 1.23 ($C-O_2$)	1.24 ($C-O_1$) 1.23 ($C-O_2$)
$\angle O_1-C-O_2$ (°)	150.0	145.9	136.2
$d_{H\text{-}bond}$ (Å)	-	1.96 ($H\cdots O_1$)	1.91 ($H_1\cdots O_1$) 1.85 ($H_2\cdots O_2$)
NPA Charge (CO_2)	-0.29	-0.38	-0.56
ΔH_{stb} (kcal·mol^{-1})	0	-14.1	-23.5

h

Parameters	NA-FeCHO	Asn-FeCHO	Ur-FeCHO
d_{Fe-C} (Å)	2.02	1.88	1.86
d_{C-O} (Å)	1.20	1.21	1.22
$d_{H\text{-}bond}$ (Å)	-	2.02 ($H\cdots O$)	2.23 ($H_1\cdots O$) 1.88 ($H_2\cdots O$)
NPA Charge (CO_2)	-0.31	-0.36	-0.43
ΔH_{stb} (kcal·mol^{-1})	0	-9.1	-17.2

Supplementary Fig. 19. Optimized structures by DFT calculations. a-c, Optimized structures of (**a**) NA-$FeCO_2$ (as control group), (**b**) Asn-$FeCO_2$ (in **MOZ-3**), and (**c**) Ur-$FeCO_2$ (in **MOZ-4**) with the key atoms

labeled. **d,** Summary of the geometries of the bound CO_2 in the above optimized structures. **e-g,** Optimized structures of (**e**) NA-FeCHO (as control group), (**f**) Asn-FeCHO (in **MOZ-3**), and (**g**) Ur-FeCHO (in **MOZ-4**) with the key atoms labeled. **h,** Summary of the geometries of the bound CHO in the above optimized structures.

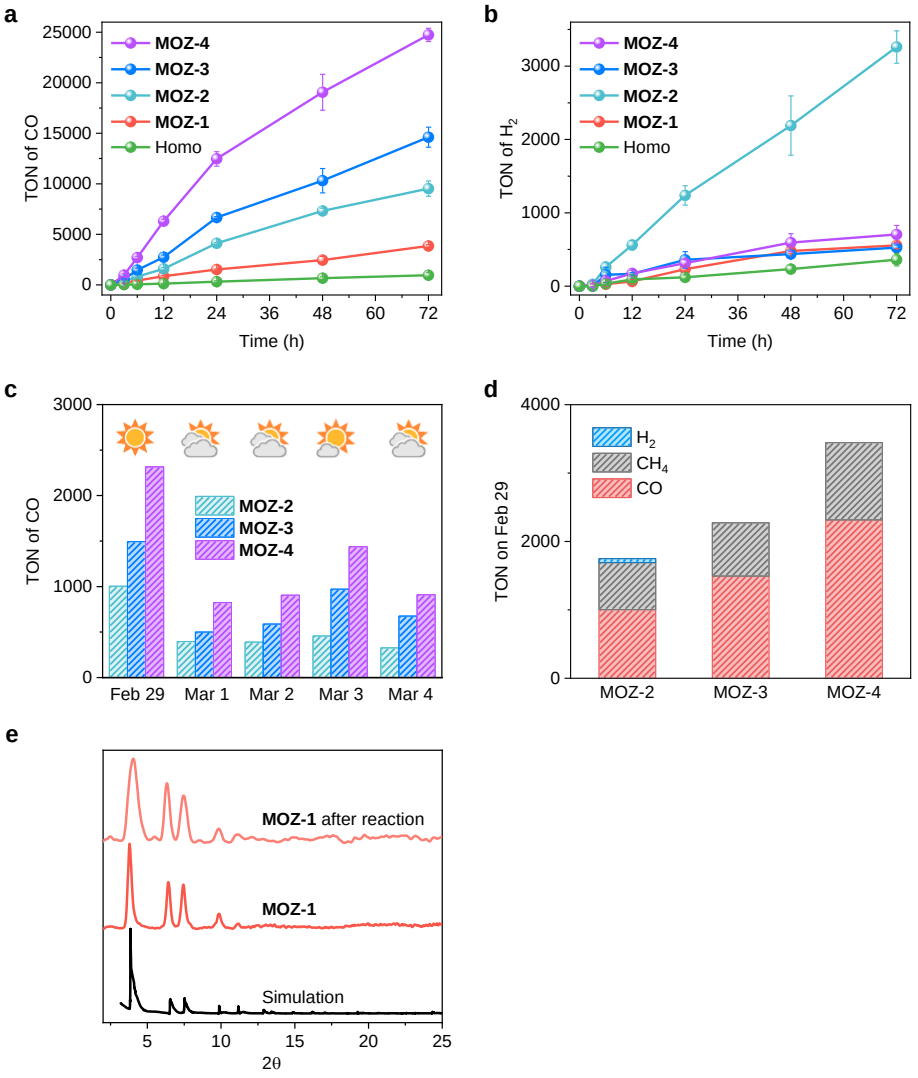

Supplementary Fig. 20. Photocatalytic CO_2RR. a-b, Time-dependent TONs of (**a**) CO and (**b**) H_2 for **MOZ-1**, **MOZ-2**, **MOZ-3**, **MOZ-4**, and homogeneous control (Homo, mixture of Ir-PS and hemin) under xenon lamp irradiation. In **a-b**, data are presented as mean ± s.d. (n= 3) with the error bars representing the s.d. **c,** TONs of CO for **MOZ-2**, **MOZ-3**, or **MOZ-4** over five consecutive days (Feb 29 to Mar 4, 2020) under direct sunlight. **d,** TON of CO, CH_4, and H_2 for **MOZ-2**, **MOZ-3**, and **MOZ-4** under direct sunlight on Feb 29, 2020. **e,** PXRD pattern of **MOZ-1**; after 72 h under reaction condition, this pattern remained similar to those of simulated and freshly prepared **MOZ-1**, demonstrating stability of MOZs during photocatalytic reactions.

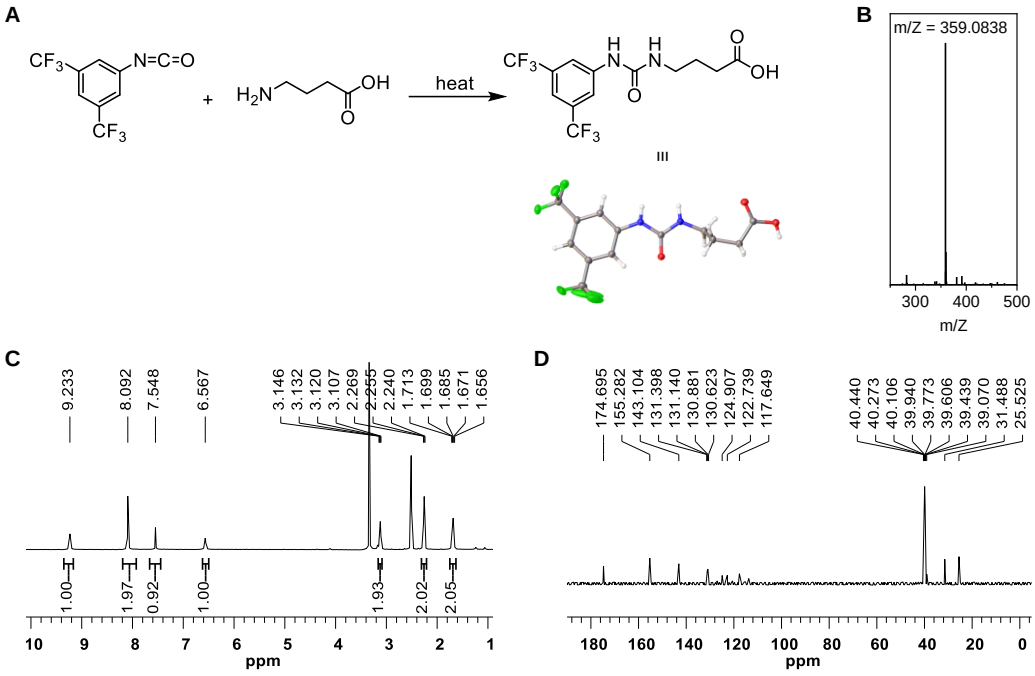

Supplementary Fig. 21. Synthesis of Ur ligand. a, Synthesis of Ur ligand and its corresponding crystal structure. See Supplementary Table 4 and Supplementary Data 2 for the crystallographic information of Ur ligand. **b-d,** (**b**) High-resolution mass spectrum, (**c**) ^{1}H NMR spectrum, and (**d**) ^{13}C NMR spectrum of Ur ligand.

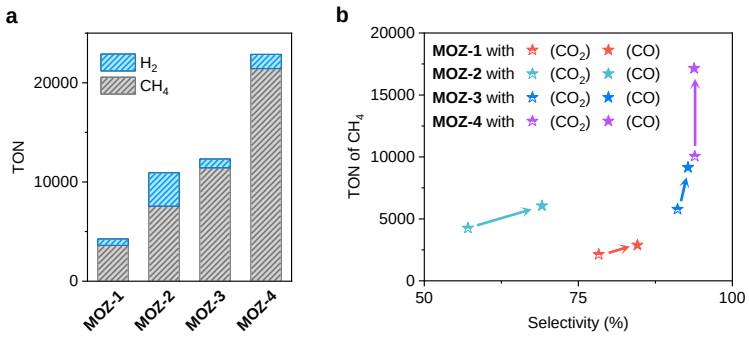

Supplementary Fig. 22. MOZ-catalyzed CO reduction. a, TON of CH_4 and H_2 with CO/N_2 (1:9) atmosphere for **MOZ-1**, **MOZ-2**, **MOZ**-3 or **MOZ-4** under 72 h visible-light irradiation. **b,** Reaction summary (TON and selectivity) of CH_4 generation with both CO_2 and CO/N_2 (1:9) atmospheres, under 72 h visible-light irradiation.

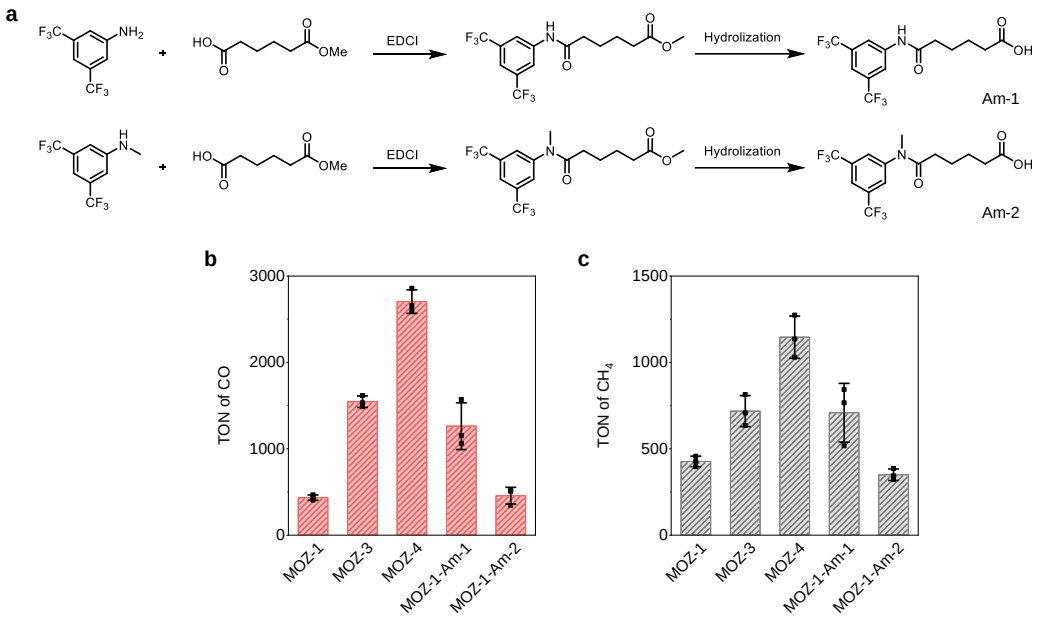

Supplementary Fig. 23. Amide ligands for CO_2RR. a, Synthesis of Am-1 and Am-2 ligands. **b-c,** TONs of (**b**) CO and (**c**) CH_4 for **MOZ-1**, **MOZ-4**, **MOZ-1**-Am-1, and **MOZ-1**-Am-2 under 6-hour reaction. In **b-c**, data are presented as mean ± s.d. (n= 3) with the error bars representing the s.d.; individual data points are shown as black dots.

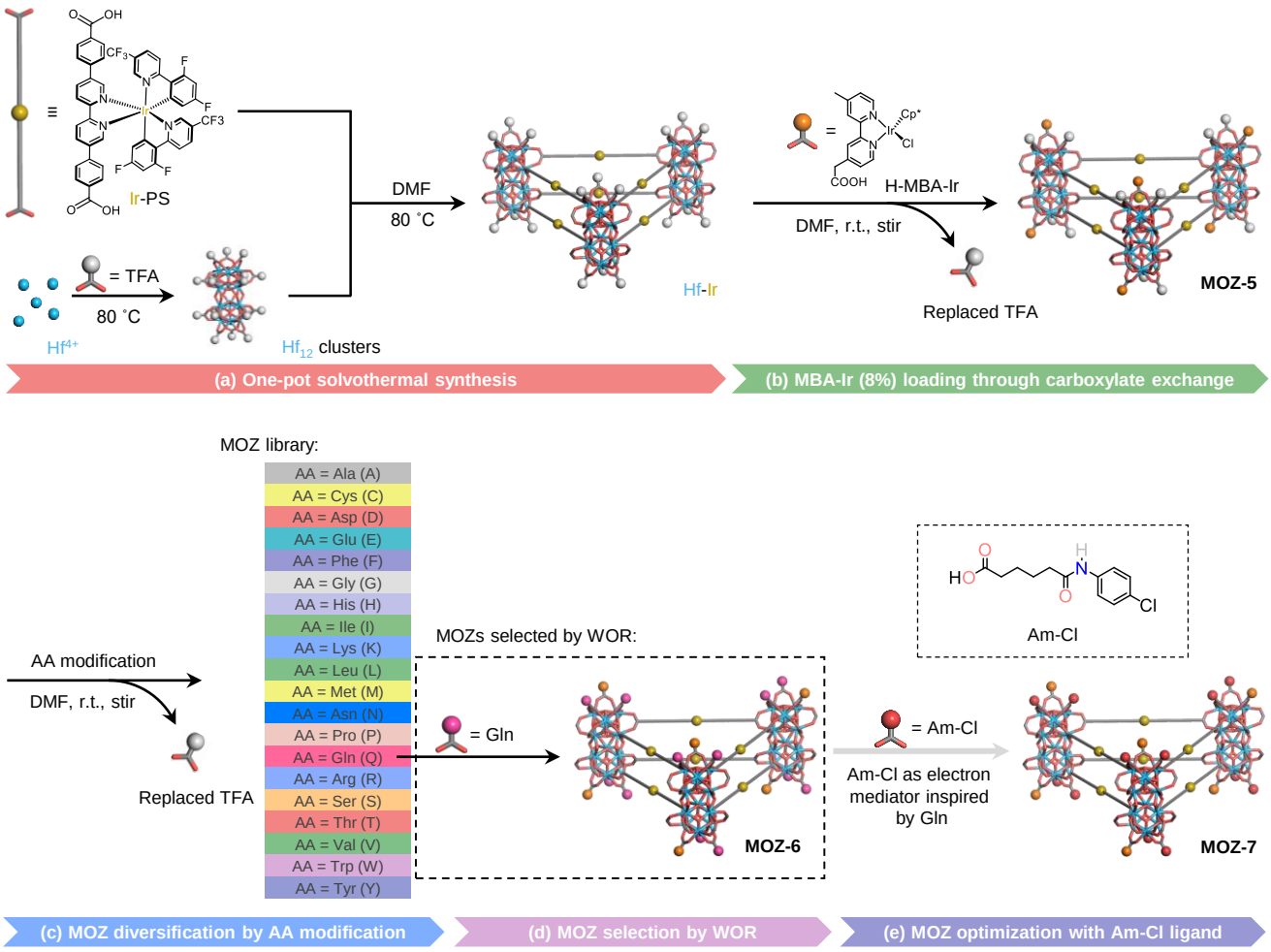

Supplementary Fig. 24. MOZ construction and optimization for WOR. (a) Hf-Ir monolayer was synthesized through a one-pot solvothermal synthesis to interlink Hf_{12} SBUs with Ir-PS. (b) **MOZ-5** was synthesized through post-synthetic modification of Hf-Ir monolayer with H-MBA-Ir, wherein weakly-coordinating TFA is replaced through carboxylate exchange. (c) The library of MOZs was generated by separately appending 20 AAs on **MOZ-5**, whereby all remaining TFA was exchanged to generate 20 MOZ candidates with unique active sites. (d) Gln-modified **MOZ-5** showed enhanced activity for photocatalytic WOR, which was selected as **MOZ-6**. (e) Inspired by **MOZ-6**, a series of Am-R ligands (R = OCH_3, CH_3, H, F, Cl, Br, or NO_2) with precisely controlled oxidation potentials (of the amide groups) was synthesized and the optimized **MOZ-7** with Am-Cl was subsequently revealed to possess the highest activity for photocatalytic WOR.

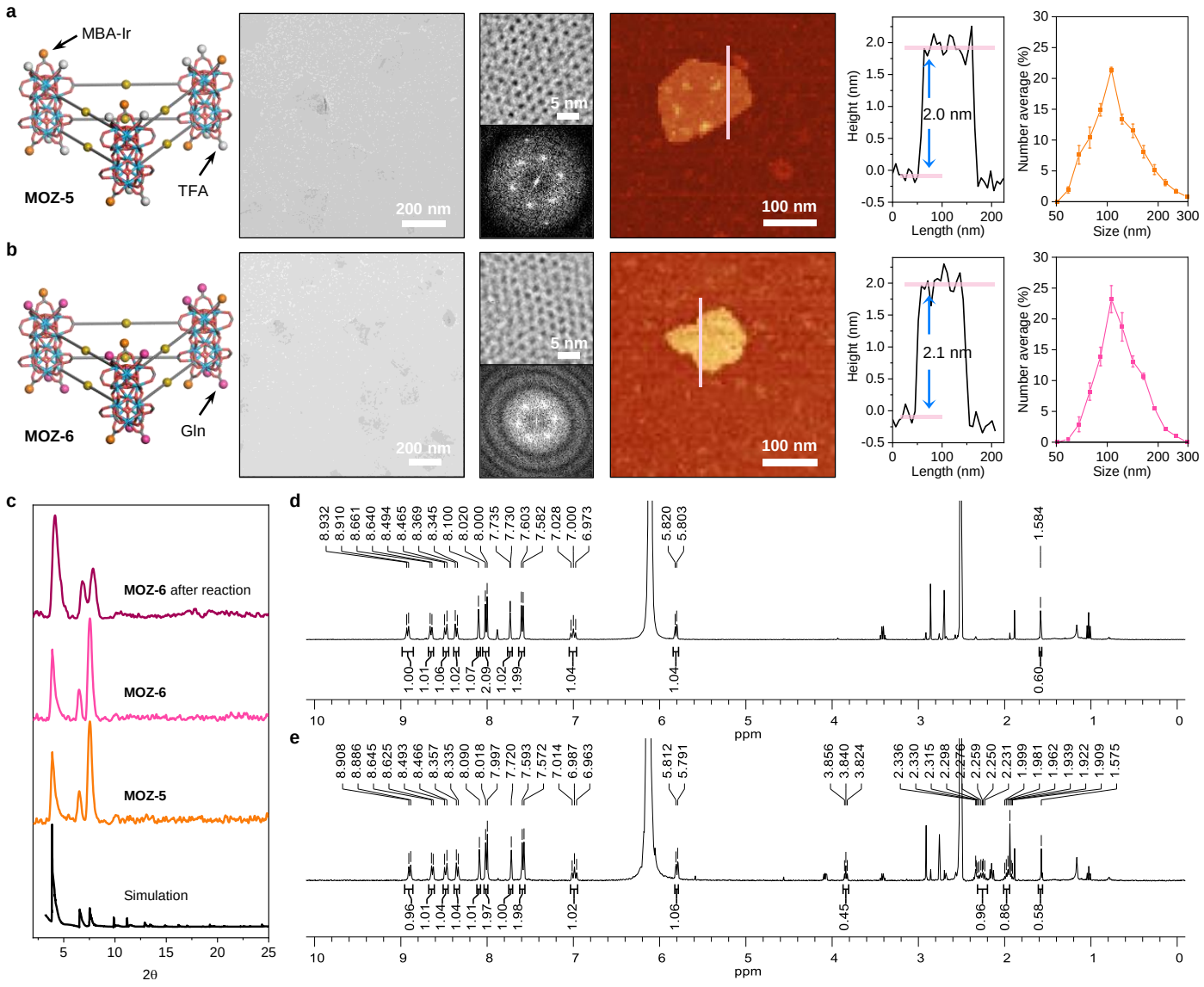

Supplementary Fig. 25. Characterization of MOZ-5 and MOZ-6. a, b, Morphological characterization of (**a**) **MOZ-5** and (**b**) **MOZ-6**. For each, from left to right: modeled structure, TEM imaging, HRTEM imaging (top) and its FFT pattern (bottom), AFM topography, height profile, and number-averaged diameter as measured by DLS. Number-averaged diameters were measured to be 117.4 ± 8.1 nm and 120.6 ± 4.1 nm for **MOZ-5** and **MOZ-6**, respectively. In **a-b**, DLS data are presented as mean ± s.d. (n= 3) with the error bars representing the s.d. **c,** PXRD patterns of MOZs, freshly prepared or after reaction, compared to the simulated pattern based on the monolayered MOF structure. **d,** NMR spectra of digested **MOZ-5**. A 0.6:1 NMR signal ratio of Cp* (1.564 ppm, 15H) in MBA-Ir to Ir-PS was observed, corresponding to a 0.08 to 1 molar ratio of MBA-Ir to Ir-PS. **e,**

NMR spectra of digested **MOZ-6**. A ~0.45:1 NMR signal ratio of Gln (3.840 ppm, 1H; 2.228 ppm, 2H; 1.950 ppm, 2H) to Ir-PS was observed, corresponding to a ~0.9:1 molar ratio of Gln to Ir-PS

.

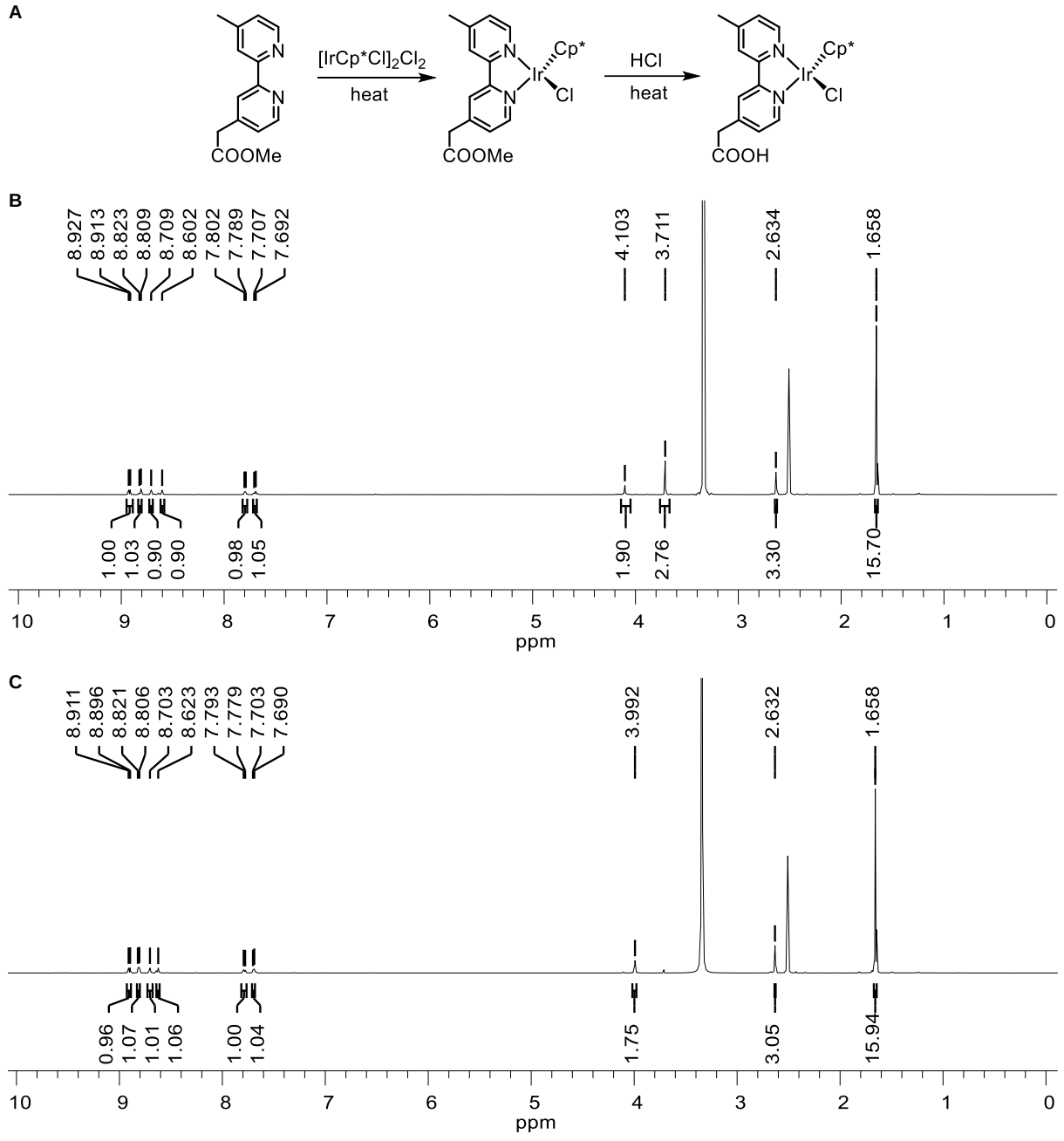

Supplementary Fig. 26. Synthesis of H-MBA-Ir. a, Synthesis route of H-MBA-Ir. **b, c,** ^{1}H NMR spectrum of (**b**) Me-MBA-Ir and (**c**) H-MBA-Ir.

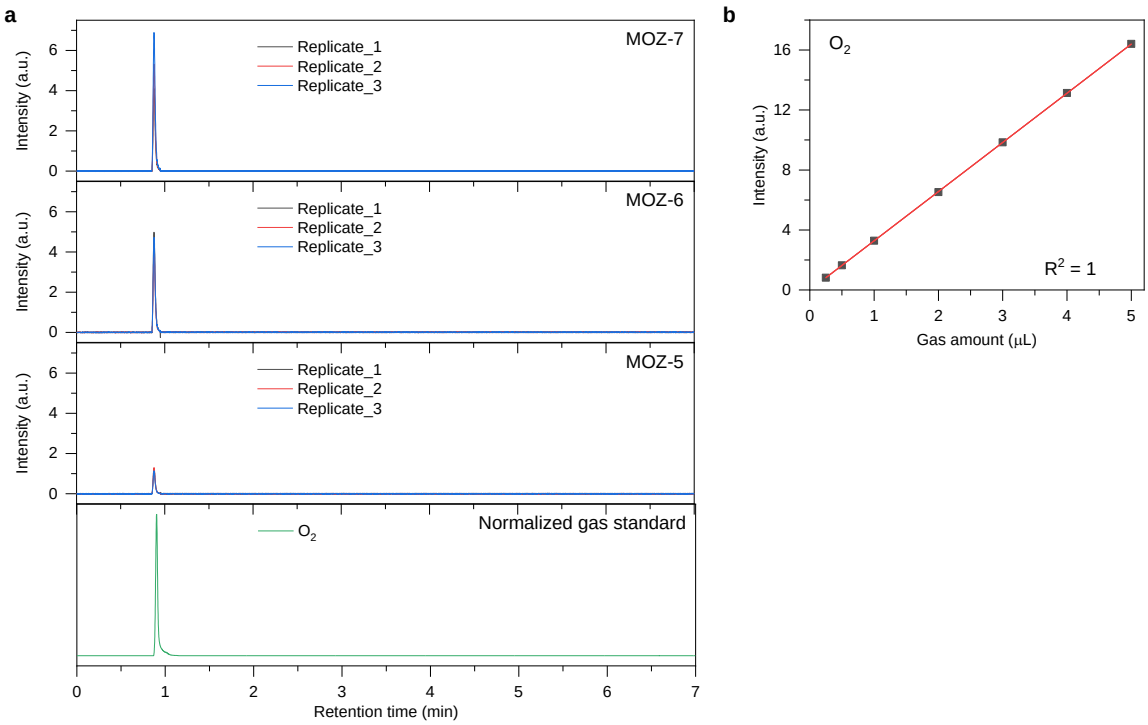

Supplementary Fig. 27. GC traces of MOZ-catalyzed WOR. a, GC traces of MOZ-catalyzed WOR in comparison to O_2 standard detected by FID. **b,** The calibration curve of O_2 by FID detection.

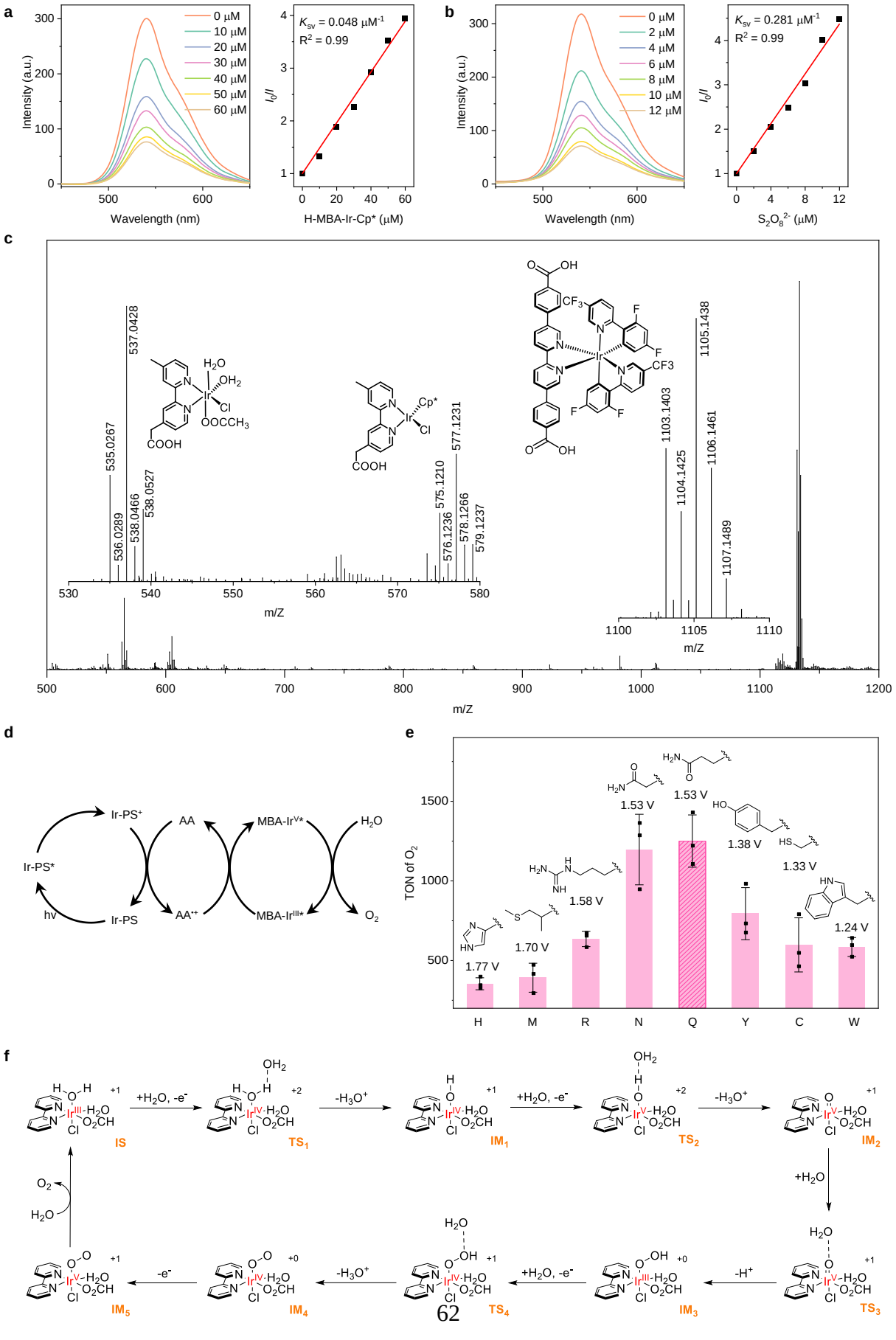
a
Intensity (a.u.)
Wavelength (nm)
0 μM
10 μM
20 μM
30 μM
40 μM
50 μM
60 μM
K_{sv} = 0.048 μM^{-1}
R^2 = 0.99
I_0/I
H-MBA-Ir-Cp* (μM)
b
Intensity (a.u.)
Wavelength (nm)
0 μM
2 μM
4 μM
6 μM
8 μM
10 μM
12 μM
K_{sv} = 0.281 μM^{-1}
R^2 = 0.99
I_0/I
$S_2O_8^{2-}$ (μM)
c
537.0428
535.0267
536.0289
538.0466
538.0527
575.1210
576.1236
577.1231
578.1266
579.1237
1103.1403
1104.1425
1105.1438
1106.1461
1107.1489
m/Z
d
Ir-PS*
Ir-PS$^+$
AA
AA$^{+\bullet}$
MBA-Ir^{V*}
MBA-Ir^{III*}
H_2O
O_2
hv
Ir-PS
e
TON of O_2
1.77 V
1.70 V
1.58 V
1.53 V
1.53 V
1.38 V
1.33 V
1.24 V
H
M
R
N
Q
Y
C
W
f
IS
TS_1
IM_1
TS_2
IM_2
TS_3
IM_3
TS_4
IM_4
IM_5
+H_2O, -e^-
-H_3O^+
+H_2O, -e^-
-H_3O^+
+H_2O
-H^+
+H_2O, -e^-
-H_3O^+
-e^-
O_2
H_2O

Supplementary Fig. 28. Mechanistic analysis of MOZ-catalyzed WOR. a, Luminescence spectra upon excitation at 350 nm of 20 μM Ir-PS in DMF with varying concentrations of Me-MBA-Ir (left) and their Stern-Volmer fitting (right, R^2 = 0.99 and K_{SV} = 0.048 μM^{-1}). **b,** Luminescence spectra upon excitation at 350 nm of 20 μM Ir-PS in DMF with varying concentrations of $K_2S_2O_8$ (left) and their Stern-Volmer fitting (right, R^2 = 0.99 and K_{SV} = 0.281 μM^{-1}). **c,** HR-MS spectra of digested **MOZ-5** after 6-h reaction under photocatalytic WOR condition. The signals with m/Z of 1105.1438, 575.1231, and 537.0428 correspond to Ir-PS ($[M]^+$: 1105.144), H-MBA-Ir ($[M]^+$: 575.125), and H-MBA-Ir* ([M]+: 537.042), respectively. **d,** Proposed mechanism for photocatalytic WOR catalyzed by **MOZ-5** and **MOZ-6**. **e,** TON for O_2 of AA-modified **MOZ-5** with redox-active residues after 6-h reaction under photocatalytic WOR condition. Data are presented as mean ± s.d. (n= 3) with the error bars representing the s.d.; individual data points are shown as black dots. The chemical structures and redox potential of the corresponding $AA^{\bullet+}$/AA were labeled in the figures. Redox potentials for R-groups were obtained from previously report.[92,93] **f,** Proposed mechanism for WOR catalyzed by **MOZ-5** or homogeneous control (a mixture of Ir-PS and Me-MBA-Ir). IS, initial state; TS, transitional state; IM, intermediate; FS, final state.

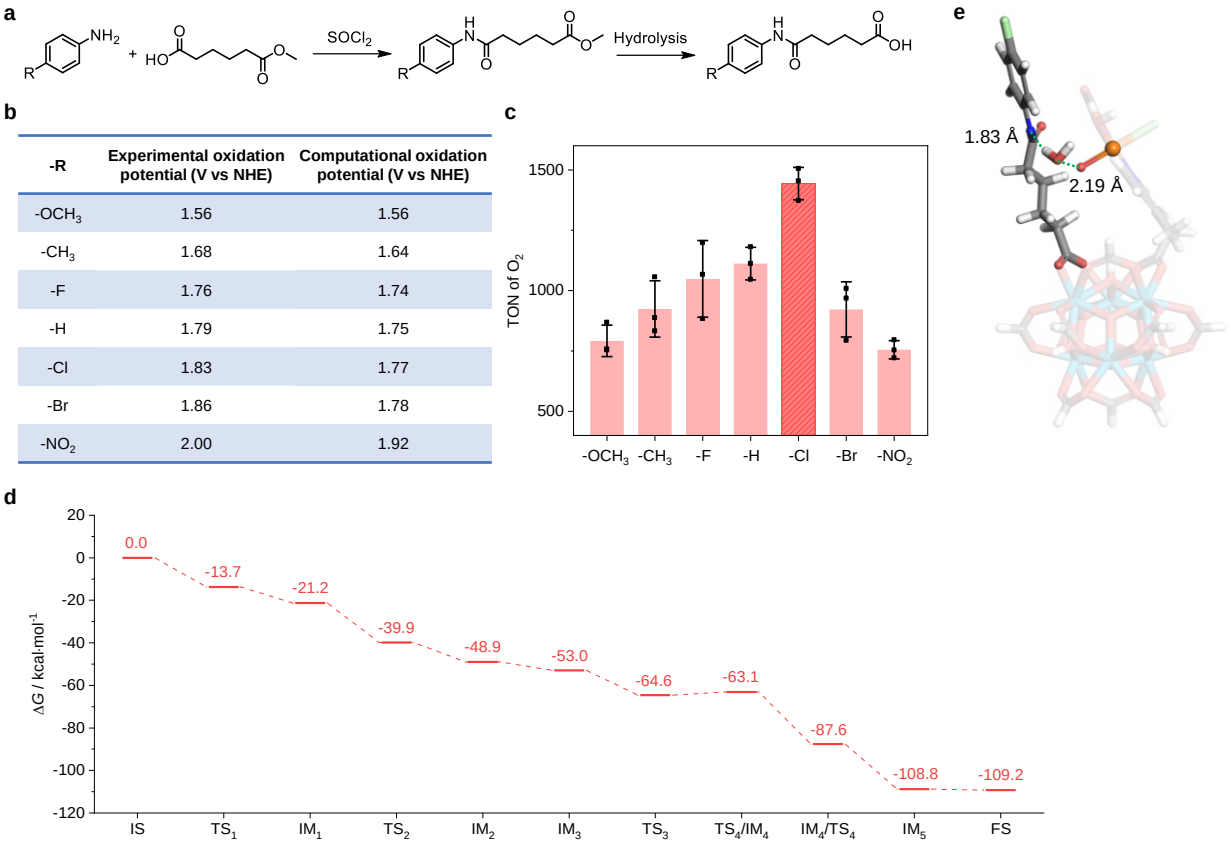

-R	Experimental oxidation potential (V vs NHE)	Computational oxidation potential (V vs NHE)
$-OCH_3$	1.56	1.56
$-CH_3$	1.68	1.64
-F	1.76	1.74
-H	1.79	1.75
-Cl	1.83	1.77
-Br	1.86	1.78
$-NO_2$	2.00	1.92

Supplementary Fig. 29. Am-R ligands for WOR. a, Synthesis of 6-oxo-6-(phenylamino) hexanoic acid-derived Am-R ligands (R = OCH_3, CH_3, H, F, Cl, Br, or NO_2) for photocatalytic WOR. **b,** Summary of both experimental and computed oxidation potentials. **c,** TON of O_2 for Am-R modified **MOZ-5** after 6-hour reactions under photocatalytic conditions. Data are presented as mean ± s.d. (n= 3) with the error bars representing the s.d.; individual data points are shown as black dots. **d,** Energy diagram of **MOZ-7**-catalyzed WOR. **e,** Representative model structure of TS3 of **MOZ-7**-catalyzed WOR. All atoms are labeled as follows: H, white; C, gray; O, red; N, blue; Ir, orange; Zr, light blue; Cl, light green. Ir-oxo, H_2O, and Am-Cl are highlighted.

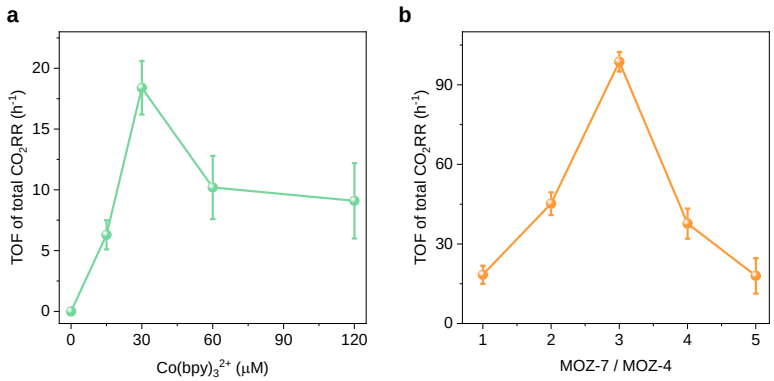

Supplementary Fig. 30. Optimization of activity for photocatalytic total CO_2RR. a, TOF of photocatalytic total CO_2RR by MOZs with different concentration of $Co(bpy)_3^{2+}$. **b,** TOF of photocatalytic total CO_2RR by MOZs with different ratio of **MOZ-7** to **MOZ-4**. In **a-b**, Data are presented as mean ± s.d. (n= 3) with the error bars representing the s.d.

Supplementary Tables

Supplementary Table 1. Summary of photocatalytic CO_2RR with different catalytic systems

Name	Reaction conditions[a]	TOF_{CO}; TOF_{CH4} (h^{-1}/ μmol·g^{-1}·h^{-1})	QYs	selectivity	References
Metal-organic-zymes reported in this work[b]					
Homo control	Xe lamp; DMA; r.t.; 1 atm	8.7±1.8/6632±1403(299.2±63.3)[c]; 4.8±1.4/924±261(41.7±11.8)[c]	0.004%	78.6%	This work
MOZ-1	Xe lamp; DMA; r.t.; 1 atm	72.5±5.2/55481.9±3953.9(2503±178)[c]; 71.2±.2/13615.3±988.5(614.2±44.6)[c]	0.056%	92.1%	
MOZ-2	Xe lamp; DMA; r.t.; 1 atm	146.5±11.8/112112±9056(5058±408)[c]; 101.3±15.3/19386±2934(874.7±132.4)[c]	0.073%	80.9%	
	Sunlight; DMA; r.t.; 1 atm	134.0/102027(3139.3)[c]; 91.5/17417(535.9)[c]	1.1%	96.7%	
MOZ-3	Xe lamp; DMA; r.t.; 1 atm	261.0±18.5/199734±14157(9011±638)[c]; 132.7±5.6/ 25381±1084(1145±48)[c]	0.14%	97.4%	
	sunlight; DMA; r.t.; 1 atm	199.3/151752(4707.2)[c]; 103.8/19759(612.9)[c]	1.2%	>99%	
MOZ-4	Xe lamp; DMA; r.t.; 1 atm	450.8±22.8/345008±17473(15566±788)[c]; 191.0±20.3/36541±3890(1648±175)[c]	0.21%	98.0%	
	Sunlight; DMA; r.t.;1 atm	308.8/235327(6495.4)[c]; 150.8/28730(793.0)[c]	1.8%	>99%	
Metal-organic complexes					
Fe-*p*-TMA and $Ir(ppy)_3$	AM 1.5 lamp; MeCN; r.t.; 1 atm	5.1/11133(142.8)[b]; 1.4/764(9.8)[b]	0.18%	82%	17
Fe-*p*-TMA and organic PS	AM 1.5 lamp; DMF; r.t.; 1 atm	1.5/700(10.0)[b]; 0.30/35(0.5)[b]	0.47%	85%	24
Metal & metal oxide-based nanoparticles					
Cu/TiO_2	UV lamp; H_2O; r.t.; 1 atm	Not reported; N.A./0.18	Not reported	Not reported	94
$Cu_{0.33}Pt_{0.67}@TiO_2$	AM 1.5 lamp; N.A.; r.t.; no report.	Not reported; 8.6/134	Not reported	Not reported	95
$Pt@Cu_2O/TiO_2$	Xe lamp; N.A.; 50; 0.2 MPa	0.032/8.3; 0.51/33	Not reported	85%	28
Au/TiO_2	UV lamp; N.A.; 75; 1 atm	Not reported; N.A./2.3	2.3%	Not reported	96
Pt/N-doped TiO_2	Xe lamp; N.A.; 45; 1 atm	Not reported; 4.5/5.7	Not reported	Not reported	97
$(MgO,Pt)/TiO_2$	Xe lamp; N.A.; 50; 0.2 MPa	0.0023/0.03; 3.4/11	Not reported	81%	29
Ag/TiO_2	Xe lamp; N.A.; 50; 0.2 MPa	0.073/1.7; 0.36/2.1	Not reported	39%	29
Pd/TiO_2	Xe lamp; N.A.; 50; 0.2 MPa	0.047/1.1; 0.74/4.3	Not reported	42%	29
Rh/TiO_2	Xe lamp; N.A.; 50; 0.2 MPa	0.026/0.62; 0.58/3.5	Not reported	45%	29
Pt/TiO_2	Xe lamp; N.A.; 80; 0.4 MPa	Not reported; 8.9/60	Not reported	75%	30

In/TiO_2	Hg lamp; N.A.; 100; 2 kPa	0.53/230; 6.2/675	Not reported	Not reported	98
TiO_2/MWCNT	UV lamp; N.A.; r.t.; no report	Not reported; N.A./12	Not reported	Not reported	99
SEG-TiO_2	Hg lamp; N.A.; r.t.; no report	Not reported; N.A./500	Not reported	Not reported	100
(N_3-dye,Cu,Fe)/ TiO_2	Hg lamp; N.A.; 75; 1 atm	Not reported; 0.040/0.85	0.045%	Not reported	101
ZnPc/TiO_2	Tungsten-Halogen lamp; H_2O; no report; no report	23/201.3; 62/133	Not reported	Not reported	102
Pd_7Cu_1/TiO_2	Xe lamp; N.A.; no report; 0.2 MPa	Not reported; 0.027/19.6	Not reported	98%	31
(NiO,In_2O_3)/TiO_2	Hg lamp; N.A.; no report; 1 atm	0.49/60; 7.9/240	Not reported	Not reported	103
WO_3	Xe lamp; N.A.; r.t.; 1 atm	Not reported; N.A./1.0	Not reported	Not reported	104
Zn_2GeO_4	Xe lamp; N.A.; r.t.; 1 atm	Not reported; N.A./1.5	Not reported	Not reported	105
Pt/(g-C_3N_4/$NaNbO_3$)	Xe lamp; N.A.; no report; 1 atm	Not reported; N.A./6.4	Not reported	Not reported	106
$SrNb_2O_6$	Xe lamp; N.A.; 50; 0.2 MPa	N.A./1.7; N.A./0.33	0.065%	82%	107
Metal-organic frameworks					
$Cu_3(BTC)_2$@TiO_2	Xe lamp; N.A.; 40; 0.15 MPa	Not reported; 0.0069/2.63	Not reported	100%	32
MOF-525-Co	Xe lamp; MeCN; no report; 80 kPa	0.43/200.6; 0.32/37	Not reported	Not reported	108
Perovskite					
$CsPbBr_3$ QD/GO	AM 1.5 lamp; EA; no report; no report	N.A./48.7; N.A./29.6	Not reported	99%	109

[a] Reaction conditions in the order of light source, reaction solvent, reaction temperature, and pressure of CO_2. N.A. refers to a gas-solid phase reaction without any solvent. [b] TOF are calculated based on initial reaction rate within 6 hours. [c] TOF_1(TOF_2), TOF_1 was calculated based on catalysts only; TOF_1 was calculated based on both catalysts and photosensitizers.

Supplementary Table 2. Summary of photocatalytic WOR with different catalytic systems

Name	Reaction conditions[a]	TOF (h^{-1}/ $\mu mol \cdot g^{-1} \cdot h^{-1}$)	QYs	Sacrificial Reagent	References
Metal-organic complexes and photosensitizers[b]					
Homo	Xe lamp; water and MeCN	10.5±0.3/1843±52(73.0±2.1)[e]	0.2%	$K_2S_2O_8$	This work
MOZ-5	Xe lamp; water and MeCN	52.0±7.2/8798±1218(257.6±35.7)[e]	1.0%	$K_2S_2O_8$	
MOZ-6	Xe lamp; water and MeCN	208.3±27.5/35224±4653(985.9±130.1)[e]	4.1%	$K_2S_2O_8$	
MOZ-7	Xe lamp; water and MeCN	240.5±11.2/30222±1407(1138±53)[e]	4.7%	$K_2S_2O_8$	
Metal-organic complexes and photosensitizers[b]					
$RuL(pic)_2$ and $Ru(bpy)_3^{2+}$	Xe lamp; pH = 7 water	2200/1038715(66020)[e]	Not reported	$Co(NH_3)_5Cl_3$	35
Di-Ru Complex and Ru-based PSs[c]	Xe lamp; pH = 7.2 water	1440/366943(2252)[e] 11088/2825458(14173)[e] 11952/3045623(12917)[e]	0.7% 4.5% 9.7%	$Na_2S_2O_8$	110
$[IrClCp^*(di\text{-}NHC)](PF_6)$ and $Ru(bpy)_3^{2+}$	LED at 450 nm; pH = 5.2 water	29/10264(1020)[e]	3.8%	$Na_2S_2O_8$	111
Metal-organic frameworks and photosensitizers					
CoO_x/MIL-101 and $Ru(bpy)_3^{2+}$	Xe lamp; pH = 9 water	173/24219(7683)[e]	Not reported	$Na_2S_2O_8$	36
Semiconductor-based photocatalysts					
$Rh@Cr_2O_3/Ga_{1-x}Zn_xN_{1-x}O$	Xe lamp; pH=4.5 water	Not reported	51%	$AgNO_3$	37
Ta_3N_5	Xe lamp; neutral water	N.A.[d]/2100	10%	$AgNO_3$	112
$Sm_2Ti_2S_2O_5$	Xe lamp; pH = 8 water	N.A.[d]/18	0.2%	$AgNO_3$	113
IrO2-$Ca(OH)_2$ /$Sm_2Ti_2S_2O_5$	Xe lamp; pH = 8 water	17/47	1.1%	$AgNO_3$	113
$IrO_2/Y_2Ti_2O_2S_2$	Xe lamp; pH = 8 water	8.3/93	2.3%	$AgNO_3$	38
RuO_2/Bi_4TaO_8X (X = Cl,Br)	Xe lamp; neutral water	200/375	20%	$Fe(NO_3)_3$	114
Pt/Bi_4NbO_8Cl	Xe lamp; pH = 2.5 water	62/400	0.4%	$FeCl_3$	115
Au, $CoO_x/BiVO_4$	Xe lamp; pH = 6.0 water	492/1640	Not reported	$[Fe(CN)_6]^{3-}$	116

[a] Reaction conditions in the order of light source and reaction solvent. All reactions were done at room temperature. [b] TOF are calculated based on initial reaction rate within 6 hours. [c] TOF and quantum efficiency results are from different photosensitizers. [d] Pure semiconductor catalyzed reactions without cocatalysts have no molecular active site. [e] TOF_1(TOF_2), TOF_1 was calculated based on catalysts only; TOF_1 was calculated based on both catalysts and photosensitizers.

Supplementary Table 3. Summary of photocatalytic total CO_2RR with different catalytic systems

Catalyst	Experimental Condition	Reduction Product	Oxidation Product	TOF of CO_2RR (h^{-1})	Reference
MOZ-4 + **MOZ-7**	300 W Xe lamp (> 300 nm)	CO, CH_4	O_2	98.7 ± 3.7	This work
$Bi_2O_2CO_3$/$CoFe_2O_4$/g-C_3N_4	800 W Xe lamp (> 400 nm),	CO, CH_4	Not mentioned	Not mentioned	39
α-Fe_2O_3/g-C_3N_4	300 W Xe lamp (> 420 nm)	CO	Not mentioned	0.022	40
Al bridged α-Fe_2O_3/g-C_3N_4	300 W Xe lamp, 2.6 bar CO_2	CO, CH_4	O_2	6.2×10^{-3}	41
ZnO-Cu_2O	300 W Xe lamp (>420 nm)	CH_4	Not mentioned	1.94	42
CdS/WO_3	300 W Xe lamp (> 420 nm)	CH_4	Not mentioned	0.024	43
Cu_2O/TiO_2	1kW Hg lamp (> 305 nm)	CO	O_2	2.6×10^{-4}	44
α-Fe_2O_3/g-C_3N_4	300 W Xe lamp	CO	O_2	0.0097	45
$ZnIn_2S_4$/$BiVO_4$	300 W Xe lamp	CO	O_2	0.032	46
Bi_2S_3 QDs/g-C_3N_4	300 W Xe lamp	CO, CH_4	O_2	0.0325	47
TiO_2 in MIL-101-Cr-NO_2	300 W Xe lamp	CO, CH_4	O_2	5.9	48
WO_3	40 W silicon nitride lamp (λ=800-1700 nm)	CO	O_2	1.3×10^{-3}	49
$MAPbI_3$@PCN-221(Fe0.2)	300 W Xe-lamp (>400 nm)	CO, CH_4	O_2	0.67	50
PCN-601	Xe-lamp (>410 nm)	CO, CH_4	H_2O_2	0.23	117
$ZrOCo^{II}$-IrO_x	Laser (355 nm)	CO	O_2	6.5×10^{-4}	118
$ZrOCo^{II}$-Co_3O_4	480 mW Ar ion laser (476 nm)	CO	O_2	Not mentioned	119

Supplementary Table 4. Crystallographic information of Ur ligand.

Empirical formula	$C_{13}H_{12}F_6N_2O_3$
Formula weight	358.25
Temperature/K	100
Crystal system	monoclinic
Space group	P21/n
a/Å	8.4706(4)
b/Å	11.5578(5)
c/Å	14.1311(7)
α/°	90
β/°	92.6870(10)
γ/°	90
Volume/Å^3	1381.93(11)
Z	4
ρ_{calc}g/cm^3	1.722
μ/mm^{-1}	0.174
F(000)	728.0
Crystal size/mm^3	0.1 × 0.1 × 0.1
Radiation	synchrotron (λ = 0.41328)
2Θ range for data collection/°	2.648 to 36.478
Index ranges	$-12 \leq h \leq 11$, $-17 \leq k \leq 17$, $-21 \leq l \leq 21$
Reflections collected	21573
Independent reflections	4932 [R_{int} = 0.0469, R_{sigma} = 0.0339]
Data/restraints/parameters	4932/0/218
Goodness-of-fit on F^2	1.003
Final R indexes [I>=2σ (I)]	R_1 = 0.0726, wR_2 = 0.1893
Final R indexes [all data]	R_1 = 0.0877, wR_2 = 0.1966
Largest diff. peak/hole / e Å^{-3}	1.60/-1.06
CCDC	2000080
Note	There are 5 B-level alerts in the single crystal structure of Ur ligand, which were all caused by the crystallographic disorder of one -CF_3 group.

Supplementary NMR Spectra

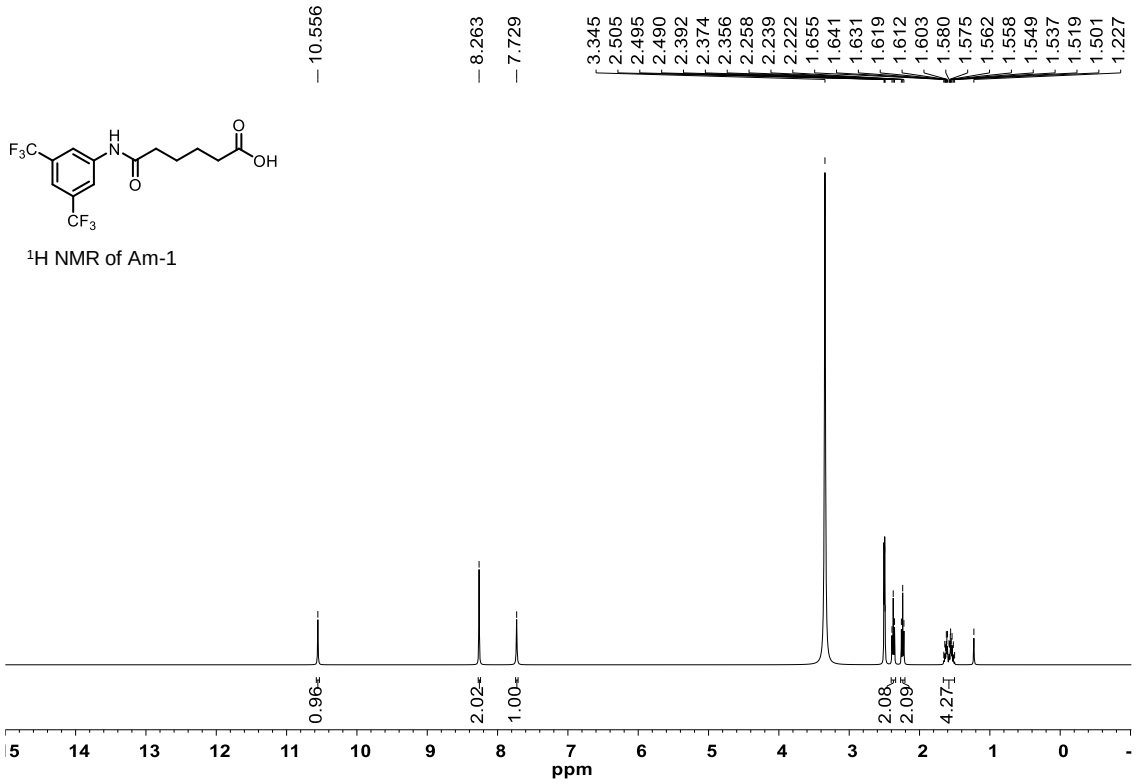

^{1}H NMR of Am-1

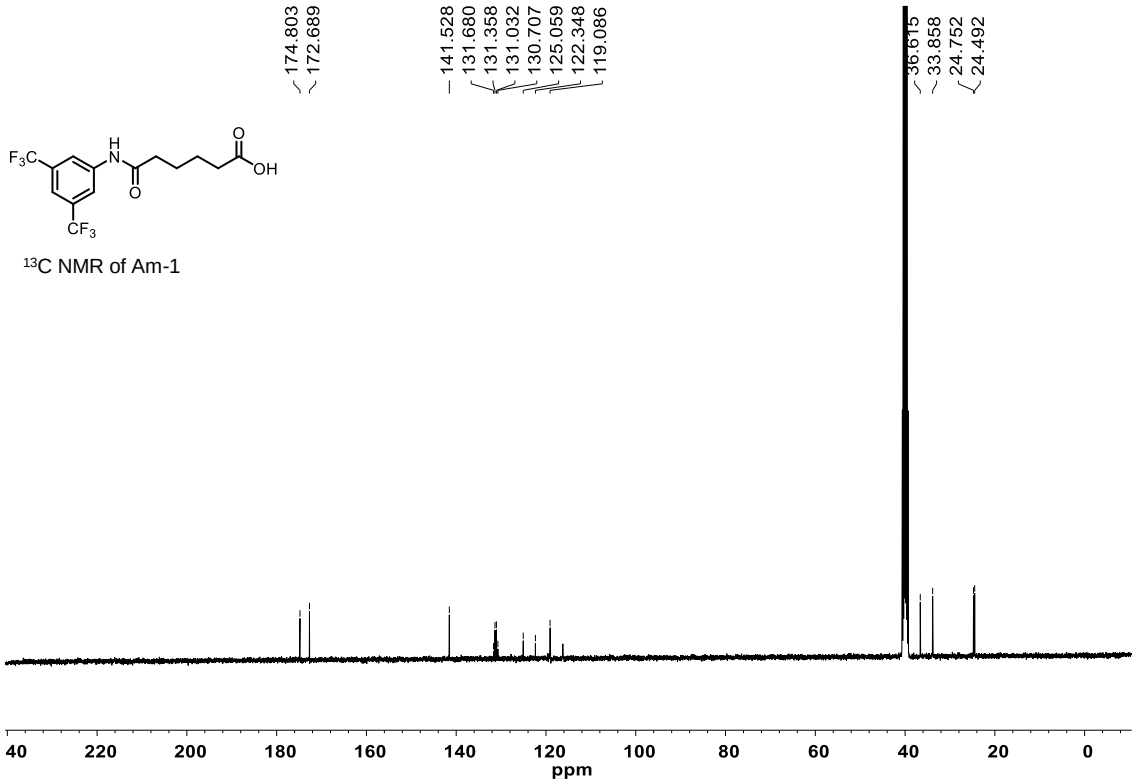

^{13}C NMR of Am-1

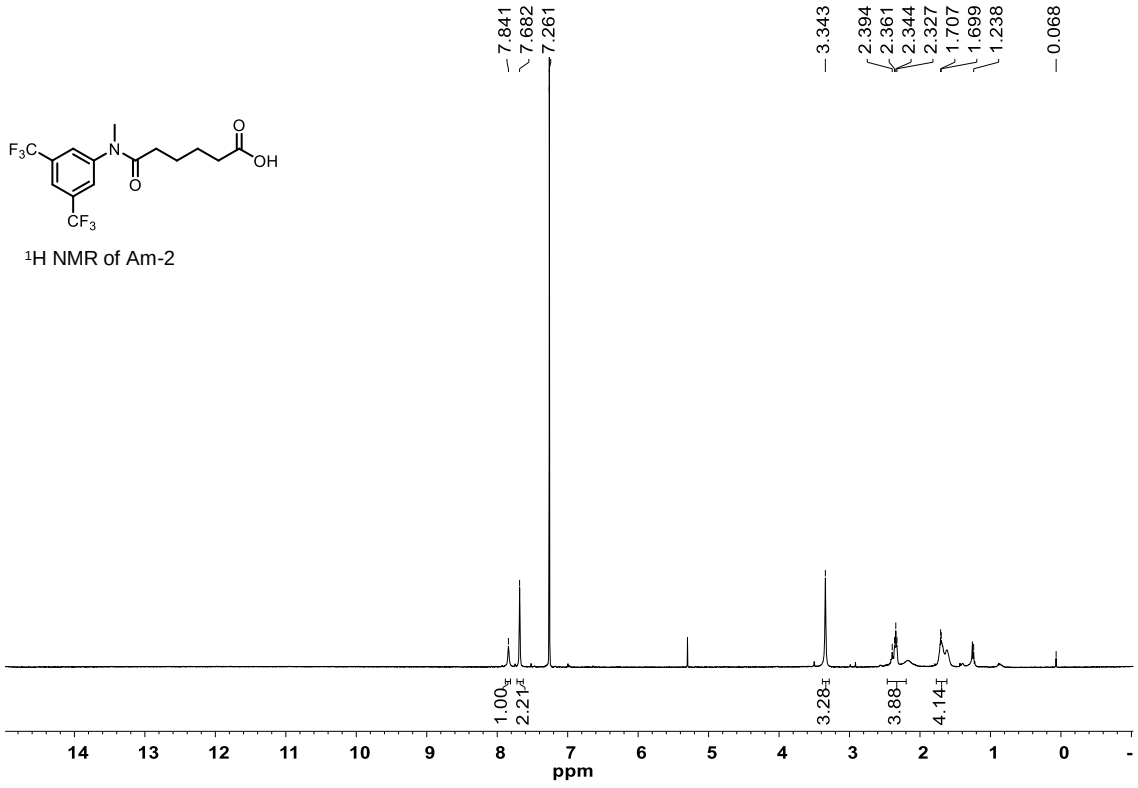

^{1}H NMR of Am-2

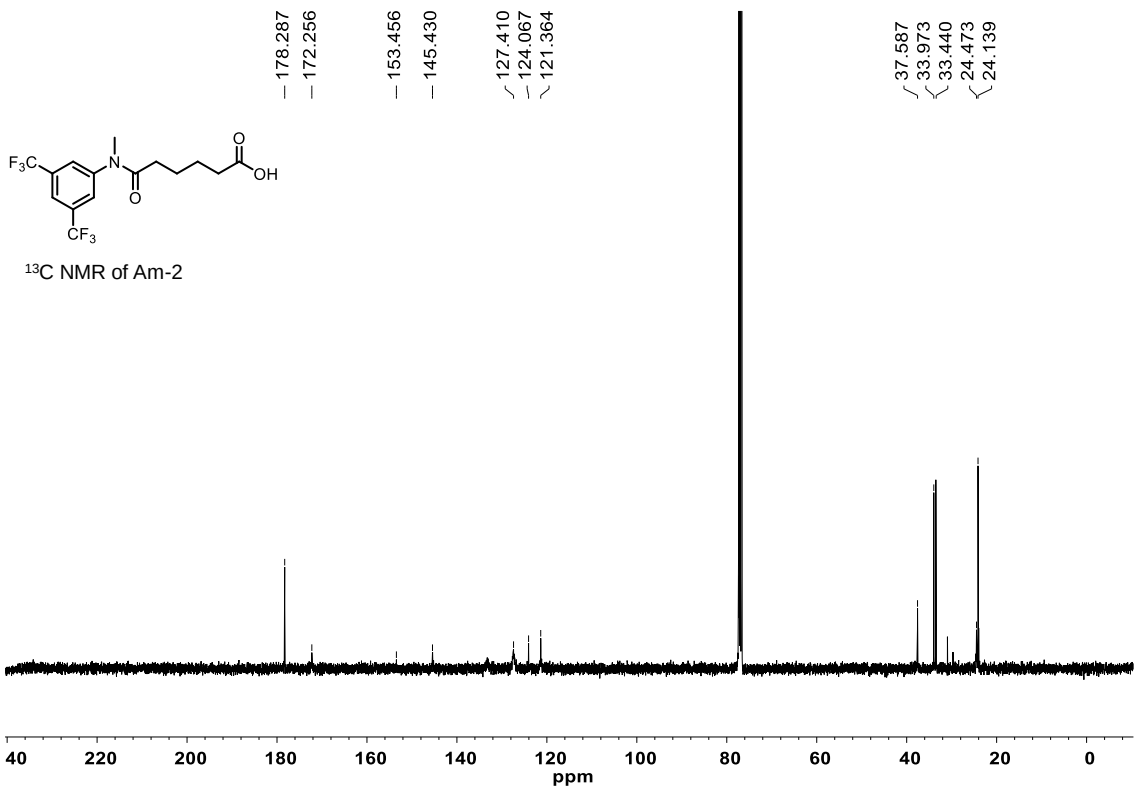

^{13}C NMR of Am-2

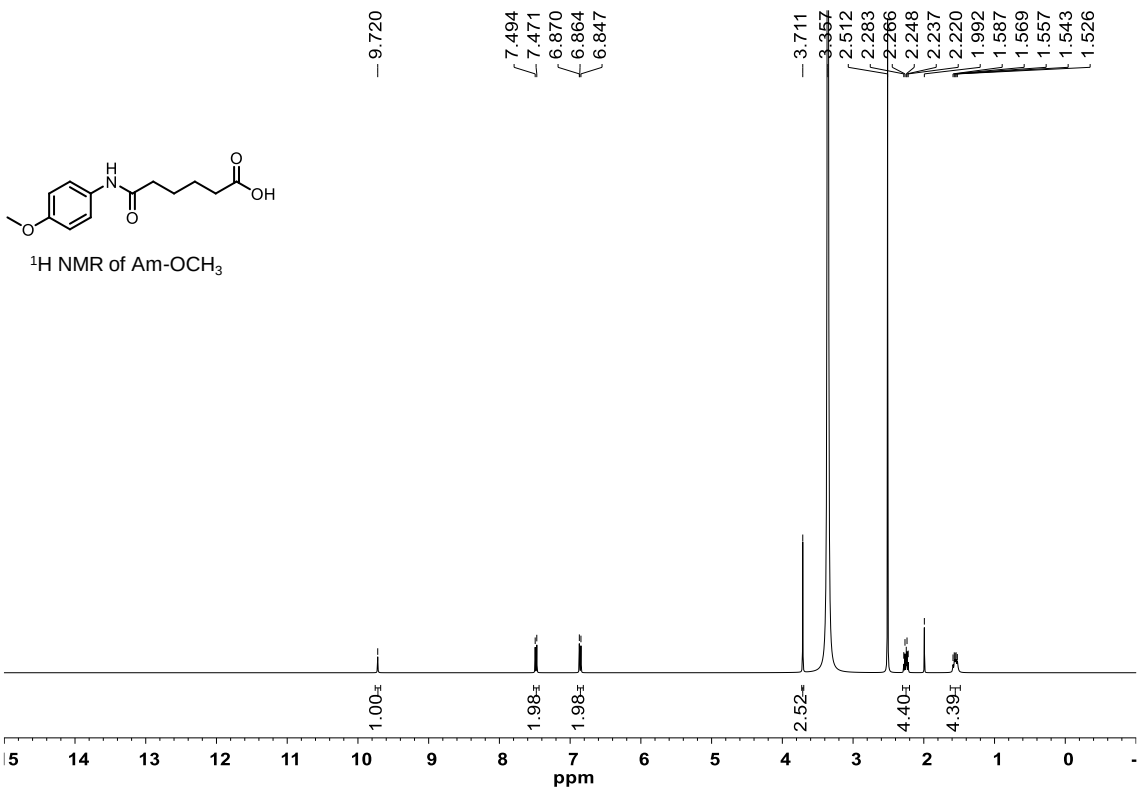

^{1}H NMR of Am-OCH$_3$

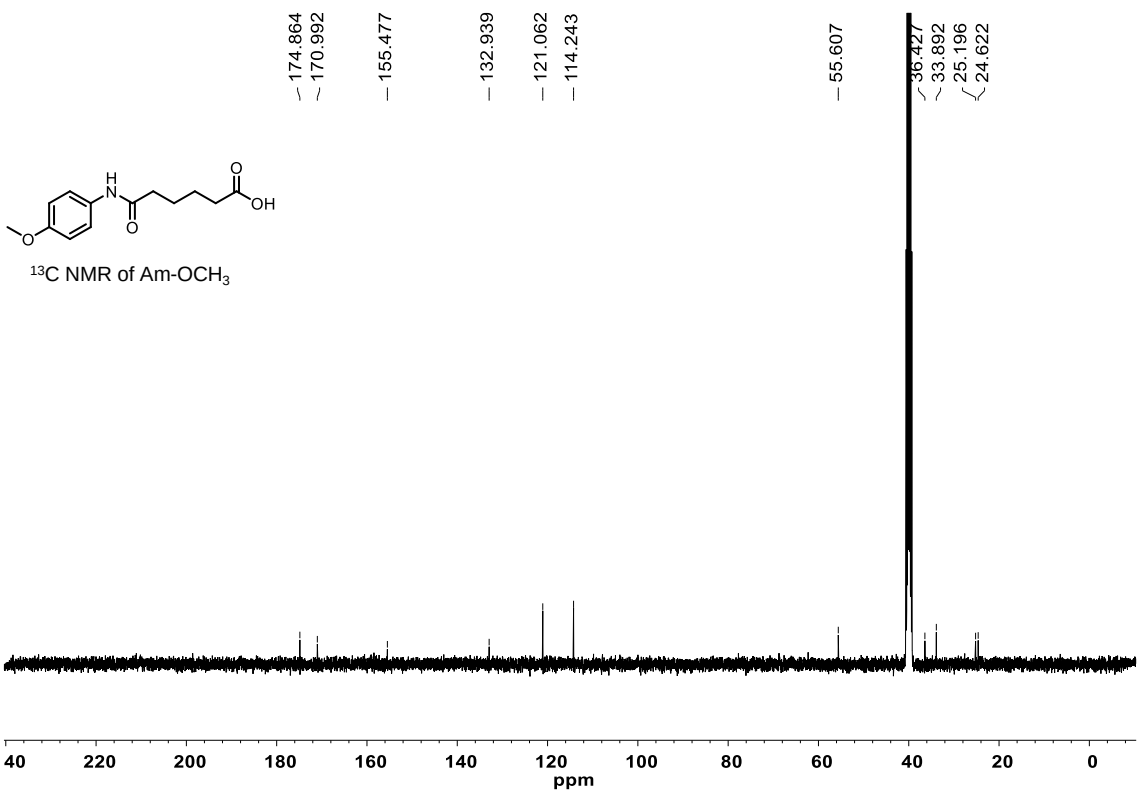

^{13}C NMR of Am-OCH$_3$

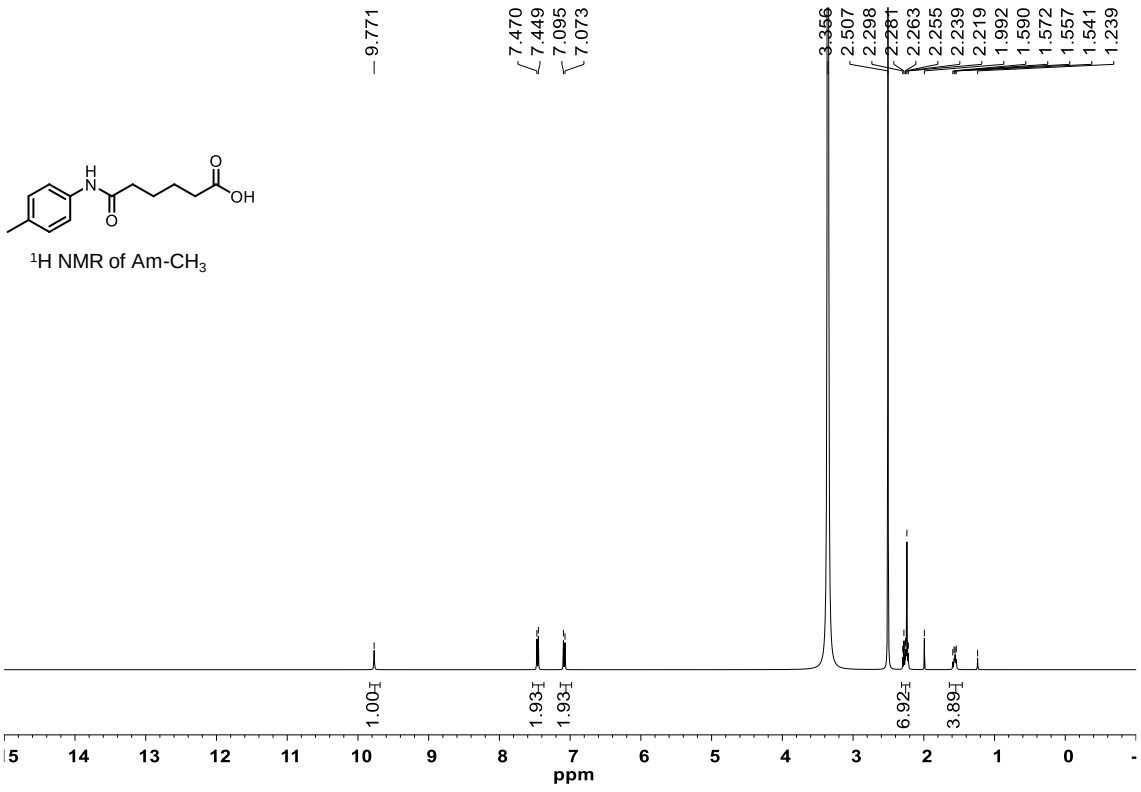

^{1}H NMR of Am-CH_3

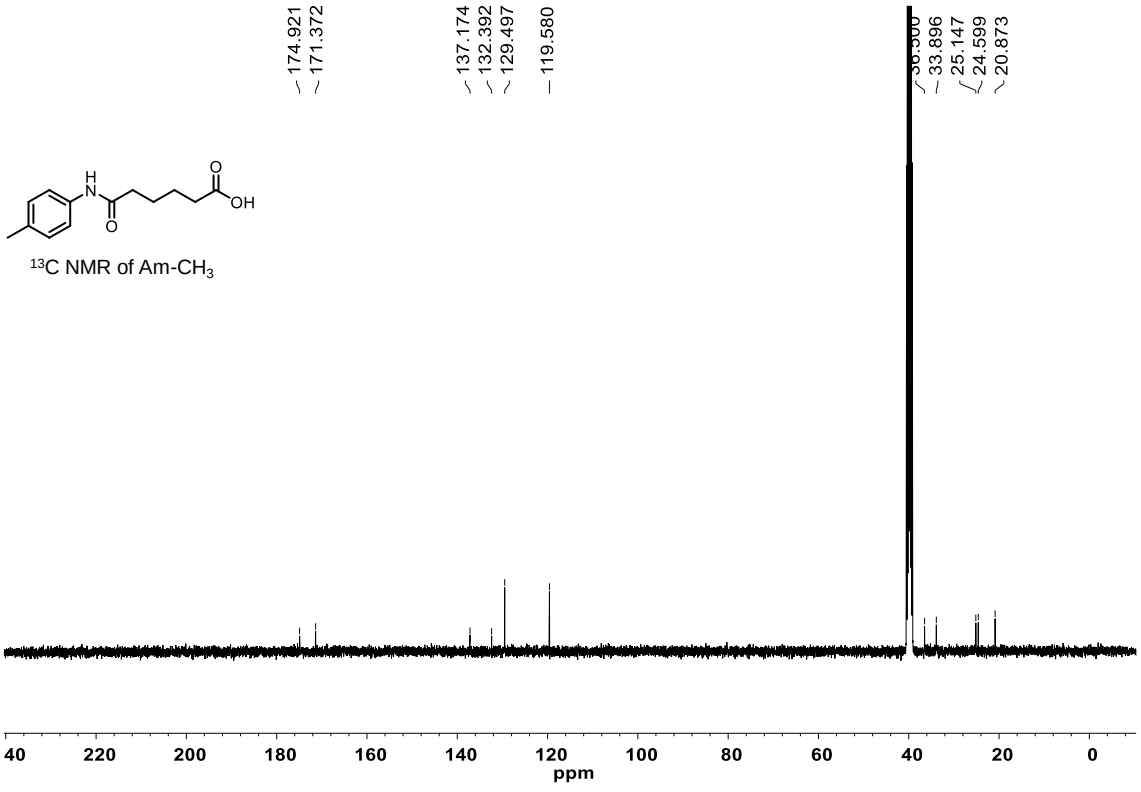

^{13}C NMR of Am-CH_3

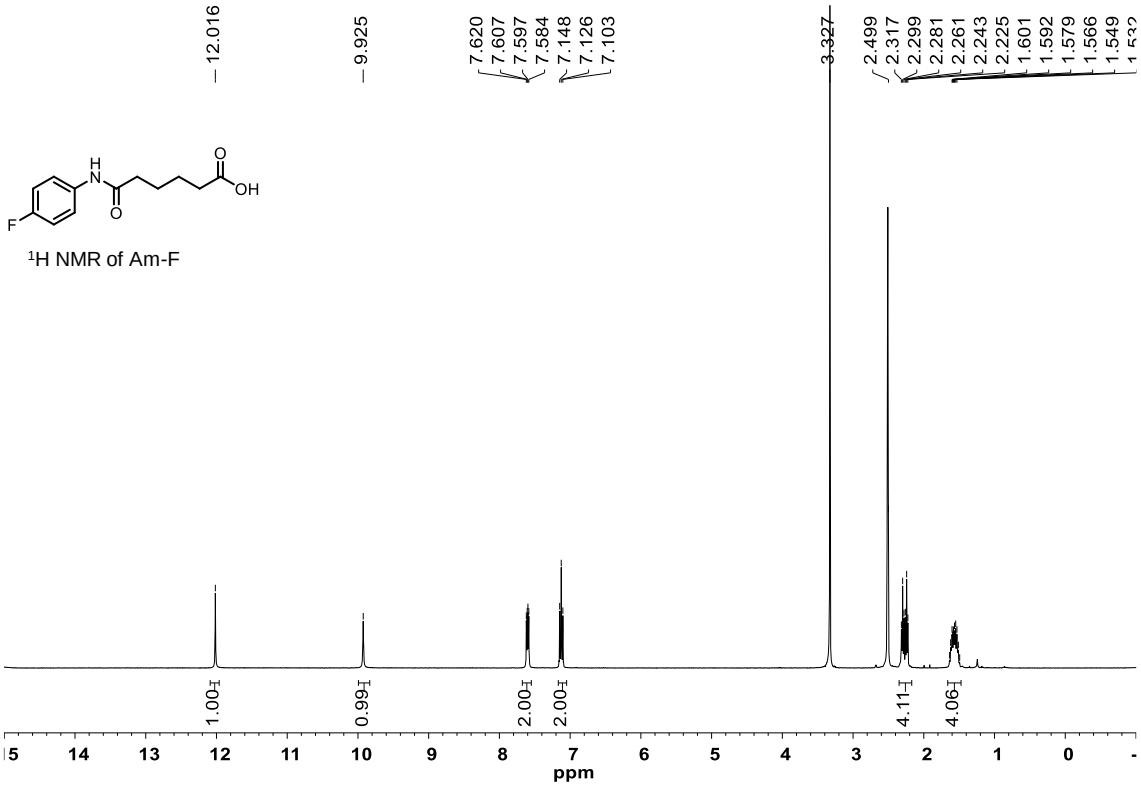

^{1}H NMR of Am-F

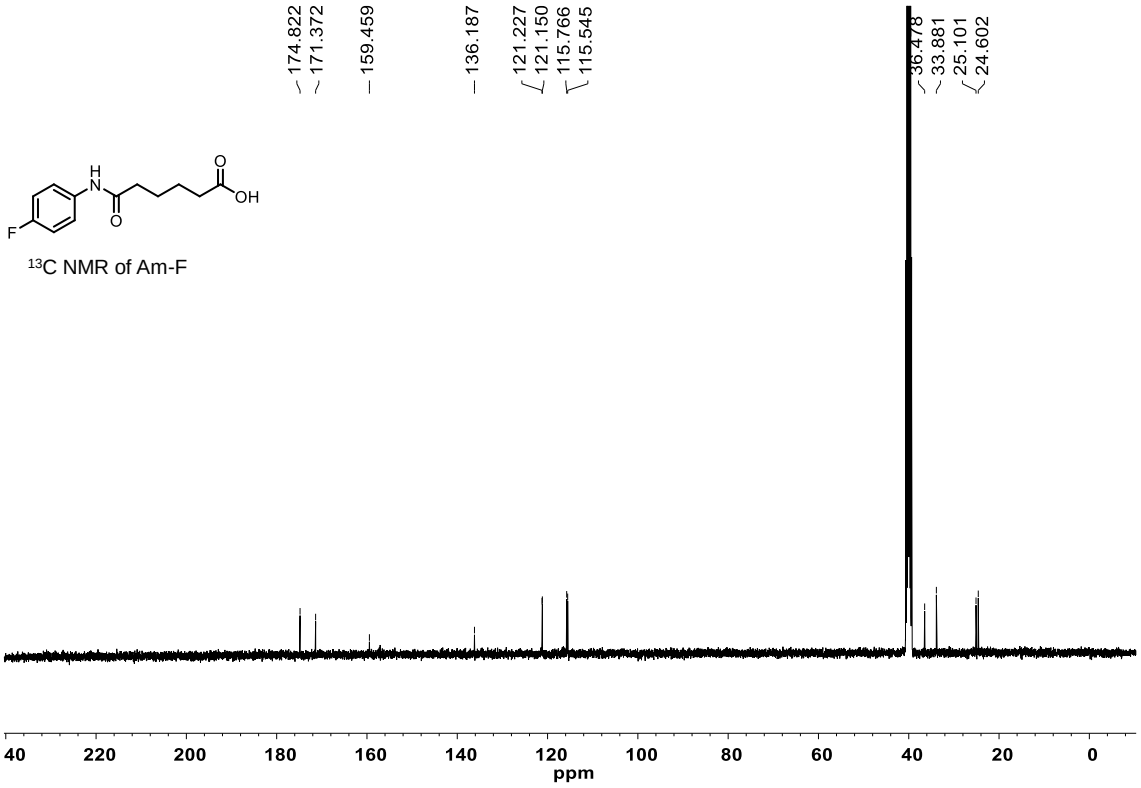

^{13}C NMR of Am-F

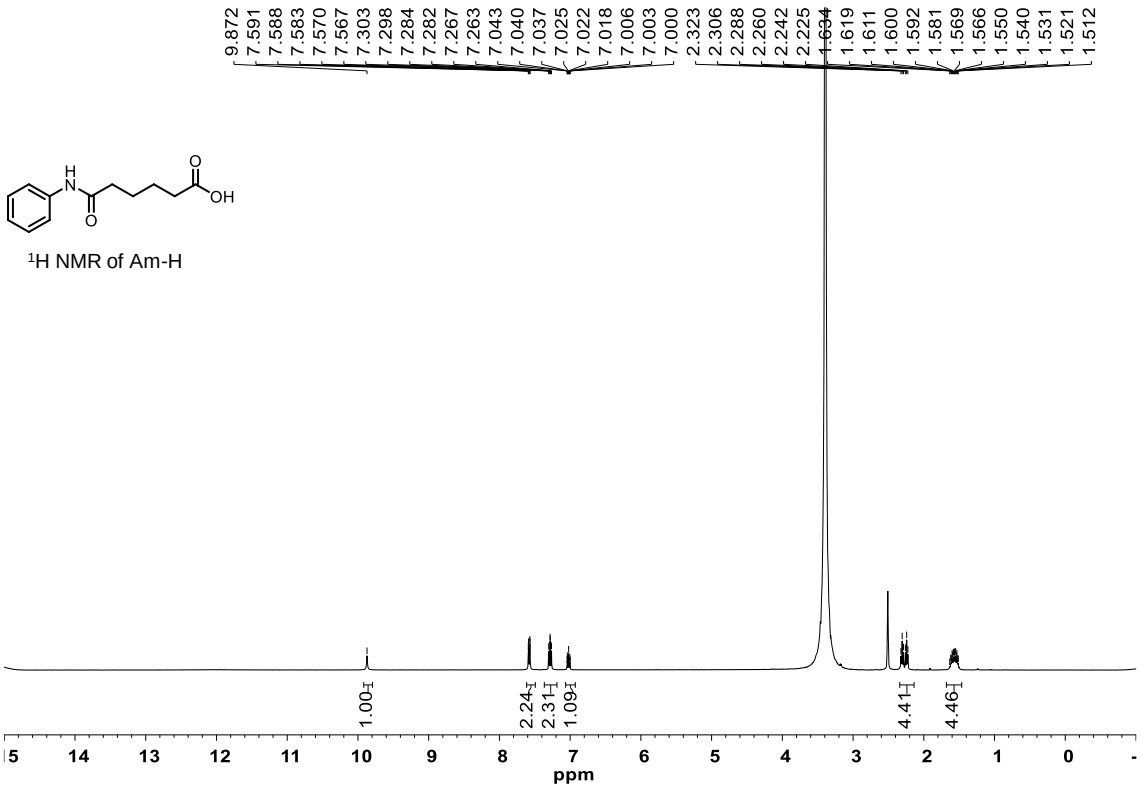

^{1}H NMR of Am-H

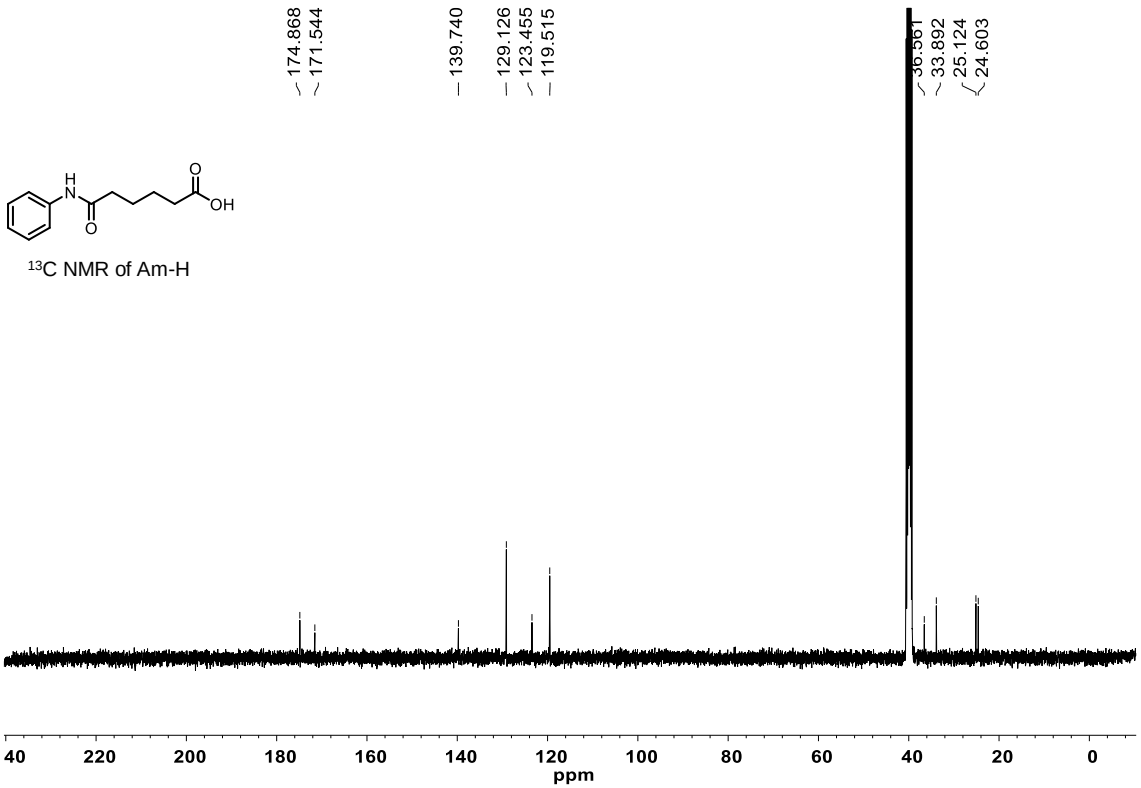

^{13}C NMR of Am-H

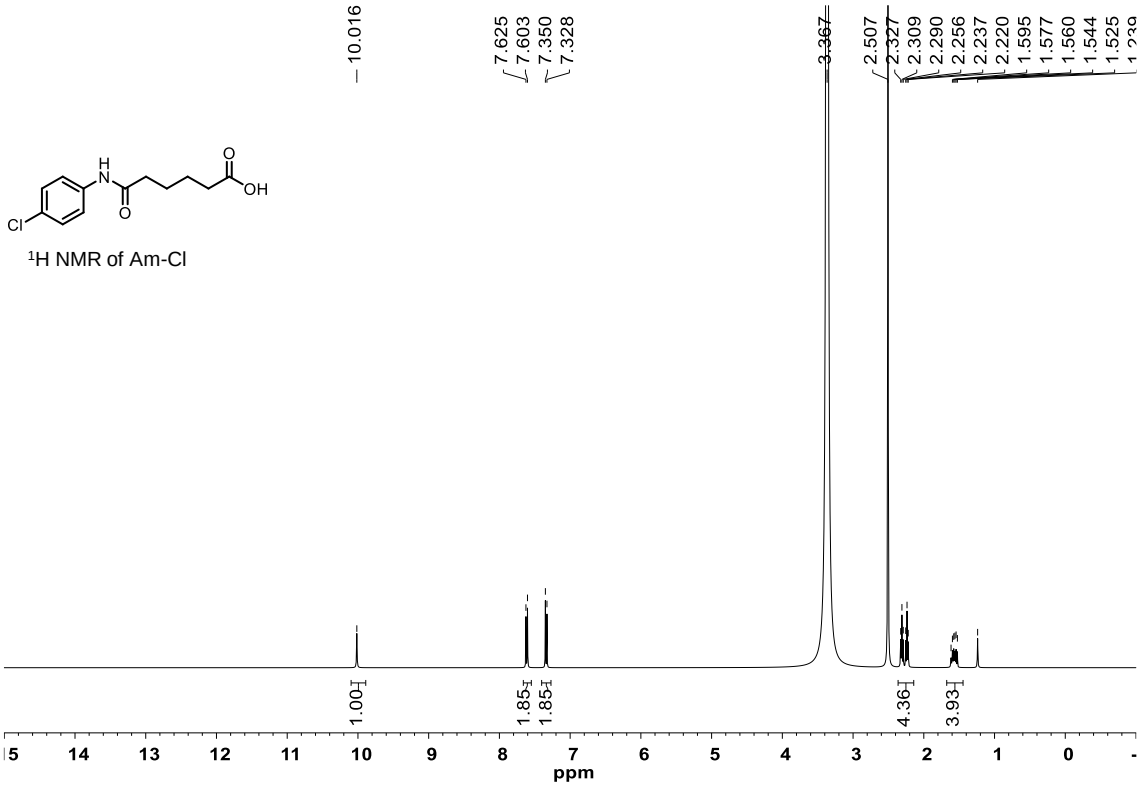

^{1}H NMR of Am-Cl

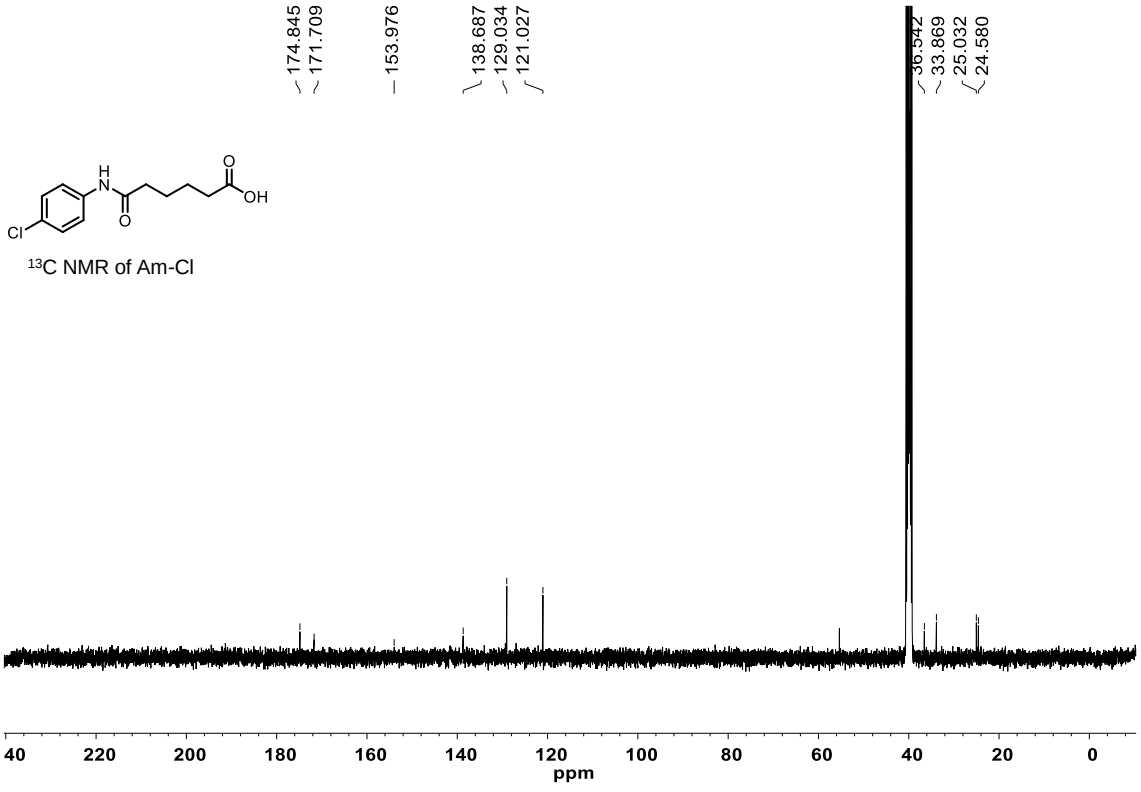

^{13}C NMR of Am-Cl

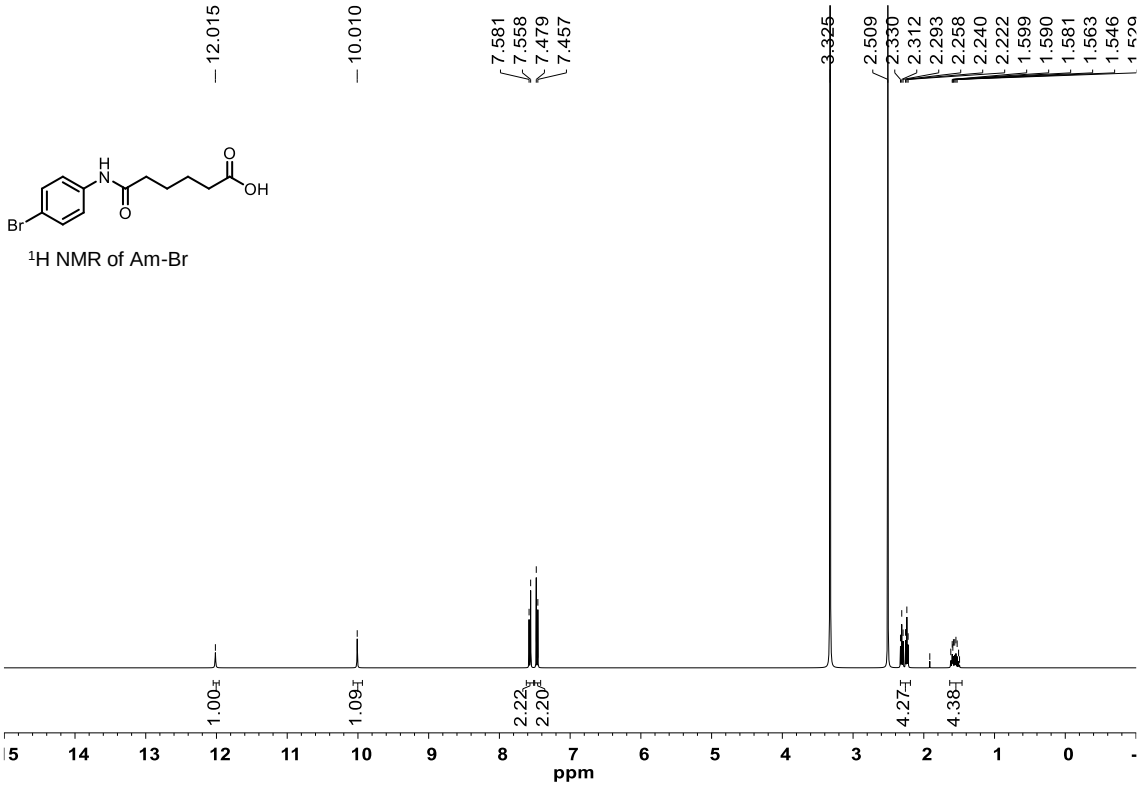

^{1}H NMR of Am-Br

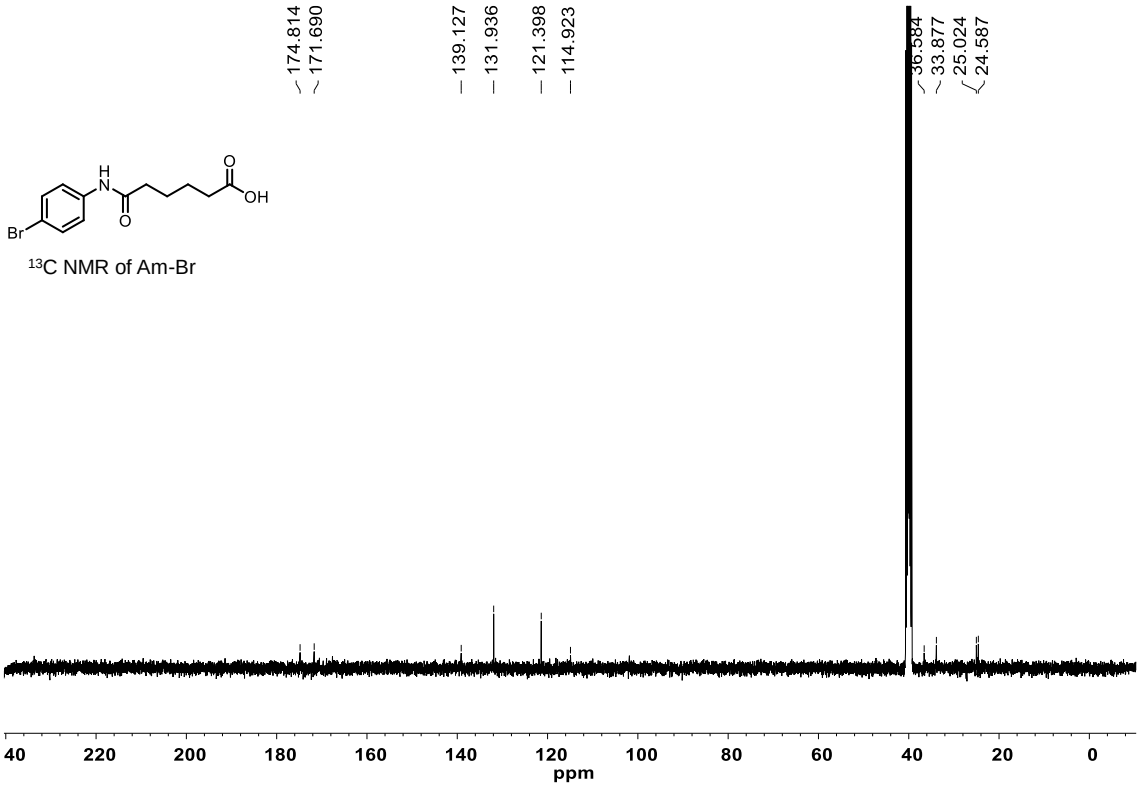

^{13}C NMR of Am-Br

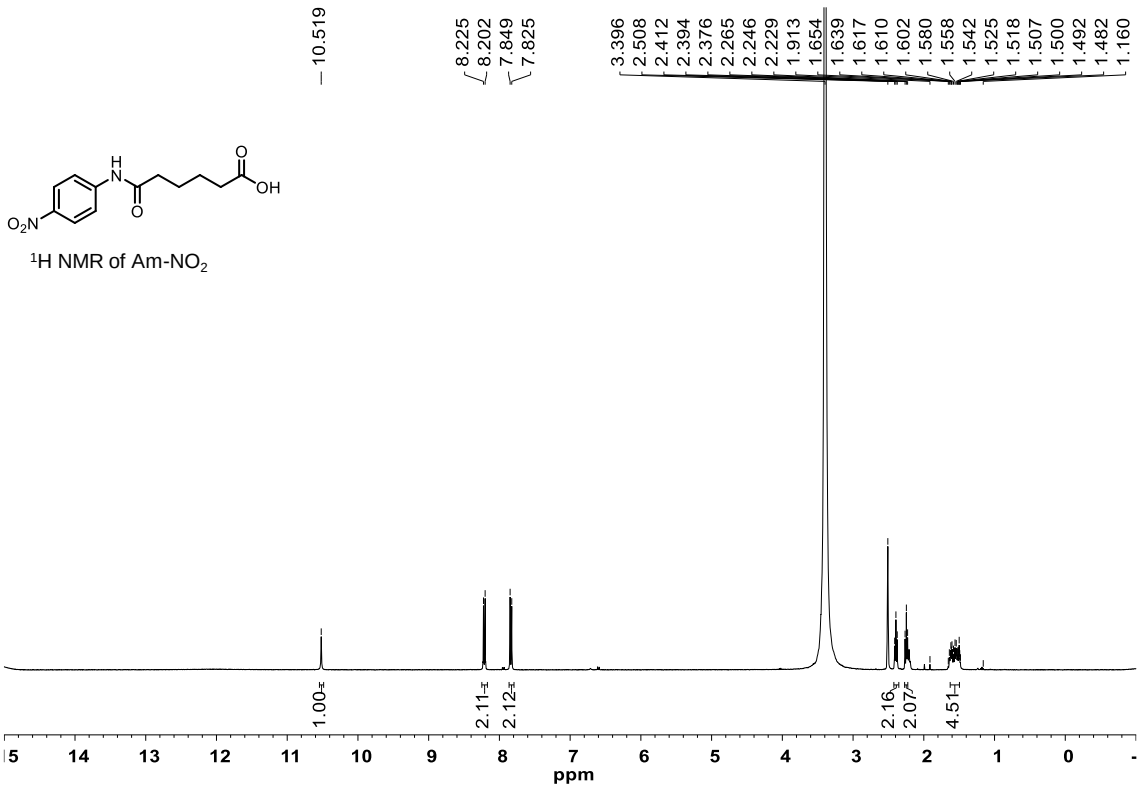

^{1}H NMR of Am-NO_2

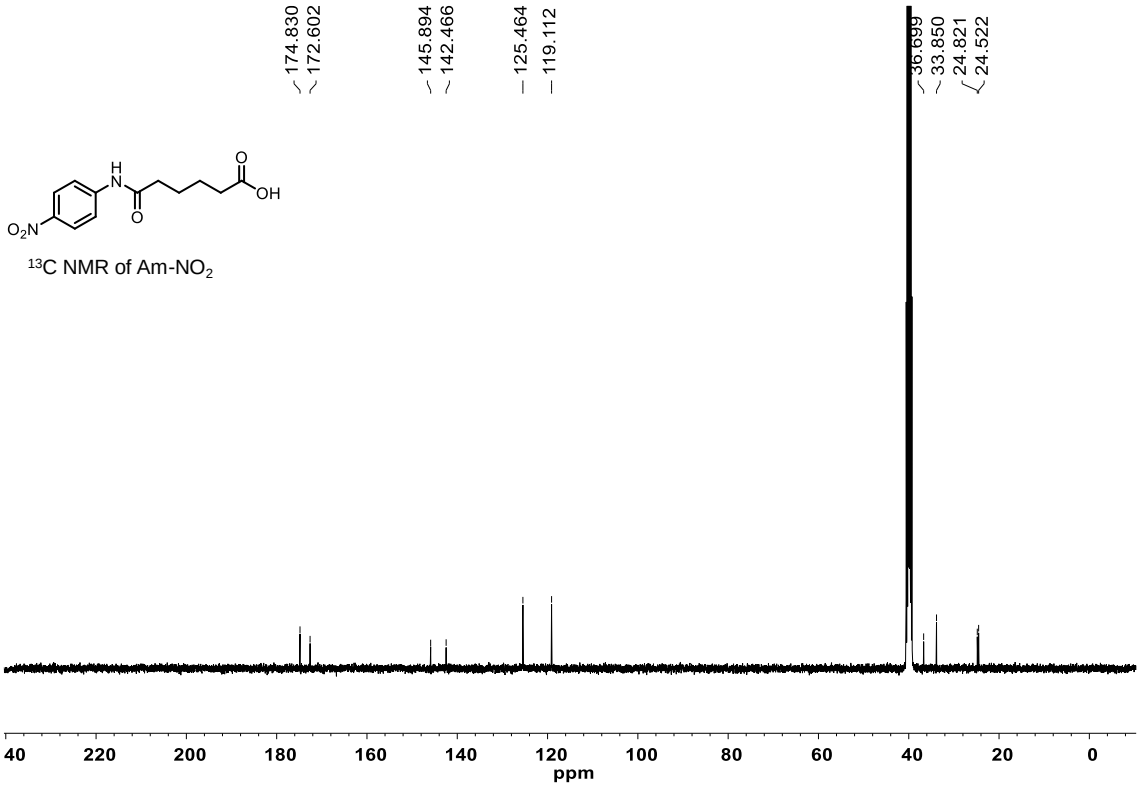

^{13}C NMR of Am-NO_2

Supplementary References

60 Kang, J. W., Moseley, K. & Maitlis, P. M. J. J. o. t. A. C. S. Pentamethylcyclopentadienylrhodium and-iridium halides. I. Synthesis and properties. **91**, 5970-5977 (1969).

61 Dai, R. *et al.* Electron Crystallography Reveals Atomic Structures of Metal–Organic Nanoplates with $M_{12}(\mu_3\text{-}O)_8(\mu_3\text{-}OH)_8(\mu_2\text{-}OH)_6$ (M = Zr, Hf) Secondary Building Units. *Inorg. Chem.* **56**, 8128-8134 (2017).

62 Das, D. K. & Medhi, O. K. The role of heme propionate in controlling the redox potential of heme: Square wave voltammetry of protoporphyrinato IX iron(III) in aqueous surfactant micelles. *J. Inorg. Biochem.* **70**, 83-90 (1998).

63 Quan, Y. *et al.* Metal–Organic Layers for Synergistic Lewis Acid and Photoredox Catalysis. *J. Am. Chem. Soc.* **142**, 1746-1751 (2020).

64 Planas, N. *et al.* Defining the Proton Topology of the Zr6-Based Metal–Organic Framework NU-1000. *J. Phy. Chem. Lett.* **5**, 3716-3723 (2014).

65 Erickson, H. P. Size and shape of protein molecules at the nanometer level determined by sedimentation, gel filtration, and electron microscopy. *Biol. Proced. Online* **11**, 32-51 (2009).

66 Zhu, Y.-Y. *et al.* Merging Photoredox and Organometallic Catalysts in a Metal–Organic Framework Significantly Boosts Photocatalytic Activities. *Angew. Chem. Int. Ed.* **57**, 14090-14094 (2018).

67 Bhugun, I., Lexa, D. & Savéant, J.-M. Homogeneous Catalysis of Electrochemical Hydrogen Evolution by Iron(0) Porphyrins. *J. Am. Chem. Soc.* **118**, 3982-3983 (1996).

68 Collman, J. P., Brauman, J. I. & Doxsee, K. M. Carbon monoxide binding to iron porphyrins. *Proc. Natl. Acad. Sci. U. S. A.* **76**, 6035-6039 (1979).

69 Matwiyoff, N. A. *et al.* Carbon-13 nuclear magnetic resonance and infrared spectroscopic studies of carbon-13 monoxide binding to rabbit hemoglobin. *J. Am. Chem. Soc.* **95**, 4429-4431 (1973).

70 Gaussian 16 Rev. C.01 (Wallingford, CT, 2016).

71 Davethu, P. A. & de Visser, S. P. CO_2 Reduction on an Iron-Porphyrin Center: A Computational Study. *J. Phys. Chem. A* **123**, 6527-6535 (2019).

72 Hariharan, P. C. & Pople, J. A. The influence of polarization functions on molecular orbital hydrogenation energies. *Theor. Chim. Acta* **28**, 213-222 (1973).

73 Hay, P. J. & Wadt, W. R. Ab initio effective core potentials for molecular calculations. Potentials for the transition metal atoms Sc to Hg. *J. Chem. Phys.* **82**, 270-283 (1985).

74 Hay, T. H. D. J. a. P. J. in Modern Theoretical Chemistry. **Ed. H. F. Schaefer III, Vol. 3 (Plenum, New York, 1977)**.

75 Troya, D. Reaction Mechanism of Nerve-Agent Decomposition with Zr-Based Metal Organic Frameworks. *J. Phys. Chem. C* **120**, 29312-29323 (2016).

76 Moon, S.-Y., Liu, Y., Hupp, J. T. & Farha, O. K. Instantaneous Hydrolysis of Nerve-Agent Simulants with a Six-Connected Zirconium-Based Metal–Organic Framework. *Angew. Chem. Int. Ed.* **54**, 6795-6799 (2015).

77 Wang, C., Wang, J.-L. & Lin, W. Elucidating Molecular Iridium Water Oxidation Catalysts Using Metal–Organic Frameworks: A Comprehensive Structural, Catalytic, Spectroscopic, and Kinetic Study. *J. Am. Chem. Soc.* **134**, 19895-19908 (2012).

78 Pasha, F. A. *et al.* Revisiting O–O Bond Formation through Outer-Sphere Water Molecules versus Bimolecular Mechanisms in Water-Oxidation Catalysis (WOC) by Cp*Ir Based Complexes. *Eur. J. Inorg. Chem.* **2019**, 2093-2100 (2019).

79 Becke, A. D. J. P. r. A. Density-functional exchange-energy approximation with correct asymptotic behavior. *Phys. Rev. A* **38**, 3098 (1988).

80 Lee, C., Yang, W. & Parr, R. G. J. P. r. B. Development of the Colle-Salvetti correlation-energy formula into a functional of the electron density. *Phys. Rev. B* **37**, 785 (1988).
81 Raghavachari, K. J. T. C. A. Perspective on "Density functional thermochemistry. III. The role of exact exchange". *Theor. Chem. Acc.* **103**, 361-363 (2000).
82 Gaussian 16 Rev. A.03 (Wallingford, CT, 2016).
83 Grimme, S., Antony, J., Ehrlich, S. & Krieg, H. A consistent and accurate ab initio parametrization of density functional dispersion correction (DFT-D) for the 94 elements H-Pu. *J. Chem. Phys.* **132**, 154104 (2010).
84 Marenich, A. V., Cramer, C. J. & Truhlar, D. G. Universal Solvation Model Based on Solute Electron Density and on a Continuum Model of the Solvent Defined by the Bulk Dielectric Constant and Atomic Surface Tensions. *J. Phys. Chem. B* **113**, 6378-6396 (2009).
85 Camaioni, D. M. & Schwerdtfeger, C. A. A. Comment on "Accurate experimental values for the free energies of hydration of H^+, OH^-, and H_3O^+". *J. Phys. Chem. A* **109**, 10795-10797 (2005).
86 Kelly, C. P., Cramer, C. J. & Truhlar, D. G. Aqueous Solvation Free Energies of Ions and Ion−Water Clusters Based on an Accurate Value for the Absolute Aqueous Solvation Free Energy of the Proton. *J. Phys. Chem. B* **110**, 16066-16081 (2006).
87 Tissandier, M. D. *et al.* The Proton's Absolute Aqueous Enthalpy and Gibbs Free Energy of Solvation from Cluster Ion Solvation Data. *J. Phys. Chem. A* **102**, 9308-9308 (1998).
88 Montgomery, J. A., Frisch, M. J., Ochterski, J. W. & Petersson, G. A. A complete basis set model chemistry. VII. Use of the minimum population localization method. *J. Chem. Phys.* **112**, 6532-6542 (2000).
89 Drago, R. S. *Physical methods for chemists*. 585 (Surfside, 1992).
90 Mashiko, T., Reed, C. A., Haller, K. J. & Scheidt, W. R. Nature of iron(I) and iron(0) tetraphenylporphyrin complexes. Synthesis and molecular structure of (dibenzo-18-crown-6)bis(tetrahydrofuran)sodium (meso-tetraphenylporphinato)ferrate and bis[tris(tetrahydrofuran)sodium] (meso-tetraphenylporphinato)ferrate. *Inorg. Chem.* **23**, 3192-3196 (1984).
91 Lexa, D., Momenteau, M. & Mispelter, J. Characterization of the reduction steps of Fe(III) porphyrins. *Biochimica et Biophysica Acta (BBA) - General Subjects* **338**, 151-163 (1974).
92 Close, D. M. & Wardman, P. Calculation of Standard Reduction Potentials of Amino Acid Radicals and the Effects of Water and Incorporation into Peptides. *J. Phys. Chem. A* **122**, 439-445 (2018).
93 Luo, P., Feinberg, E. C., Guirado, G., Farid, S. & Dinnocenzo, J. P. Accurate Oxidation Potentials of 40 Benzene and Biphenyl Derivatives with Heteroatom Substituents. *J. Org. Chem.* **79**, 9297-9304 (2014).
94 Tan, J. Z. Y. *et al.* Photoreduction of CO_2 using copper-decorated TiO_2 nanorod films with localized surface plasmon behavior. *Chem. Phys. Lett.* **531**, 149-154 (2012).
95 Zhang, X. *et al.* Photocatalytic Conversion of Diluted CO2 into Light Hydrocarbons Using Periodically Modulated Multiwalled Nanotube Arrays. *Angew. Chem. Int. Ed.* **51**, 12732-12735 (2012).
96 Hou, W. *et al.* Photocatalytic Conversion of CO_2 to Hydrocarbon Fuels via Plasmon-Enhanced Absorption and Metallic Interband Transitions. *ACS Catal.* **1**, 929-936 (2011).
97 Li, X., Zhuang, Z., Li, W. & Pan, H. Photocatalytic reduction of CO_2 over noble metal-loaded and nitrogen-doped mesoporous TiO_2. *Appl. Catal. A* **429-430**, 31-38 (2012).
98 Tahir, M. & Amin, N. S. Indium-doped TiO_2 nanoparticles for photocatalytic CO_2 reduction with H_2O vapors to CH4. *Appl. Catal. B* **162**, 98-109 (2015).
99 Xia, X.-H. *et al.* Preparation of multi-walled carbon nanotube supported TiO_2 and its photocatalytic activity in the reduction of CO_2 with H_2O. *Carbon* **45**, 717-721 (2007).
100 Liang, Y. T., Vijayan, B. K., Gray, K. A. & Hersam, M. C. Minimizing Graphene Defects Enhances Titania Nanocomposite-Based Photocatalytic Reduction of CO_2 for Improved Solar Fuel Production. *Nano Letters* **11**, 2865-2870 (2011).

101 Nguyen, T.-V., Wu, J. C. S. & Chiou, C.-H. Photoreduction of CO_2 over Ruthenium dye-sensitized TiO_2-based catalysts under concentrated natural sunlight. *Catal. Commun.* **9**, 2073-2076 (2008).
102 Zhao, Z.-H., Fan, J.-M. & Wang, Z.-Z. Photo-catalytic CO_2 reduction using sol–gel derived titania-supported zinc-phthalocyanine. *J Clean. Prod.* **15**, 1894-1897 (2007).
103 Tahir, M., Tahir, B., Amin, N. A. S. & Muhammad, A. Photocatalytic CO_2 methanation over NiO/In_2O_3 promoted TiO_2 nanocatalysts using H_2O and/or H_2 reductants. *Energy Convers. Manag.* **119**, 368-378 (2016).
104 Chen, X. *et al.* Ultrathin, Single-Crystal WO_3 Nanosheets by Two-Dimensional Oriented Attachment toward Enhanced Photocatalystic Reduction of CO_2 into Hydrocarbon Fuels under Visible Light. *ACS Appl. Mater. Interfaces* **4**, 3372-3377 (2012).
105 Liu, Q. *et al.* High-Yield Synthesis of Ultralong and Ultrathin Zn_2GeO_4 Nanoribbons toward Improved Photocatalytic Reduction of CO_2 into Renewable Hydrocarbon Fuel. *J. Am. Chem. Soc.* **132**, 14385-14387 (2010).
106 Shi, H., Chen, G., Zhang, C. & Zou, Z. Polymeric g-C_3N_4 Coupled with $NaNbO_3$ Nanowires toward Enhanced Photocatalytic Reduction of CO_2 into Renewable Fuel. *ACS Catal.* **4**, 3637-3643 (2014).
107 Xie, S., Wang, Y., Zhang, Q., Deng, W. & Wang, Y. $SrNb_2O_6$ nanoplates as efficient photocatalysts for the preferential reduction of CO_2 in the presence of H_2O. *Chem. Commun.* **51**, 3430-3433 (2015).
108 Zhang, H. *et al.* Efficient Visible-Light-Driven Carbon Dioxide Reduction by a Single-Atom Implanted Metal–Organic Framework. *Angew. Chem. Int. Ed.* **55**, 14310-14314 (2016).
109 Xu, Y.-F. *et al.* A $CsPbBr_3$ Perovskite Quantum Dot/Graphene Oxide Composite for Photocatalytic CO2 Reduction. *J. Am. Chem. Soc.* **139**, 5660-5663 (2017).
110 Xu, Y. *et al.* Chemical and Light-Driven Oxidation of Water Catalyzed by an Efficient Dinuclear Ruthenium Complex. *Angew. Chem. Int. Ed.* **49**, 8934-8937 (2010).
111 Volpe, A. *et al.* N-Heterocyclic Dicarbene Iridium(III) Catalysts Enabling Water Oxidation under Visible Light Irradiation. *Eur. J. Inorg. Chem.* **2014**, 568-568 (2014).
112 Hitoki, G. *et al.* Ta_3N_5 as a Novel Visible Light-Driven Photocatalyst (λ<600 nm). *Chem. Lett.* **31**, 736-737 (2002).
113 Ishikawa, A. *et al.* Oxysulfide $Sm_2Ti_2S_2O_5$ as a Stable Photocatalyst for Water Oxidation and Reduction under Visible Light Irradiation ($\lambda \leqslant$ 650 nm). *J Am. Chem. Soc.* **124**, 13547-13553 (2002).
114 Tao, X. *et al.* Bismuth Tantalum Oxyhalogen: A Promising Candidate Photocatalyst for Solar Water Splitting. *Adv. Energy Mater.* **8**, 1701392 (2018).
115 Fujito, H. *et al.* Layered Perovskite Oxychloride Bi4NbO8Cl: A Stable Visible Light Responsive Photocatalyst for Water Splitting. *J. Am. Chem. Soc.* **138**, 2082-2085 (2016).
116 Qi, Y. *et al.* Redox-Based Visible-Light-Driven Z-Scheme Overall Water Splitting with Apparent Quantum Efficiency Exceeding 10%. *Joule* **2**, 2393-2402 (2018).
117 Fang, Z.-B. *et al.* Boosting Interfacial Charge-Transfer Kinetics for Efficient Overall CO_2 Photoreduction via Rational Design of Coordination Spheres on Metal–Organic Frameworks. *J. Am. Chem. Soc.* **142**, 12515-12523 (2020).
118 Kim, W., Yuan, G., McClure, B. A. & Frei, H. Light Induced Carbon Dioxide Reduction by Water at Binuclear $ZrOCo^{II}$ Unit Coupled to Ir Oxide Nanocluster Catalyst. *J. Am. Chem. Soc.* **136**, 11034-11042 (2014).
119 Yuan, G., Agiral, A., Pellet, N., Kim, W. & Frei, H. Inorganic core–shell assemblies for closing the artificial photosynthetic cycle. *Faraday Discuss.* **176**, 233-249 (2014).